CRANFIELD UNIVERSITY

YE XIE

DESIGN AND ENERGY MANAGEMENT OF AIRCRAFT HYBRID ELECTRIC PROPULSION SYSTEM

SCHOOL OF AEROSPACE, TRANSPORT AND MANUFACTURING

Aerospace

PhD

Academic Year: 2015 - 2018

Supervisor: Al Savvaris, Antonios Tsourdos

September 2018

CRANFIELD UNIVERSITY

SCHOOL OF AEROSPACE, TRANSPORT AND MANUFACTURING

Aerospace

PhD

Academic Year 2015 - 2018

YE XIE

DESIGN AND ENERGY MANAGEMENT OF AIRCRAFT HYBRID ELECTRIC PROPULSION SYSTEM

Supervisor: Al Savvaris, Antonios Tsourdos

September 2018

This report is submitted in partial fulfilment of the requirements for the degree of PhD

ABSTRACT

This thesis investigates the design and development of a Hybrid Electric Propulsion System (HEPS) for aircraft. The main contributions of the study are the multi-objective system sizing and the two energy optimization algorithms.

First, the system sizing method is employed to design the hybrid electric propulsion system for a prototype aircraft. The sized hybrid propulsion system can ensure that no significant performance is sacrificed and the fuel economy is improved. The novel approach in this work is a new non-dominated sorting algorithm for the Non-dominated Sorting Genetic Algorithm (NSGA). The new algorithm can improve the time complexity of non-dominated sorting process. The optimized hybrid aircraft can save up to 17% fuel, achieve higher cruising speed and rate of climb. It is concluded that the optimal results are more sensitive to the variation of battery energy density than other parameters.

Next, the main components of the HEPS are modelled for example. The engine model provides an insight into the inherent relationship between the throttle command and the output torque. Regarding the d-q model of motor/generator, the estimation of torque loss at steady state is achieved using the efficiency map from experiments. The application of Shepherd model leads to the straightforward parameter identification.

In this research, both non-causal and causal energy management strategies for HEPS are investigated. The main novelty when studying convex optimization is the proposal of a new lossless convexification, which simplifies the formation of the convexified problem, and the proof of equality between the original problem and convexified problem. The introduced variable—battery internal energy, is proposed to convexify the

battery model. The first test case verifies that the convex relaxation does not sacrifice the optimality of the solution nor does the variable change lose the original bounds. Also, the optimal control from convex optimization is demonstrated to be robust to a disturbance in power demand. Comparison with the benchmark optimization—dynamic programming, shows that convex optimization achieves a minimal objective value with much less optimization time. Most significant is that the convexification reduces the optimization computation time to a level compatible with implementation in practical application.

In causal control, the main focus is to extend the original Equivalent Consumption Minimization Strategy (ECMS) with the fuzzy control. The proposed algorithm can maintain the battery State of Charge (SoC) in a desirable range, without the requirement of off-line estimation of equivalence factor. By comparing with non-causal control—dynamic programming, the test cases validates that the fuzzy based ECMS succeeds in converting the non-causal optimization, with little sacrifice of the optimality of the solution. In other words, the prior-knowledge of flight mission is not a pre-requisite, and the fuzzy based ECMS can achieve the sub-optimal control for on-line implementation. The fuzzy based ECMS is also validated to outperform the adaptive ECMS, since it can reduce the computation time of optimization and save more fuel usage. The theoretical relationship between the equivalence factor of ECMS and the co-state variable of Hamiltonian function is also demonstrated in this thesis.

The convex optimization and fuzzy based ECMS are combined to complete a flight mission with several sub-tasks. Each task has different power and SoC requirements. The test case demonstrates that only the combination of non-causal and causal optimization can satisfy the various constraints and requests of the test scenario. Compared with the engine-only powered aircraft, the hybrid powered aircraft saves 18.7% on fuel consumption. Furthermore, the hybrid propulsion system has better efficiency since it integrates the high efficient electric powertrain.

Keywords:

Light Aircraft, Hybrid Electric Propulsion System, Sizing, Modelling, Energy Management, Dynamic Programming, Convex Optimization, Pontryagin’s Maximum Principle, Fuzzy Logic Control, Hardware-in-the-Loop

PUBLICATIONS

A. Savvaris, **Y. Xie**, K. Malandrakis, M. Lopez, A. Tsourdos, Development of a fuel cell hybrid-powered unmanned aerial vehicle, in: 2016 24th Mediterr. Conf. Control Autom., IEEE, 2016: pp. 1242–1247. doi:10.1109/MED.2016.7536038.

Y. Xie, A. Savvaris, A. Tsourdos, J. Laycock, A. Farmer, Modelling and control of a hybrid electric propulsion system for unmanned aerial vehicles, in: 2018 IEEE Aerosp. Conf., IEEE, Bozeman, 2018: pp. 1–13. doi:10.1109/AERO.2018.8396436.

Y. Xie, A. Savvaris, A. Tsourdos, Sizing of hybrid electric propulsion system for retrofitting a mid-scale aircraft using non-dominated sorting genetic algorithm, Aerosp. Sci. Technol. 82–83 (2018) 323–333. doi:10.1016/j.ast.2018.09.022.

Under Peer-Review

Y. Xie, A. Savvaris, A. Tsourdos. Convexification in Energy Optimization of a Hybrid Electric Propulsion System for Aerial Vehicles.

Y. Xie, A. Savvaris, A. Tsourdos. Fuzzy Logic Based Equivalent Consumption Optimization of a Hybrid Electric Propulsion System for Unmanned Aerial Vehicles.

TABLE OF CONTENTS

LIST OF FIGURES

LIST OF TABLES

LIST OF ABBREVIATIONS

HEPS	Hybrid Electric Propulsion System
ICE	Internal Combustion Engine
EM	Electric Motor
CVT	Continuously Variable Transmission
RPA	Remotely-Piloted Aircraft
UAV	Unmanned Aerial Vehicle
MVM	Mean Value Model
ECU	Engine Control Unit
AC	Alternating Current
DC	Direct Current
SoC	State-of-Charge
SFC	Specific Fuel Consumption
DP	Dynamic Programming
FLC	Fuzzy Logic Control
ECMS	Equivalent Consumption Minimization Strategy
A-ECMS	Adaptive Equivalent Consumption Minimization Strategy
PMP	Pontryagin’s Maximum Principle
HiL	Hardware-in-the-Loop
NSGA	Non-dominated Sorting Genetic Algorithm

FNS	Fast Non-dominated Sorting
ENS	Efficient Non-dominated Sorting
HNDS	Hierarchical Non-Dominated Sort
MTOW	Maximum Take-Off Weight
RoC	Rate of Climb
DoH	Degree of Hybridization
BLDC	BrushLess Direct Current motor
PMSM/PMSG	Permanent Magnet Synchronous Motor/Generator
LiPo	Lithium-ion Polymer
MF	Membership Function
LTO	Landing and Take-Off cycle

LIST OF NOMENCLATURE

Aircraft

S	Wing area
AR	Aspect ratio
R_c	Rate of climb
d_{tkof}	Take-off distance
C_L	Lift coefficient
C_D	Drag coefficient
$C_{L,0}$	Minimum-drag lift coefficient
$C_{D,0}$	Zero-lift parasite drag coefficient
e	Oswald efficiency factor
C_{f_e}	Skin friction coefficient
S_{wet}	Aircraft wetted area
W_g	Global weight of aircraft
ρ	Air density
V	Aircraft speed
P	Power
F	Force
D	Drag
$stall$	Stall

$endur$	Endurance
$range$	Range
$cruise$	Cruise
$climb$	Climb
$tkof$	Take-off
LO	Lift-off
min	Minimum
max	Maximum
avg	Average

Multi-objective Genetic Algorithm

J	Objective function
O	Computational complexity
M	Number of objectives
N	Number of solutions
P	Population set
F	Pareto front set
p	Solution
Q	Solution set
R	Solution set
I	Solution set

Propulsion System

t	Time
m	Mass
$\dot{m}$	Mass rate
σ_p	Power-split
e_{air}	Altitude-related factor
e_{elec}	Motor efficiency and battery efficiency

e_{mech}	Mechanical efficiency
ε_f	Specific fuel consumption of the engine
ε_b	Energy density of the battery
P	Power
T	Torque
ω	Rotational speed
J	Inertia
G	Gear ratio
E	Energy
R	Resistance
L	Inductance
C	Capacitor
Q	Battery capacity
v	Alternative voltage
i	Alternative current
V	Direct voltage
I	Direct current
τ_{ice}	Time constant of the engine
δ_{ice}	Throttle command
$_{ICE}$	Internal combustion engine
$_{ice}$	Internal combustion engine
$_{EM}$	Electric motor
$_{mg}$	Motor/Generator
$_{mot}$	Motor
$_{gen}$	Generator
$_{prop}$	Propeller
$_{req}$	Requirement

ref	Reference
$fuel$	Fuel
$batt$	Battery

1 Introduction

Over the last decades, the rapid growth in fossil fuel consumption has generated a need for energy sustainability. Industries have made much effort to decrease the use of fossil fuels, but the fuel used in transportation is still increasing [1]. This is partly due to the widespread use of aircraft in both military and civilian applications. If the growth of air transportation continues, there will be the peremptory challenge in sustaining the petroleum consumption. Additionally, the exhaust gas from fuel combustion not only does harm to human health but also has a negative impact on the environment, for example, contributing to global warming. It is even worse if those emissions are from aircraft since the tail gas is directly discharged to the atmosphere. Concerning those adverse effects, NASA calls on the aeronautic industry to reduce aircraft fuel burn by 70% by 2025 in their N+3 concepts [2]. Meanwhile, FlightPath 2050 reported by ACARE targets a 75% reduction in CO_2 emissions [3].

The aim to sustain natural resources and relieve environmental pollution are pushing the related research areas to develop less fuel consumption and environmental friendly aerospace technologies. This leads to not only the development of renewable fuels but also alternative propulsion technologies.

1.1 Hybrid Propulsion System

The most prospective environmentally-clean propulsion technology is to shift towards electric propulsion systems, e.g. the Electric Motor (EM), replacing the conventional Internal Combustion Engine (ICE).

At the beginning of powered flight, the ICE was the most popular propulsion means for aerial vehicles. Even in today's transportation market, most air transport is based on fossil fuels, with no apparently sign of reduction of numbers. The emissions, noise and heating issues accompanied by ICE powering are difficult to tackle, if the ICE-powered aircraft want to achieve a good stealth performance. This must leads to the rapid development of electric powered aircraft.

For the propulsion point of view, an EM has better efficiency and responds much faster than an ICE does [4]. Electric propulsion systems do not generate on-board emissions, so are more environmentally friendly. From an aircraft point of view, electric powertrains have further advantage—elimination of all propulsion system noise excluding propeller noise. With reduced emissions and lower noise profile, the electric aircraft has better stealth performance compared with the ICE-powered one. However, the energy density (specific energy) of electrical energy storage source, such as batteries, are much lower than that of fossil fuel [5]. The truth is that at this point in time and for the foreseeable future, aerial vehicles using electric propulsion systems cannot achieve the same flight endurance as their conventional (i.e. combustion engine) powered counterparts.

Considering the disadvantages of ICE or EM powered flight, an evolving technology—Hybrid Electric Propulsion System (HEPS) comes to the researchers' mind and attracts much attention. HEPS integrates an electric powertrain with a conventional combustion engine to provide the propulsion. It can combine the clean power and system efficiency of an electric propulsion system with the extended range of an ICE. This results in decreased fuel burn and additional 'stealth mode' (low emissions/noise mode) compared with ICE-powered aircraft, and increased flying range compared with electric aircraft. HEPS has the potential to provide much better fuel economy. For these reasons, there is a significant interest in further research into this technology and applications for the aviation industry. However, those advantages come at the cost of increased complexity of the system design, modelling and hybrid energy management.

1.1.1 Powertrain Configuration

In a hybrid propulsion system, two or more power sources with different configurations are combined to improve the performance of the whole system. In this thesis, only two energy storages are considered: fuel and battery. For the fuel/battery hybridization

system, the most commonly used configurations are series, parallel and series-parallel architecture.

1.1.1.1 Series Configuration

In a series hybrid configuration, the propeller is driven only by the electric motor (see Figure 1-1). The engine power derived from combustion is converted into electrical power via a generator. The electrical power can be used to power the EM directly, or can be stored in the battery by a charging process. The benefit of this architecture is that the engine is completely decoupled from the propeller and its output power is not related to the power demand of the powertrain. In other words, the engine can run at its optimal operating condition during the different working condition. The fuel efficiency of engine can remain high and its lifespan can be lengthened. Moreover, the series architecture has the definite advantage of flexibility for locating the ICE-generator set due to the mechanical decoupling.

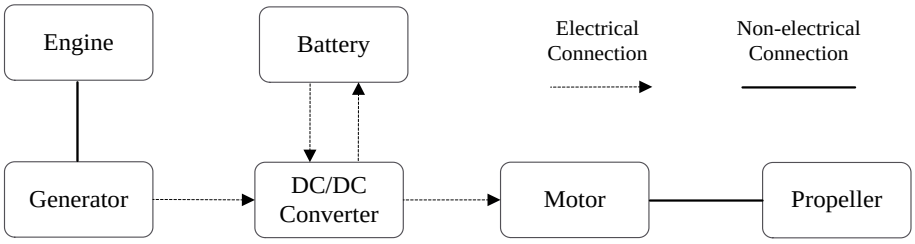

Figure 1-1 Series configuration

However, the series configuration suffers from the poor system efficiency, since massive power losses exist in the combustion and electrical energy conversion. Another disadvantage is that it needs three propulsion devices: engine, generator and EM. All three propulsion devices need to be sized to cope with maximum power if the series HEPS is designed for sustained climbs. This makes series HEPS expensive and bulky [5]. Last but not the least, series architecture cannot make use of the maximum combined power potential of the engine and motor, since the engine is not mechanically connected to the load.

1.1.1.2 Parallel Configuration

In parallel configuration, the ICE and the EM are both connected mechanically to the propeller, so they can contribute to the propulsion energy either simultaneously or individually. In addition with the parallel configuration, the ICE can simultaneously drive

the propeller and motor/generator, thereby charging the battery pack. Other advantage of the parallel over the series configuration is that it only needs two propulsion devices—engine and motor/generator. Also, a smaller engine and a smaller electric motor can be used to get the same performance [5]. Even for long-climb trip operation, only the engine needs to be rated for the highest sustained power. The power losses are also reduced compared with the series configuration, with no need of mechanical-electrical energy conversion.

However, the rotational speed of propeller is not always the optimal speed of the engine, thus operating at the optimum region of engine cannot be guaranteed. In general, there are two approaches to deal with this issue. The first and more direct one is to implement a Continuously Variable Transmission (CVT), which permits the independence of the engine and propeller rotational speed. The second and more economical one is to develop an energy management strategy. The energy management strategy can optimize the power contribution of the engine and the motor, which enables the propulsion devices to operate at their optimum condition.

Parallel hybrids are further classified according to the position of the motor/generator in the drivetrain [6]. If the engine and the motor/generator are mounted on two separate drive shafts, as shown in Figure 1-2, the speed of the engine and motor/generator can be different from the propeller and each other. This architecture is called as double-shaft parallel configuration. Similarly, if a CVT is applied in this architecture, the speed of two propulsion devices can be decoupled from the speed of the propeller.

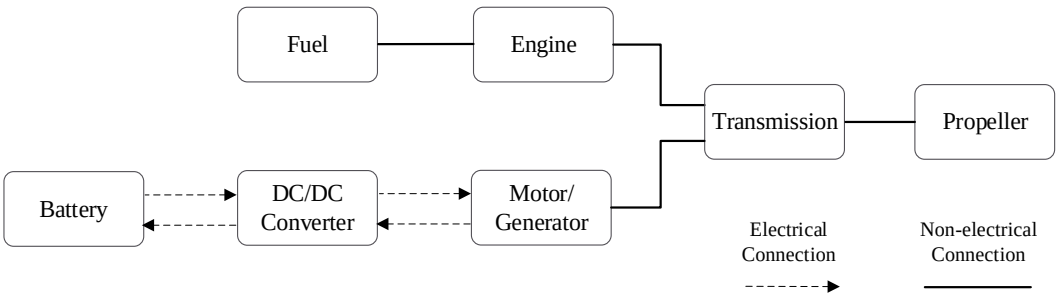

Figure 1-2 Double-shaft parallel configuration

If the engine is connected to the motor/generator but not directly linked to the propeller, the architecture is called single-shaft since the transmission has only one input shaft (see Figure 1-3). Generally, the electric machine is directly linked to the propeller, while the engine is connected to the electric machine via decoupling devices and gears. In

this architecture, the speed of motor/generator is always rigidly linked to that of the propeller.

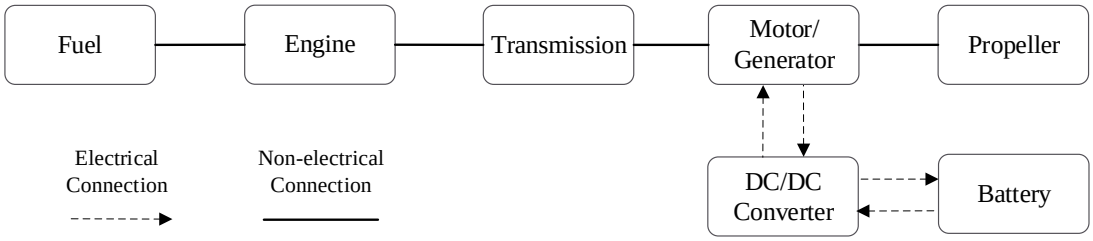

Figure 1-3 Single-shaft parallel configuration

1.1.1.3 Series-Parallel Configuration

The series-parallel configuration, also recognized as power-split configuration, is a mixture of the two architectures shown above. Here, the propeller, engine, motor and generator are connected to a planetary gear. This structure not only makes power distribution more flexible, but also allows the engine and motor to operate in its most efficient region. The series-parallel configuration is the most advanced configuration of the hybrid propulsion system, but it also requires the most complicated clutch/gearing mechanism and energy management.

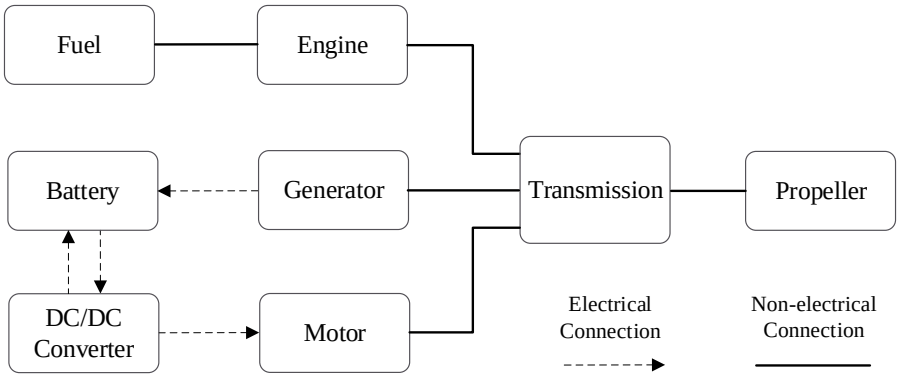

Figure 1-4 Series-Parallel configuration

Overall, the most commonly used configurations are illustrated above. Among them, the series configuration enables the engine to operate at its ideal operating condition. However, its system efficiency is relatively low since large power losses exist in the energy conversion. The series-parallel is the most functional, but complicated configuration out of the three architectures. The parallel configuration offeres a good trade-off between those two configurations.

1.1.2 Charge Strategy

In addition to the powertrain configurations, hybrid propulsion systems also differs in the battery operating strategy, having two classifications: charge-sustaining and charge-depleting strategy.

The charge-sustaining strategy aims at maintaining the State-of-Charge (SoC) of the battery at a certain level with on-board recharging. This ensures the battery will always have an adequate reserve SoC in the case of an emergency, but the electricity cannot be made the biggest use of. The charge-depleting strategy differs in that the battery charge does not take place. The battery SoC is allowed to decrease continuously until its minimum value is reached. A consequence of not charging the battery in a charge-depletion system is that the battery needs to have enough capacity to provide enough power during the specified run time. Therefore, the charge-depleting strategy tends to lead to a large battery.

1.1.3 State-of-Art

1.1.3.1 Ground Vehicle Application

Most people believe that hybrid cars powered by both gasoline and electric systems are relatively new, however they already existed at least as early as the late 1800s. In 1899, a car featured a gasoline-generator system fed four electric motors, is believed to be the first hybrid car. This hybrid car was constructed by Dr Ferdinand Porsche at Jacob Lohner & Co and named the Lohner-Porsche [7]. Shortly after Dr Porsche introduced the first hybrid, an American engineer H. Piper filed a patent for a petrol-electric hybrid vehicle in 1905. The hybrid vehicle employed an electric assist motor and a gasoline engine, capable of reaching a top speed of 25 mph (40 km/h) [8]. In 1916, a prominent electric vehicle company—Woods Motor Vehicle offered a hybrid electric car, Dual Power. It operated in electric-only mode under 15 mph (24 km/h) with the assistance of a four-cylinder ICE to achieve 35 mph (56 km/h) top speed. However, Dual Power was considered as a commercial failure, since it was too slow for its price and too difficult to service [9]. From the 1920s to the 1960s, the hybrid car drew little attention due to the low price of petrol and the advance of combustion engines.

1966 is the turning point of hybrid-electric technologies. U.S. Congress introduced the first bills recommending the use of electric vehicles as a means of reducing air pollution [10]. Additionally, with the Arab oil embargo of 1973, the soaring price of gasoline created new interest in electric and hybrid vehicles. In 1976, the U.S. Congress enacted Public Law 94-413, the Electric and Hybrid Vehicle Research, Development and Demonstration Act of 1976 [11]. The period of two decades from 1960 saw the accumulation of techniques related to hybrid vehicles. Regenerative braking systems, a core design concept of most modern hybrids, was developed in 1967 by American Motors Corporation [12]. An experimental hybrid car, XP-883, was constructed by General Motors in 1969 [13]. XP-883 demonstrated the concept—plug-in hybrid vehicle, whose battery can be charged by plugging it into an external source as well by its on-board engine-generator unit. In addition to hybrid cars, many concept hybrid buses were also released in those decades. Mercedes-Benz launched a project in 1969 to develop OE 302, which was the first hybrid omnibus [14]. Volkswagen researched into hybrid powertrains for their city taxis in response to the oil crisis in 1973. The prototype hybrid was based on a Volkswagen Type II microbus and reached a speed of up to 70 km/h [15].

Even with the accumulation of techniques, hybrid cars had been at experimental stage until the 1990s. In 1993, the “big three” American automakers (Chrysler, Ford and General Motors) and United States governmental agencies (Department of Energy etc.) combined forces in the initialization of Partnership for a New Generation of Vehicles (PNGV). All three manufacturers developed concept cars, but there were problems with the development of production prototypes [16]. The breakthrough came from the Japanese car corporation—Toyota. In 1997, Toyota launched the worldly first mass-produced hybrid vehicle—Toyota Prius, after two decades of its first hybrid prototype on the road [17]. In the same year, Audi introduced the Audi Duo, a hybrid car based on the A4 Avant, to the European market. Finally, in 1999, the introduction of the Honda Insight started the sales of hybrid automobiles to Americans. The “big three” American automakers hadn’t kept up to date until Ford released the first hybrid-electric sport-utility vehicle in 2005, one year after Toyota authorizing Ford to apply its patents to the hybrid manufacturing [18].

Global sales of hybrid cars are led by Toyota with more than 10 million Lexus and Toyota hybrids sold as of January 2017 [17]. The first-generation Prius sedan could offer a top speed of 100 mph (160 km/h) and a fuel economy of 42 miles per gallon

(mpg) for combined city and highway operation [5]. Both its fuel economy and exhaust emissions were much better than that of any conventional automobile. Toyota began the mass production of the Auris Hybrid in 2010. Auris Hybrid shares the same powertrain as the third-generation Prius, but the combined city/highway fuel economy increases from the original 50 mpg to 62 mpg [19]. The 2016 Prius Eco is acknowledged as the most fuel-efficient car available in the US without plug-in capability. After introducing the plug-in hybrid techniques, the all-electric range of Prius Plug-in Hybrid is several times longer than its conventional hybrid ones. Meanwhile, the equivalent fuel economy at electric-only mode is up to 133 mpg [20].

1.1.3.2 Aerial Vehicle Application

The widespread research and advances in hybrid electric propulsion systems in automobiles are transferrable to the aircraft industry. Automobile hybrid systems have been in use for several years, have been verified and widely accepted. Those benefits include increased endurance time as compared to electric-powered aircraft, with additional benefits of reduced noise, emissions and fuel consumption which are not attainable using gasoline-power. After acknowledging of those benefits, aeronautic academia and industry began to introduce the HEPS to power the aircraft. There is a significant interest in further research into this technology and its application on from small to larger-scale aircraft.

Initially, academics focused on the small-scale (unmanned) sector to validate and demonstrate the feasibility of the hybrid electric technology. The Air Force Institute of Technology (AFIT) began its investigations of hybrid electric technologies with the conceptual design and configuration comparison, see Harmon [21] and Hiserote [22]. It was concluded that the clutch-start parallel configuration is the most practically realizable. Continuing this work, Ausserer [23] and Molesworth [24] implemented the system validation and flight test, by integrating the 1.3-hp (969 W) Honda GX35 engine with a 1.6-hp (1.2 kW) Fuji motor. The research team from Queensland University of Technology (QUT) also developed a parallel HEPS by combing a 10 cc combustion engine and a 600 W brushless motor. Simulation and ground tests demonstrated that the aircraft performance [25] could be improved by a large margin and fuel usage [26] is decreased by 6%, with only a 5% weight penalty compared to the non-hybrid system. (Quasi-) static models of each component were developed for the preliminary design and sizing of HEPS, by Schoemann in the Technical University of Munich [9]. A scaling

method was applied since it is difficult to develop an accurate model for small engines. Friedrich and Robertson, from the University of Cambridge, researched design and sizing methods for hybrid-electric propulsion of a 20 kg UAV [27] where the combustion engine was sized based on the engine ideal operating line. Sliwinski, et al., investigated the range and endurance performance of HEPS powered aircraft [28] and demonstrated that hybrid electric technology represents a viable trade-off solution in small-scale aircraft.

The mid-scale aircraft (light manned aircraft) also has drawn much attention. At the early stage of HEPS study for small-scale aircraft, Hiserote questioned the adaptability of hybrid propulsion technologies to larger aircraft [22]. Using the same conceptual design method, Ripple (also from AFIT) successfully retrofitted several general aviation platforms using the mild HEPS [29]. In 2009, German aircraft builder Flight Design presented a hybrid electric system where a 40-hp (30 kW) EM can provide approximately 5 min of additional power to a 115-hp (86 kW) ICE [30]. Based on this hybrid system, a light aircraft–EcoEagle was developed by Embry-Riddle Eagle Flight Research Center to compete in the NASA's Green Flight Challenge 2011 [31]. However, though using a parallel configuration, EcoEagle has the same issue as the Hybrid Atlas (built by the University of Cambridge in 2010 [32]). Neither of these has the capability to recharge the battery during flight. Following a new project–SOUL, The University of Cambridge successfully retrofitted a light sport aircraft and completed on-board regeneration, by combing an 8 kW ICE and a 12 kW EM [27]. The first series-configured hybrid-electric manned aircraft, named DA36 E-Star, was demonstrated by Airbus, Siemens and Diamond Aircraft [33]. It launched its debut flight on June 2011, featured a 70 kW motor made by Siemens and 30 kW rotary engine made by Austro Engine. A more advanced version, DA36 E-Star 2, benefited from the revised electric powertrain and was approximately 100 kg lighter than its predecessor [34]. Also, an increase in range/duration was expected. HYPSTAIR project, starting from 2013, unveiled the prototype of the world's most powerful series hybrid powertrain (200 kW) for general aviation, after a four-year study [35]. The University of Nottingham initialized the conceptual design of hybrid electric propulsion for skydiver aircraft [36]. The study demonstrated that the series-hybrid-distributed architecture could offset the problematic aspects of increased HEPS weight.

The world's largest aerospace magnates have been exploring the potential of hybrid-electric technology on large-scale transport aircraft, i.e. regional or even

intercontinental airlines. The Georgia Institute of Technology won the 2012-2013 Federal Aviation Administration (FAA) Design Competition in electric/hybrid-electric aircraft technology category [37]. The developed technology suite implemented on the NXG-50 hybrid aircraft provided a future regional jet with expected reductions of 15% for life-cycle energy consumption. Airbus invited Siemens as the third partner to support the E-Fan X program in 2017, as a first step in the long-term goal of developing a hybrid-electric regional airliner [38]. The Delft University of Technology explored innovative propulsion techniques to achieve NASA N+3 goals. One feasible design for hybrid regional aircraft results in a fuel weight drop of 28 %, and a global aircraft weight rise of 14 % [39].

The hybrid electric distributed propulsion for transport airplanes is highly rewarded in recent years [40]. NASA leads the concept of Turbo-electric Distributed Propulsion (TeDP) that hybridizes turboshaft engine and distributed electric powertrain in a series architecture. Following the successful project SCEPTOR [41], ESAero continued to work with NASA on SBIR program to investigate the benefit of a gas generator and superconducting motor [42]. NASA also funded Boeing SUGAR team to boost the promotion of subsonic air transport using hybrid electric concept design. The 2014 final report demonstrated that hybrid SUGAR Volt is able to meet NASA goals in terms of fuel burn [43]. With the experience of developing hybrid DA36 E-Star, Airbus started a joint project DEAP [44] with Rolls-Royce in 2016. The proposed E-Thrust concept can also be described as a series-hybrid/distributed propulsion system.

1.2 Aims and Objectives

The research aim of this study is to improve the fuel economy of aircraft hybrid electric propulsion system. This aim can be accomplished by studying the design and energy management of HEPS for aircraft applications. The thesis first designs a hybrid electric propulsion system for a prototype aircraft and investigates how to achieve better fuel economy of the hybrid aircraft at the design stage. Fuel consumption of the HEPS is further reduced by researching different energy management strategies, i.e. supervisory controls.

The objectives of the four main work are illustrated as follows:

(1) Design: The designed hybrid electric propulsion system needs to achieve improved fuel economy with little-compromise in aircraft performance. Therefore, the system sizing method must achieve optimal trade-off between the fuel consumption and flight duration.

(2) Modelling: This part of work aims to develop a simulation environment to validate the energy management methods. Different dynamic models are studied according to different subsystems' timescales characteristics.

(3) Non-causal Energy Management: The objective of this part is to study a non-causal optimization that not only simplifies the original energy management problem, but also does not lead to any loss of original optimality. The time cost of the optimization process is required to be lower than the dynamic programming.

(4) Causal Energy Management: The causal control based method is researched here to realize the on-line optimization of the original non-causal problem. The proposed causal control based algorithm must have little sacrifice of the original optimality.

1.3 Contributions

This thesis presents a successful design for an aircraft hybrid electric propulsion system and management of its energy distribution. The design method results in the hybrid aircraft that can save 17% fuel consumption compared with the prototype aircraft. The studied energy management strategies further improve the fuel economy of the hybrid aircraft. Up to 18% fuel is reduced by comparing the hybrid aircraft and the engine-only powered aircraft.

The main contributions of the study are the multi-objective sizing method and the two energy optimizations:

- For the system sizing, the optimal trade-off between fuel consumption and flight duration is achieved by applying the multi-objective genetic algorithm. The author does not find any open full-length-articles covering the detailed analysis of hybrid propulsion system sizing using multi-objective genetic algorithm. This part of work proposes a new non-dominated sorting algorithm for the Non-dominated Sorting Genetic Algorithm (NSGA), which can reduce the number of

comparisons and improve the time complexity of non-dominated sorting process.

- The convex optimization is applied due to its low computational complexity. Currently, there still no research is conducted to apply the convex programming to the HEPS of aircraft. A new lossless convexification proposed in this thesis, can simplify the formation of the convexified problem, and the proof of equality between the original problem and convexified problem. Most significant is that the convexification reduces the optimization computation time for implementation in practical application.
- The fuzzy logic control is employed to solve the equivalence factor issue of Equivalent Consumption Minimization Strategy (ECMS). The fuzzy-based ECMS succeeds in transferring the original causal problem into the instantaneous one, with no need for off-line estimation of equivalence factor. Furthermore, it realizes the on-line charge-sustaining, with no sacrifice of the computation time. It can resolve the conflict between the SoC sustaining and electric power consumption. Neither sustaining the SoC at the high or low level, the proposed approach exploits the advantages of HEPS for the aircraft to the full.

1.4 Thesis Layout

This thesis completes the design, modelling, energy management of an aircraft hybrid electric propulsion system.

Chapter 1 introduces the background of the development of aircraft HEPS. The state-of-art of hybrid configurations and studies of hybrid propulsion technologies are also presented.

Chapter 2 reviews the previous work related to the system sizing, modelling and energy management of hybrid propulsion system. The research gaps in these areas are demonstrated based on the analysis of the pros and cons of various methods and algorithms.

Chapter 3 accomplishes the design of a HEPS for the prototype aircraft, using the multi-objective genetic algorithm. A new non-dominated sorting algorithm is proposed

to reduce the computational cost. The optimized HEPS can reduce fuel consumption by up to 17%.

Chapter 4 presents the modelling of the engine, motor/generator, battery and DC/DC converter of the HEPS.

Chapter 5 studies the convex optimization to solve the original non-causal energy management of the HEPS. A lossless convexification is proposed to convexify the original problem. The optimality of the original problem is not sacrificed but the computational efficiency is improved.

Chapter 6 converts the original non-causal energy management to a causal optimization problem, using the proposed fuzzy-based equivalent consumption optimization. The new method achieves the on-line optimization with sub-optimal solutions.

Chapter 7 demonstrates that the HEPS-powered aircraft can save around 18% fuel using the two energy optimizations. The fuzzy-based equivalent consumption optimization is proved to resolve the conflict between the SoC sustaining and electrical power consumption.

Chapter 8 summarizes all the work and its conclusions. The future work is then recommended.

2 Literature Review

This chapter reviews the previous work related to the system sizing, modelling and energy management of hybrid electric technologies. The advantages and disadvantages of various methods and algorithms are demonstrated based on the previous studies and their conclusions. New approaches or applications are proposed according to the research gaps in the system sizing and energy management.

2.1 Sizing

The first technological problem to be resolved when introducing hybrid electric technology, is the synergetic design and sizing of the propulsive system at aircraft level. The sizing mentioned in this study means the process of determination of parameters of the corresponding devices, which can represent their weight, output power and energy capacity characterises.

The pioneer of hybrid technology—AFIT firstly applied the conventional aircraft design method to size the aircraft wing and HEPS components for the Unmanned Aerial Vehicle (UAV) [21,45]. The sizing problem was formulated as a constrained optimization problem, in which UAV performance requirements were represented by the constraints. Based on the optimization code developed by Harmon and Hiserote [21,45], Ripple applied the sizing approach to design the HEPS for the mid-scale Remotely-Piloted Aircraft (RPA) [29]. Case studies demonstrated that the retrofit of the existing airframe is possible, but the fuel saving ability is not clear in the study. For a regional airline case, Delft University of Technology integrated the weight estimation function to the optimization iteration [39]. It was concluded that 30% fuel reduction could be accessible if the battery technique could be promoted to 1000 Wh/kg.

Isikveren proposed so-called quadrant-based algorithmic nomograph to pre-design the aircraft with advanced propulsion systems [46]. This universal graphical-based approach allows for maximizing transparency for the designer, since the optimization is not used in the design process.

Generally, a propulsion system sizing should not be regarded singularly since it describes the interdependency of the propulsion system and aircraft [21]. However, integrated propulsion system and aircraft sizing are time-consuming. Therefore, Schömann introduced the aircraft scaling approach and only focused on the propulsion system sizing [47]. The optimization results achieve 5% fuel mass reduction in the hybrid powered aircraft. Using the scaling method but no need of optimization, Friedrich, et al., showed the feasibility of HEPS application on small unmanned aircraft and intercity airliners, with 47% and 10% fuel saving, respectively [27]. Glassock, et al., provided a detailed comparison of the fuel burn, battery weight and climbing performance between the original skydiver aircraft and its hybrid-retrofitted one, covering the full spectrum of hybridisation ratio [36]. The hybrid-energy retrofitting of reference aircraft was successfully achieved by Pornet et al., even considering the medium-range mission [48]. The study claimed that the retrofitted aircraft has a potential to save 16% fuel burn for a 900 n mile (1666 km) mission. Furthermore, sizing the hybrid aircraft to its reference range (3300 n mile) would lead to an increase of the wing area. The range and endurance are mainly concerned characteristics when retrofitting the RPA with HEPS in the study by Sliwinski et al. [28]. The results suggested that HEPS technology could promote the mitigation of exhaust while providing adequate range and endurance performance, compared with the ICE-only propulsion system. In short, researchers are benefited from sizing the HEPS excluding the aircraft design. A prototype (reference) aircraft is selected in those studies. The verification of hybrid aircraft is straightforward by just being compared with the prototype one.

Most studies on the sizing of HEPS employ single-objective optimization to reach the optimal results [47]. However, the single-objective (such as fuel minimization) can only give one optimal sizing at one specific performance request (like duration), in one optimization run. Therefore, several optimization runs have to be carried out to examine the different performance demands [28,36]. The multi-objective optimization can simultaneously optimize several costs and result in Pareto-optimal solutions. Pareto-optimal solutions, or so-called Pareto front, is the combination of all possible

optimal outcomes. If the performance needs are also included in the cost function, the potential of the hybrid propulsion system can be thoroughly evaluated in one optimization run, by using multi-objective optimization.

An engineering note about hybrid unmanned aircraft design using multi-objective genetic algorithm has been published in 2016 [49]. Yet the authors did not find any open full-length-articles covering the detailed analysis of hybrid propulsion system sizing using multi-objective optimization. The design of HEPS for aircraft starts with the system sizing using the multi-objective genetic algorithm.

2.1.1 Multi-objective Genetic Algorithm

Since the Genetic Algorithm (GA) works with a population of points, it may capture a number of Pareto-optimal solutions in one single simulation run. The study of multi-objective GA is as early as the 1980s. Schaffer and Grefenstette applied GA to multi-objective learning, but their algorithm suffered from biasness towards some Pareto-optimal solutions [50]. To eliminate the bias, Srinivas and Deb proposed the famous Non-dominated Sorting Genetic Algorithm (NSGA) in 1994 [51]. The proposed algorithm avoids the bias and distributes of the population over the entire Pareto-optimal regions. The proof-of-principle simulation also demonstrated that NSGA could maintain stable and uniform reproductive potential across non-dominated individuals.

However, NSGA was criticised due to its high computational complexity, lack of elitism and need for specifying the sharing parameter [52]. Therefore, Deb, et al., brought the second version of NSGA—NSGA-II, which alleviates all the above three issues. Simulation results show that the proposed NSGA-II, in most problems, is able to find a much better spread of solutions and better convergence near the true Pareto-optimal front. Nevertheless, the computational complexity is still relatively high although the Fast Non-dominated Sorting (FNS) was proposed. This is also a common problem most existing of the Pareto-front-based evolutionary algorithms.

2.1.2 Non-dominated Sorting Algorithm

Non-dominated sorting is a procedure where solutions in the population are assigned to different Pareto fronts based on their dominance relationships. It accounts for a large

part of the computation of NSGA. If the computational complexity of non-dominated sorting can be reduced considerably, the computing efficiency of NSGA will be benefited a lot.

The idea of non-dominated sorting was first suggested by Goldberg as a selection strategy for the multi-objective evolutionary optimization [53]. Srinivas and Deb then introduced it to its NSGA. The time complexity of the original non-dominated sorting is $O(MN^3)$ and a space complexity of is $O(N)$, where M is the number of objectives and N is the population size. Deb, et al., successfully decreased the time complexity to $O(MN^2)$ in the NSGA-II [52], though the space complexity increased to $O(N^2)$. The new non-dominated sorting algorithm is termed Fast Non-dominated Sorting (FNS). FNS is the first to acquire all the dominance relation between every two solutions by traveling all the solutions. Since proposed by the research group leaded by Deb, FNS becomes the benchmark of the non-dominated sorting algorithm. Schorlars have been engaged in reducing the complexity of non-dominated sorting.

Jensen extended the divide and conquer vector sorting algorithm and applied it to the non-dominated sorting [54]. The recursive non-dominated sorting approach leads to the time complexity of $O(N \log^{M-1} N)$. This means that Jensen's sorting method can only reduce the computation time by a large margin for bio-objective problems. Its complexity increases expotentially with the number of the objectives. Furthermore, this approach is only applicable to problems with weak dominance, which is less more commonly used than the strong dominance (where a solution only dominates another if it is better for all objectives).

Arena's principle was proposed by Tang et al. [55] in 2008. The concept of arena host was established to construct the non-dominated set. A randomly selected solution is set as the first arena host. Then, the arena host is compared with each of the remaining solutions. Consequently, all the solutions can be divided into two parts: dominated or non-dominated set. Different from Arena's principle, the deductive sort [56] proposed that each solution is compared against all following solutions and not previous solutions. If any solution is found to be dominated, it can be ignored in later comparisons. Both Arena's principle and deductive sort didn't reduce the worst case complexity of FNS, but they do perform better in the simulation tests.

Efficient Non-dominated Sort (ENS), proposed by Zhang et al. in 2015 [57], is the most promising sorting approach since the FNS. Both theoretical analysis and empirical

results show that the ENS is computationally more efficient than all previous non-dominated sorting methods. ENS creatively proposed to first sorts all candidate solutions in ascending order by their first objective. This approach guarantees that the succeeding solution can never dominate the preceding solution. Therefore, a considerable number of unnecessary comparisons can be omitted. Regarding the necessary comparisons, both the sequential search and binary search were studies and compared. Zhang et al. extended ENS to the Approximate-ENS (A-ENS) [58]. It significantly enhances the time efficiency for many-objective optimizations, which has more than three objectives. The time complexity of A-ENS is independent of the number of objectives and fixed to $O(N^2)$.

2.2 Modelling

In systems engineering, a general approach for modelling is to focus on the dynamics of interest. The dynamics that are not quite related to the targeted application are ignored. In terms of different levels of details, the model can be classified as steady-state (static) and transient (dynamic) one.

(Quasi-) Static Model: Static and quasi-static models are treated under the same category since both types of models serve similar purposes. They have several advantages in comparison with more detailed models. Without complex differential equations, (quasi-) static models are less time-consuming and better qualified for real-time simulation. With limited approximation ability, their main objectives are to evaluate steady-state performance and slow response performance, such as fuel economy and exhaust emissions. From the preliminary studies of propulsion systems, the (quasi-) static model are widely employed on the system sizing [22,27,48] and energy management design [59,60].

Low-frequency Dynamic Model: Since the static and quasi-static models are mostly qualified for average performance ratings, a dynamic model is required to present the transient activity. In addition to the benefits of (quasi-) static models, low-frequency dynamic models provide detailed descriptions of dynamics that have impacts on stability and control performance, with a negligible compromise on the accuracy of models. In general, the validation of energy management strategies requests the numerical simulation with dynamic models [61,62].

In this thesis, the (quasi-) static models are adopted in the research on the design of the hybrid propulsion system and its energy management. The detailed dynamic models are studied to develop the simulation system. The literature review of dynamic modelling of different components is illustrated as follows.

2.2.1 Engine

The Mean Value Model (MVM) is widely applied when the purpose of modelling is to identify engine output performance (power and torque), rather than implementing detailed engine design. The MVM neglects the discrete cycles of the engine and assumes that all processes and effects are spread out over the engine cycle [63]. It not only simplifies phenomena that are too fast or sophisticated such as thermodynamic and kinetic processes, but also keeps the rotational dynamics and is able to predict fuel injection and pollutant formation. Hence, the MVM is suitable for the speed control design and fuel/exhaust analysis of engines [64]. However, the traditional MVMs still consider the inlet manifold dynamics and flow rate dynamics, etc. Those details are unnecessary for the simulation of hybrid propulsion systems, as well as increasing the complexity of modelling. As a result, the application of the simplified MVM is widespread.

The simplified MVMs usually focus on torque output and fuel consumption rate. In some studies [65,66], the engine model is simplified to a first-order or second-order transfer function characterizing the torque response. The dynamics of torque response is reflected by the time constant and damping ratio. The engine losses are approximated on the steady-state condition. This approach can assure the steady-state performance to be well modelled, at the same time preserving a certain level of dynamics. However, it cannot reveal the relationship between the engine throttle position and output capability, which is the main characteristic interesting researchers. This study aims to develop a simplified MVM of the engine that provides an insight into the inherent relationship between the throttle command and the torque output.

2.2.2 Electric Subsystem

Motor/Generator: The well-established d-q model was introduced to model Permanent Magnet Synchronous Motor/Generator (PMSM/PMSG) during the 1990s [67,68]. In a salient pole Alternative Current (AC) machine, parameters (such as phase inductance) change with the rotor turning in the machine. This introduces a set of time-varying variables to the equations for each phase, which increases the complexity of model [67]. The transformation of equations to the d-q frame forces all varying inductances to become constant, thereby simplifying the dynamic model. In terms of steady-state behaviour of the d-q model, the energy losses are approximated to achieve a good match with experimental data. There was a novelty in the use of efficiency data and a general purpose friction moment in [69].

DC/DC Converter: The general-purpose power stage model can be used under different operating modes. Since switching power supplies are discontinuous and non-linear by nature, the linearization techniques need to be applied. The state-space averaging model [70] is one of the linearization methods that result in a continuous mode of the power stage. This modelling approach has been widely employed in the power management of systems including the supercapacitor and battery [71,72]. Recently, its implementation on the voltage buck/boost between the PMSM and lithium battery draws much attention [73].

Battery: The main purpose of battery modelling in hybrid propulsion system is to present its charge/discharge characteristics and predict the SoC that is indispensable for the energy management. Therefore, the electric circuit-based model should be precise enough for the application. The most widely applied electric circuit-based model is the one proposed by Shepherd in 1965 [74]. This model pays attention to charge/discharge characteristics with open circuit voltage and internal resistance. It neglects Resistance-Capacity (RC) circuit dynamics since the two RC-circuit modes are much faster than the dynamics of SoC. This model can also present the discharge and charge process. However, it leads to an algebraic loop problem in the mathematical simulation. To resolve this issue, Tremblay, et al., replaced the polarisation resistance with the polarisation voltage [75,76].

2.3 Energy Management

Different from the one in a conventional non-hybrid vehicle, the controller in an HEPS is generally recognized as two levels: supervisory control and component control [4]. The supervisory controller functions at the energy management level, splitting power or torque request between the combustion and electric powertrain. The lower level component controller, which receives commands from the supervisory controller, aims to regulate the performance of each subsystem (component). The component controller sometimes is applied to optimize the system efficiency in series hybrid systems [77,78]

With the demand for the energy management, supervisory control strategies attract more attention and have been widely studied. Broadly, the energy management strategies of hybrid propulsion system can be classified into causal and non-causal ones.

2.3.1 Non-Causal Control

The purpose of energy managing is to distribute the engine and motor power to meet one or several criteria. If the objective is to optimize one performance along the complete mission profile, the optimization problem with a time-varying cost function is normally formulated. Since the state of this kind of problem is dependent on future inputs, the energy management strategy used to solve it is called the non-causal control. Many researchers also name this kind of problem as ‘global optimization problem’, for which the complete mission is taken as the ‘global information’. However, the non-causal or time-global problem is used in this thesis to avoid ambiguity.

When the fuel minimization is the objective, the non-causal control can get time-global optimum by minimizing the cost function representing fuel economy along a given mission profile. Unless future mission information is priori-known, the non-causal control cannot be implemented on the practical application. Despite this, the non-causal optimization is still the most studied energy management strategy for the hybrid propulsion system [79].

In general, there are two approaches handling the formulated energy optimization of hybrid propulsion systems: the one is to solve the original nonlinear problem directly;

another one is to simplify the original problem with approximation techniques. Several optimizations have been applied to solve the original energy management problem, such as dynamic programming [80,81] and genetic algorithm [82]. The dynamic programming is the dominant one for solving the complicated nonlinear system.

Dynamic Programming: The Dynamic Programming (DP) is one of the most studied non-causal optimizations since it can guarantee the global optimality of the solution [83]. The conventional DP requests the prior-known of the complete mission, so it is also called as Deterministic DP (DDP). The DDP was first introduced to the optimal control of hybrid vehicles in the 1980s [84]. After about one decade, Brahma et al. applied the same method to the optimization of the power split between electrical generation and energy storage in series hybrid vehicles [85]. On the other hand, many researchers benefit from extracting sub-optimal power split from the DDP, rather than directly implementing the DDP results [86–88]. In the study by Lin et al. [86], the DDP was firstly used to optimize the gear-shifting ratio and the power split of a parallel HEPS, subjecting to the battery SOC-sustaining constraint. Then, the near-optimal rules were extracted and implemented in the real practice. Ref. [88] employed the same approach in a series-parallel hybrid configuration. The simulation results of the extracted rules were proved to be very close to the optimal ones. However, the extraction process is generally time-consuming, and extracted rules are only sub-optimal for the given mission [89].

To overcome the drawback of poor adaptability, Lin et al. proposed the Stochastic DP (SDP) [89], one year after they studied the DDP. Instead of being optimized over a given driving cycle, the power split is optimized over a family of random driving cycles. The power demand of driving cycles is represented by the stochastic Markov process. It was found that the proposed SDP control algorithm outperforms sub-optimal rules extracted from the DDP results. The stress of electrical powertrain was considered in the study of SDP for a retrofitted hybrid vehicle [90]. The designed SDP yielded a 13% reduction in electrical powertrain stress without sacrificing any fuel savings. However, this approach did require a collection of representative driving data on which to be based. Those data may not be readily available [90].

On the other hand, many researchers aim to reduce the computational burden of DP, by combing the DP with other methods [91,92]. However, those DP-based algorithms sacrifice the optimality of DP, thereby leading to poorer accuracy [79]. Moreover, those

improved algorithms still suffer from large computational cost, since they all consider the complete nonconvex characteristics of the energy optimization problem.

The most effective way to reduce the computational complexity is to simplify the original energy optimization problem. So forth, several simplification approaches have been implemented, and their corresponding optimization algorithms have been studied. Those programming algorithms include linear programming [93,94], quadratic programming [95–97], mixed integer linear programming [98–100], and convex programming problem [101–103]. Those approaches can effectively simplify the original problem and save the time cost of study. The convex programming is worth further studying and more attention, since it can avoid over-simplification compared with the linear programming and quadratic programming [104].

Convex Optimization: The convex optimization was firstly proposed by Murgovski et al. [105,106] to solve the component sizing and energy management of a plug-in hybrid city bus. Due to low computational complexity, the convex modelling approach enables the optimization of problems with several state variables. Therefore, the convex programming can simultaneously optimize the battery size and energy distribution, on the condition that the city bus is driven along a perfectly known bus line. The original non-convex, mixed integer problem was converted to a new problem by two main steps.

The first one is the convexification process. The battery pack energy was first introduced as the state variable. The state transition equality became convex but not affine, by replacing the battery SoC with battery pack energy. Then, the non-affine equality constraint was relaxed to a convex inequality constraint. Finally, the battery constraints were converted to a convex form. The second step is to relax the mixed integer convex problem into conventional convex programming. Two integer control variables—gear ratio and engine on/off were tuned outside the optimization loop. The heuristic decisions of these two variables were based on the demanded power and speed of vehicles. This heuristic approach removes the need for solving a mixed integer problem, thereby reducing the complexity of the problem. The results indicated that both the convexification process and heuristic approach have a small influence on the optimal solution. The convex optimization pointed toward similar battery size to one of the DP [106].

In the following further study of Elbert et al. [107], the convexification process was similar to the previous study. However, the optimal engine on/off strategy was calculated analytically using Pontryagin's maximum principle. The engine is switched on if and only if the requested power exceeds a certain threshold, which is dependent on the co-state and electrical buffer energy. The study also gave the necessary condition for a globally optimal solution of the convexified problem. It was shown to deliver optimal results in less time than DP even in the presence of active state constraints.

The lifetime of the battery was considered in another study by Murgovski et al. [108]. A simple battery wear model was adopted to predict the life of the battery. The battery replacement times within the vehicle lifetime is taken as the optimized variable. The integer number of replacement times was relaxed to a real number to convexify the original problem. The ceiling of this real number was labelled as the maximum number of replacements, which was used in the cost function and constraints. One significant finding of this paper is that the optimal result of battery size is noticeably different, when the battery lifetime is considered in the sizing problem [108].

The convex programming has been proved to be an efficient optimization to solve the component sizing and energy management problem. However, the approximation and relaxation methods used in the convexification process, may lead to the errors between the original problem and the convexified problem. In [109], Murgovski et al. illustrated that the relaxation of state transition equality does not bring any errors between the original and the convexified model. In other words, the solution of the relaxed problem will provide the solution to the non-relaxed problem. The proposition given in the paper indicated that the global minimum of the original problem could be obtained by solving the relaxed problem without the loss of equality. The effect of approximation was not discussed in the paper.

Hu et al. [110] extended the convex programming to the application of fuel cell and battery hybrid vehicles. The battery State-of-Health (SoH) model was adopted in the study to consider the longevity of the battery. Since the SoH state equation is naturally convex, only one equality relaxation is needed to convexify the SoH constraint. In later research [111], the objective of optimization was changed to the minimization of carbon dioxide emissions. The study adopted an economic grid dispatch model for power plants to generate marginal grid carbon dioxide emissions. The results revealed that

the size of battery size does not necessarily grow as the emission of carbon dioxide levels reduces.

Currently, there still no research is conducted to apply the convex programming to the HEPS of aircraft. This thesis proposes a new convexification method. It can not only retain the feature of lossless relaxation from previous studies, but also lead to a more straightforward and explicit form of convexified problem.

2.3.2 Causal Control

Though the simplification can reduce the complexity of the original problem, the application of non-causal energy management still cannot be implemented in the real-time application, if the complete mission profile is not priori-known. Therefore the causal control is introduced to the energy management of hybrid propulsion system.

In addition to the optimization algorithm, the causal energy management can also refer to the rule-based control since the control rules generally consider the current or past system information. The rule-based causal energy management and optimization-based one are illustrated in the following text.

2.3.2.1 Rule-based One

The rule-based control is comprised of a series of logic statements, which can determine the modes of operation only dependent on past and current system states. Therefore it is easily implemented as the real-time supervisory control. Without the optimization algorithm, the rule-based control achieves the best criterion by regulating the system to one ‘optimal’ condition. This ‘optimal’ condition is determined by the designer using different kinds of performance maps. The fuel rate map, motor efficiency map and battery efficiency map are selected according to the predefined optimal criterion. The rule-based control can be further subcategorized into deterministic rule-based and fuzzy rule-based one.

The deterministic rule-based control employs the classic set theory and elements to define different modes of operation. The transitions between those modes are determined by the logic rules. The rules are normally designed based on the operation states of the engine, such as the most efficient point [112], engine optimal operation line [113] and engine peak efficiency region [114]. Regardless of the point/line/region,

the basic idea of those rule-based controls is to operate the engine around its optimal condition while adopting the EM to provide additional power. In some further studies [115], not only the engine/fuel efficiency is considered, but also the transmission power loss and electric system efficiency are taken into account. No matter how complicated the optimal criterion is, it can be represented by the deterministic states and rules. Therefore the rules-based strategy is simple and easy to apply. However, the deterministic rules-based control is not robust to the model uncertainties and measurement disturbances.

Fuzzy Logic Control: In essence, the Fuzzy Logic Control (FLC) is the linguistic rule-based control, so it is an extension of the deterministic rule-based control. Unlike the classical set theory, the membership of an element in a fuzzy theory is uncertain and is typically numbered between zero and one. That decides that the FLC deals with reasoning using an approximate way rather than the precise way. As a result, the FLC is tolerant to imprecise measurements and variations, thereby being robust against system uncertainties [116].

As early as the 1990s, Lee and Sul [117] applied the fuzzy logic decision-making to generate motor torque command of the hybrid powertrain of a city bus. The torque command was dependent on the acceleration pedal stroke and the rotational speed of the motor. The fuzzy rules were extracted from road tests, which characterized the relationship between the motor torque and the nitrogen oxides emission. The designed FLC achieved the 20% reduction of nitrogen oxides emission in the dynamometer test. Schouten, et al., [61] developed a set of fuzzy rules to determine the energy split between the combustion and electric powertrain. The underlying theme of the rules is to optimize the operating efficiency of the complete hybrid propulsion system. The fuel economy was also improved in the simulation tests. Schouten, et al., [61] selected the Takagi-Sugeno (T-S) fuzzy system, instead of the Mandami type. Baumann, et al., [118] gave the definition of Degree of Hybridization (DoH) when conducting the mechatronic design of hybrid powertrains. The ICE-dominated configuration (DoH<0.48) was preferred due to the smaller battery pack and less cost. It was demonstrated that better fuel economy and drivetrain efficiency could be achieved with the fuzzy logic controller for the ICE-dominated hybrid automobile.

In some further studies, the FLC is tuned by other intelligent algorithms [119–121]. The parameters of membership functions of FLC were optimized by the genetic algorithm [119]. Further reduction of fuel and emissions were realized with the tuned parameters.

However, those improved advance algorithms sacrifice the low-complexity and easy-implementation of fuzzy rules control. It can be concluded from preceding studies that the FLC can regulate the HEPS to operate around its pre-specified ideal condition, such as the best system efficiency, the lowest emissions and the minimum fuel usage. In addition, fuzzy logic based methods are insensitive to model uncertainties and are robust against the measurement of noises and disturbance [117,118].

In sum, the rule-based controls are made up of a series of logic statements and predefined criteria, thereby being easily implemented in practice. However, the set of logic rules is usually designed based on the human expertise and engineering intuition. Accordingly, the development of rule-based energy management strategy is usually time-consuming and experience-dependent. Furthermore, since the rule-based control cannot give any necessary or sufficient conditions for the control to be optimal, the optimality of solutions cannot be guaranteed.

2.3.2.2 Optimization-based One

The optimization-based strategy becomes more and more attracting, as its optimality can be, to some extent, supported by the theoretical basis. The difference between the non-causal and causal optimization is that the latter one does not need the future information. Many studies have found that the non-casual optimization problem can be converted to a causal optimization problem based on optimal control theories.

Pontryagin's Maximum Principle: The Pontryagin's Maximum Principle (PMP) is a classic optimal control approach. It can find the best possible control for the original non-causal problem, by solving several causal functions. The primary benefit of PMP is that it can provide the necessary condition for the solution to be the optimal control of the original non-causal problem. Basically, the PMP can be taken as an approach of converting a non-causal optimization to the corresponding Hamiltonian function minimization. Another advantage of PMP is that it can give the analytical solution of energy optimization problems [122,123]. The optimization constraints can be represented by the algebraic equations. Kim, et al., [124][125] demonstrated the conditions of reaching the global optimality for PMP.

The Hamiltonian function can be minimized instantaneously using current information, if the initial co-state value is pre-known. However, the future information is requested to estimate the optimal value of initial co-state. Otherwise, the system state (the battery

SoC) may not reach its ideal value at the end of the mission. This limits the application of PMP in the on-line implementation. Some studies around PMP is how to estimate the initial co-state. Delprat et al. [126] applied the dichotic search to off-line optimize its Lagrangian multipliers. Less than ten iterations were requested to converge to the optimal point. Serrao et al. [122] employed the same approach to estimate the initial co-state value. On the other hand, some researches took advantage of the inner relationship between PMP and DP [127,128]. In other words, the optimal co-state is related to the optimal cost-to-go result from DP. However, the above-mentioned approaches all need future information of the mission, since generally implemented on the off-line optimizations. Moreover, the optimal value of initial co-state varies depending on the driving cycles.

The application of PMP makes the real-time energy optimization theoretically feasible. Still large computational cost exists due to nonlinear and nonconvex characteristics of the optimization problem. To reduce the computational loads, various approximations are applied to the simplification of the original problem. Ambuhl et al. [129] implemented a quadratic approximation on both the engine fuel rate and the electric powertrain efficiency. Koot et al. [96] described the energy optimization problem using the quadratic programming structure. It reduces the time consumed of optimization, compared with the DP. The work of Tate and Boyd [93] converted the original nonconvex problem to a large linear programming problem, by approximating the fuel map and battery losses with linear models. To overcome the deficiency of the above-mentioned fitting method, Hou et al. [62] firstly proposed a piecewise linear approximation to fit the fuel rate map. The distortion of the fuel rate map was successfully avoided by considering the turning point of efficiency.

Equivalent Consumption Minimization Strategy: The Equivalent Consumption Minimization Strategy (ECMS) is one of the most promising causal optimizations since proposed by Paganelli [130]. It can be considered as the extension of PMP by replacing the co-state variable with the so-called equivalence factor [131]. Then the Hamiltonian function is converted to a new objective—the equivalent consumption. This new objective has a real physical meaning as the sum of actual fuel consumption from ICE and equivalent electric energy consumption from the battery.

The first challenge of the ECMS is to estimate the equivalence factor. Since the equivalence factor is essentially related to the co-state variable of PMP, the researchers first applied the Hamilton-Jacobi-Bellman equation to predict the

equivalence factor [128,132]. However, this approach requests the optimal cost-to-go result from DP. Put differently, a-priori knowledge of mission has to be known to estimate the equivalence factor. This sacrifices the advantage of causal optimization. Some studies implemented other methods to off-line evaluate the optimal equivalence factor. Ref. [133] optimized the corresponding equivalent discharging/charging factor using the genetic algorithm, before implementing the ECMS on-line. If the minimization of equivalent consumption was considered as a multi-objective optimization problem, the equivalence factor could be estimated from the Pareto front [134].

Unfortunately, those approaches all need future information about the system. Moreover, the optimality of equivalence factor is heavily dependent on the driving cycles. Therefore, many studies start to approximate the equivalence factor according to its physical meaning. Since the equivalence factor can be interpreted as the equivalent amount of fuel represented by a given amount of electrical energy, it can be evaluated using the specific fuel usage of engine and the efficiency of electrical component [135–137].

The key issue with the ECMS, when applied in real-time, is that it cannot sustain the battery SoC due to the equivalence factor being evaluated off-line [132]. As a consequence, the Adaptive-ECMS (A-ECMS) have been addressed to regulate the equivalence factor on-line. Generally, A-ECMS can be classified into two kinds. The first one is to update the original equivalence factor with a correction term regarding the SoC value. At the beginning of the establishment of the concept of equivalence factor, the penalty function was already applied to regulate the SoC behaviour [138]. The control variable was corrected by the penalty function if the SoC deviates from its desired value. The commonest way to adaptively update the equivalence factor was to adopt the P or PI controller [139,140]. The input of the controller was the error between the current SoC and desired SoC. Ref. [137] compared the results of different methods for the SoC correction.

The second category of A-ECMS, sometimes, is also called as predictive ECMS, since it needs to predict the future information on-line. A neural network based velocity predictor was constructed by Ref. [141] to forecast the short-term future driving behaviours by learning the data stored in 3-D maps. Instead of keeping updating the optimal equivalent factor, Ref. [142] demonstrated an approach to estimate the upper and lower bounds of the optimal equivalent factor, which were independent of drive cycles. The second category of A-ECMS is obviously more advanced, but it suffers

from larger computational cost when implementing the optimization and profile forecast simultaneously. This approach might be a good compromise for ground vehicle, but still not ideal for aircraft.

The aforementioned A-ECMS algorithms aim to realize the charge-sustaining strategy [138], which is typical of hybrid ground vehicles. However, the charge-sustaining strategy is not ideal for aerial vehicle applications [143]. If the SoC is sustained at a very low level, the residual battery capacity cannot guarantee a safe landing when there is a failure of the engine; on the other hand, maintaining a high-level SoC, means full use cannot be made of the electrical energy in the battery. Therefore, for aircraft, it is better that the SoC is held within a range instead of at a specific value. The most intuitive way is to combine the ECMS with a rule-based control [135,144], since the desired SoC requirement can be achieved using logic rules. This means, the control performance will not be heavily dependent on the selection of equivalence factor.

2.3.3 Summary

The brief review of non-causal and causal energy management strategy for HEPS is presented above. Compared with the causal approaches, the non-causal energy management is generally preferred for off-line applications, since it requests the complete information of missions. The non-causal optimization can also be taken as the benchmark for causal approaches, since it can reach time-global optimal trajectories of control variables and system states. Meanwhile, the non-causal control may be applied to the on-line mission where the upcoming mission profile is priori-known or predictable.

On the other hand, the causal strategy has less limitation since it only requires the current or past system information. However, an instantaneous optimization cannot guarantee the time-global optimum along the complete mission. Furthermore, the causal control commonly cannot meet the requirement of system states (for example the final state), since the future information is not considered in the algorithm.

Basically, the non-causal and causal energy management are preferred under different circumstances. If the flight mission varies depending on the flight environment, the causal control needs to be adopted to update control variables on-line. If a specific sub-task is demanded for the part of the future flight, the non-causal control is preferred to

achieve the optimal results, since all information about this sub-task is previously known. Therefore, both the non-causal and causal control are required to complete a complicated mission.

2.4 Conclusion

A multi-objective optimization—NSGA will be applied to size the hybrid propulsion system, since it can simultaneously optimize several objectives. A new non-dominated sorting algorithm is needed to reduce the computational complexity of NSGA. The newly proposed approach will be developed based on the ENS algorithm.

Both the non-causal and causal energy management have their advantages and disadvantages and are worth further studying. For the non-causal control, the convex programming will be studied, where a new convexification approach is needed to simplify the original non-causal problem. For the causal control, the ruled-based ECMS optimization will be proposed to transform the original non-causal problem to the causal problem, and solve the equivalence factor issue. In this study, as opposed to previously published articles, the fuzzy rules will be performed to improve the robustness of the supervisory control to system uncertainties.

3 Design

This chapter aims to design a hybrid electric propulsion system for the prototype aircraft. Parameters, including the weight, maximum power or energy capacity of the main components in the propulsion system are optimized using the system sizing.

The system design starts by first covering the analysis of the prototype aircraft. The performance requirements are evaluated on the basis of the aerodynamics of prototype airframe. The power-weight models of different sorts of engines and motors are also established and compared. A high-level parallel configuration is presented before the system sizing.

The system sizing is formulated as a multi-objective optimization problem with two contradictory objectives. The fuel consumption is minimized while the flight duration is maximized. Then, a new non-dominated sorting algorithm is proposed, and its computational complexity is analysed. The constraint handling is integrated into the original Non-dominated Sorting Genetic Algorithm (NSGA) to address the optimization constraints (performance requirements). The preferred solution from the Pareto front is evaluated. This preferred solution is also set as the configuration of the hybrid propulsion system for the prototype aircraft.

In the next two sections, the performance of hybrid aircraft is verified by comparing with the prototype aircraft. The sensitivity of optimization results to the variation of optimization parameters, system parameters and aircraft performance is further discussed. The main propulsion components are selected among off-the-shelf products on the basis of the preferred optimal solution.

3.1 Prototype Aircraft

The prototype aircraft is developed based on Ercoupe, first manufactured by the Engineering and Research Corporation (ERCO). It is a low-wing monoplane aircraft and usually equipped with Continental combustion engine from 48 kW to 67 kW. In this study, a Continental C-75-12 powered model is selected as the template of prototype aircraft. The basic properties and performance of the prototype aircraft are given in Table 3-1. The Maximum Take-Off Weight (MTOW) is 572 kg when the 56 kW Continental engine used. Some of the parameters are explicitly used in the following sections, so their symbols are also given in the table.

Table 3-1 Basic Properties

Prototype Aircraft		Symbol	Value
Airframe	Wingspan	-	9.1 m
	Length	-	6.3 m
	Height	-	1.8 m
	Wing area	S	13.3 m^2
	Aspect ratio	AR	6.23
	Airfoil	-	NACA 43013
Performance	Maximum speed	-	177 km/h
	Range speed	-	118 km/h
	Endurance speed	-	90 km/h
	Stall speed	-	77 km/h
	Rate of climb	R_c	2.8 m/s
	Take-off distance	d_{tkof}	230 m
	Endurance duration	-	2-3 h
Others	MTOW	-	572 kg
	Engine power	-	56 kW

3.1.1 Aerodynamics

The aerodynamic analysis provides the drag polar, which is directly related to the required thrust and power for the aircraft. It has a significant impact on the propulsion system sizing and therefore has to be analysed in some detail. The drag polar suggests the relationship between the lift coefficient and drag coefficient. It can be expressed as an equation in terms of the drag coefficient on the lift coefficient:

$$C_D = C_{D,0} + \frac{(C_L - C_{L,0})^2}{\pi e AR}, \quad \textbf{(3-1)}$$

where $C_{D,0}$ is the zero-lift parasite drag coefficient, AR is the aspect ratio, and e is the Oswald efficiency factor typically between 0.7 and 0.85 [145]. The minimum-drag lift coefficient $C_{L,0}$ is introduced to reflect the truth that the parasite drag is slightly higher than the minimum drag [146].

The parasite drag is a consistent percentage of the skin-friction drag, so the parasite drag coefficient can be addressed by $C_{D,0} = C_{f_e} \frac{S_{wet}}{S}$, where C_{f_e} represents the skin friction coefficient and its estimated value is given by Ref. [145] for mid-scale aircraft. Aircraft wetted area S_{wet} can be calculated by the actual exposed planform area, while S refers to wing area.

The minimum-drag lift coefficient $C_{L,0}$ can be calculated using the minimum lift, which occurs at the maximum speed based on the following relation:

$$C_L = \frac{2W_g}{\rho_\infty V_\infty^2 S}, \quad \textbf{(3-2)}$$

for steady flight, in which ρ_∞ and V_∞ can be any available chosen values. And W_g represents the global weight of aircraft. Similarly, the coefficient $C_{L,max}$ is acquired by using the stall speed.

The endurance speed is corresponding to the maximum endurance duration, which requests the minimum power from the propulsion system. Put differently, the aircraft achieves the maximum $C_L^{3/2}/C_D$ at the endurance speed [146]. Combining $C_L^{3/2}/C_D$ with Eq. (3-1), the lift coefficient at endurance speed $C_{L,endur}$ can be obtained. On the other

hand, the range speed refers to the speed leading to the maximum range, flying at the maximum C_L/C_D [146]. Similar to the endurance speed, the lift coefficient at range speed $C_{L,rang}$ can be calculated using Eq. (3-1).

3.1.2 Airspeed and Power Requirements

The aircraft when retrofitted will be required to meet a number of performance targets, such as the requirements of airspeed and propulsion power.

The first will be that the endurance speed will have an adequate safety margin above the stall speed. As mentioned in Eq. (3-2), the aircraft flight speed is determined by the lift coefficient and the wing loading, for steady-level flight $V_\infty = (2W_g/\rho_\infty C_L S)^{1/2}$. Therefore, the stall speed V_{stall}, endurance speed V_{endur}, and range speed V_{range} of hybrid powered aircraft can be calculated by substituting their lift coefficients, respectively.

Though those three speed is vital for identifying the performance of aircraft, the ideal cruising speed usually is none of them. The range speed is known as the most fuel economy speed, but generally too slow for aircraft cruising. This thesis introduces Carson's Speed [147] as the optimum cruising speed, since this speed desires to achieve the minimum additional fuel consumption compared with the real minimum one. Unless otherwise stated, the cruising speed V_{cruise} used in the thesis would be Carson's Speed. The relation between Carson's Speed and the range speed is $V_{cruise} = 3^{1/4} V_{range}$.

Secondly, the minimum and maximum power requirements also need to be determined, and for steady-level flight, the power requirement is expressed by:

$$P_{rd} = \sqrt{\frac{2W_g^3}{\rho_\infty S}} \cdot \frac{C_D}{C_L^{3/2}}. \quad \textbf{(3-3)}$$

Using Eq. (3-3), the power needed for the steady-level flight at different airspeeds (like P_{endur}) can be obtained. The power at the endurance speed is the minimum power demanded for steady-level flight, i.e. $P_{min} = P_{endur}$.

On the other hand, the maximum power requirement is dependent on the take-off and climbing performance, mainly featured by the take-off roll and Rate of Climb (RoC).

For a reciprocating engine/propeller combination, the power is reasonably constant at the take-off phase. Neglecting the rolling resistance and using average thrust and drag, the specifying take-off distance can be expressed as:

$$d_{tkof} = \frac{W_g V_{LO}^2}{2g(F_{avg} - D_{avg})}, \quad \textbf{(3-4)}$$

where g is the acceleration of gravity. The lift-off velocity V_{LO} should be no less than $1.1V_{stall}$ [146]. T_{avg} and D_{avg} are equal to their values at $0.7V_{LO}$, respectively. Therefore, the take-off power P_{tkof} can be estimated using $P_{tkof} = T_{avg} \cdot 0.7V_{LO}$.

Climbing to a higher altitude at a certain rate is another important characteristic of aircraft performance. R_c is a function of excess power, which is the difference between available power (P_{climb}) and the power required to overcome drag (P_{rd}):

$$R_c = \frac{P_{climb} - P_{rd}}{W_g}, \quad \textbf{(3-5)}$$

Here, the power demanded for cruising, P_{cruise}, not minimum power required, is taken to represent the power required (P_{rd}). Thus, the power available for climbing can be addressed by: $P_{climb} = P_{cruise} + R_c \cdot W_g$.

3.1.3 Weight Models

From the equations in the previous section, all performance of aircraft depends on its global weight. The global weight of aircraft mainly consists of the weight of propulsion system and airframe with other devices (avionics and mechanics etc.). Different from the conventional propulsion system, an HEPS includes both engine and electric motor. The weight of engine and motor increases with the growth of its power capability.

This study compares the weight models as the function of maximum power, between two types of reciprocating engines. As shown in Figure 3-1, the rotary engine has higher power-to-weight ratio than the piston engine with 1-3 cylinders, when the engine

output capability is under 100 kW. Between 30 kW and 90 kW, four-cylinder piston engines are also favoured due to less fluctuation of output torque, compared with 1-3 cylinders. However, few 3-4 cylinders are employed in rotary engines during this power range, since the rotary engine can achieve smooth operation with only 1-2 cylinders.

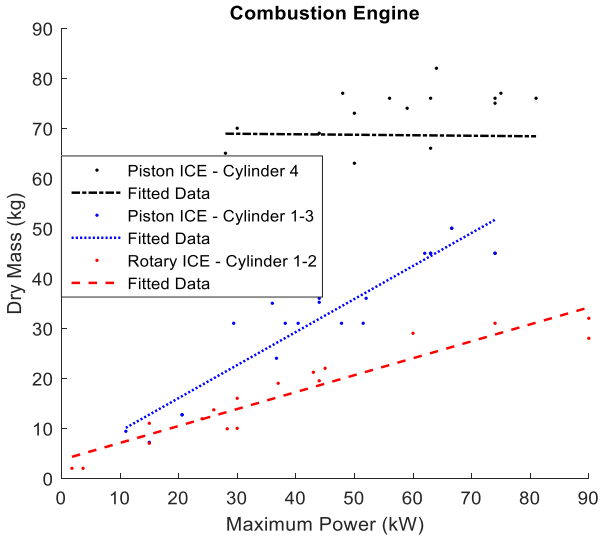

Figure 3-1 Comparison of weight model for different engines

With respect to electric motors, it is well known that BrushLess Direct Current motor (BLDC) and PMSM (PMSG) have better efficiency and power density than the induction motor [148]. The weight models of BLDC and PMSM motors from different companies are given in Figure 3-2. The maximum rotational speed of selected BLDC is around 3000-5000 rpm when without load, while the maximum no-load rpm of selected PMSM is around 5000.

Regarding off-the-shelf motors, the PMSM normally can achieve higher maximum power output than the BLDC. The same type of electric motor from different companies normally have different power densities, but products from the same company show similar values. The fitted lower boundary implies the highest power density of the electric motors (considering BLDC and PMSM) can achieve; while the fitted higher boundary denotes the lowest power density of the electric motors quoted in the thesis.

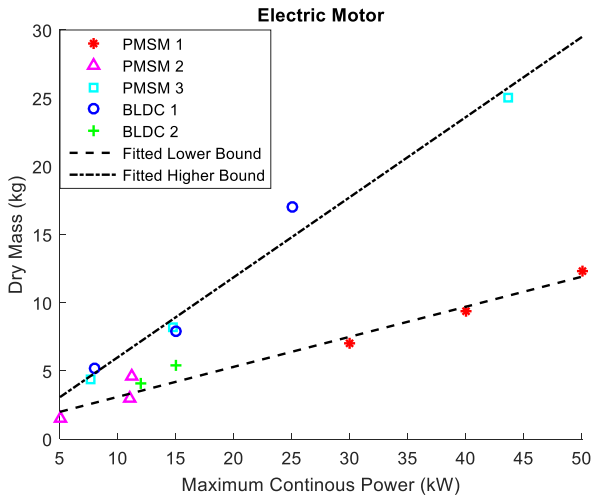

Figure 3-2 Weight model for electric motor

On the other hand, the weight of the motor controller cannot be ignored for high voltage/current one. The fitted results of weight model for the motor controller are also shown in Figure 3-3. In a word, for the aircraft in this study, the rotary engine is more suitable than the piston engine, regardless of cylinders. This thesis also selects PMSM/PMSG with the highest-power-density.

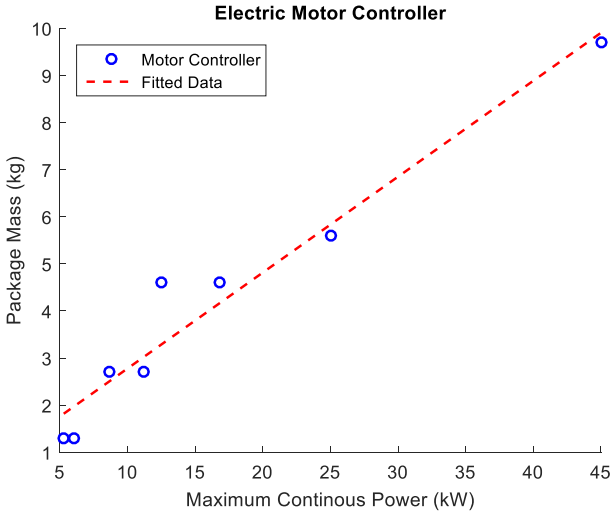

Figure 3-3 Weight model for the controller of electric motor

3.2 Configuration

There are various hybrid powertrain configurations currently in use. The most commonly used configurations are series, parallel and series-parallel architecture. Of

these, the series architecture enables the engine to operate at its ideal operating condition. However, its system efficiency is relatively low since large energy losses exist in the energy conversion [149]. Also, the series configuration cannot achieve a combination of combustion and electrical power. The series-parallel is the most functional structure of the three architectures. Nevertheless, its complicated clutch/gear mechanism raises the issue of reliability on real aircraft applications. Compared with the series-parallel configuration, the parallel configuration is lighter and less complex, whilst keeping the flexibility of hybridization. According to the work by Harmon [150] and Hiserote [45], the single-shaft parallel configuration is best suited for small- and medium-scale aircraft.

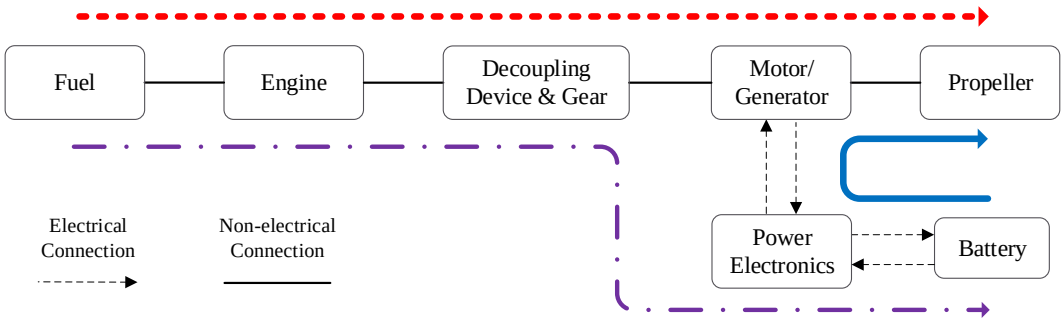

Figure 3-4 Parallel configuration of HEPS

The high-level diagram of the parallel hybrid propulsion system developed in this study is shown in Figure 3-4. The energy/power flows between the combustion and electric powertrains are indicated by the red, purple and blue line around blocks. The red dotted line represents the fuel flow to the engine and the corresponding power to drive the propeller, while the purple dashed line denotes the engine power used to charge the battery. The electric power supporting the propeller driving is represented by the blue solid line.

The output shaft of the engine and the input shaft of the motor/generator are connected through a decoupling device and reduction gear. The energy needed by the motor is supplied by a battery with the integrated power electronics. This setup enables the system to combine the power from engine and motor/generator, when the power demand exceeds that which can be provided by only one of the propulsive units. Otherwise, when the power demand is lower than the maximum engine power, the motor/generator can draw power from the engine to charge the battery. Moreover, this architecture also permits the motor to drive the propeller alone, if electric-only flight

mode is required. The hybrid architecture has the property that it is fault-tolerant. In the case of a failure of one of the propulsion units, it can de-couple the combustion drivetrain or shut down the electric power supply, so that one of the working units will continue driving the propeller.

3.3 Propulsion System Sizing

This section will firstly formulate the sizing of hybrid propulsion system into a standard multi-objective optimization problem. As explained in Section 2.2, the (quasi-) static models are employed in the study of propulsion system sizing.

3.3.1 Objectives and Variables

Different from the traditional propulsion system, the hybrid one has two additional parameters that determine its capability—hybrid of power and hybrid of energy. The former one is normally called Degree of Hybridization (DoH) [151], which compares the maximum installed power between the engine and electric motor; while the latter parameter reveals the ratio of energy storage from two sources. In other words, the maximum power of the engine and electric motor, and the energy storage of fuel and battery amount must be taken as the optimized variables. It is more common to refer to the mass of the fuel rather than its energy content since the former provides a more straightforward representation of fuel consumption. Therefore, the mass of fuel and battery are considered as the optimized variables, replacing the energy storage of fuel and battery, respectively.

The fuel mass of a flight mission cycle can be presented as:

$$J = \int_0^{t_f} \dot{m}_{fuel}(P_{ICE})dt, \quad \textbf{(3-6)}$$

where $\dot{m}_{fuel}$ is the rate of fuel usage and t_f is the end time of flight.

From Eq. (3-6), the total fuel consumption mainly depends on the power drawn from the engine and the flight duration. The instantaneous engine power P_{ICE} is generally related to the power requirement P_{req} using the power-split variable σ_p, and so σ_p has

to be considered as variable to be optimized. Note that σ_p is time-variant and $P_{ICE}(t) = (1 - \sigma_p(t)) \cdot P_{req}(t)$.

Eq. (3-6) shows that one can minimize fuel consumption by reducing either or both flight duration t_f and engine power P_{ICE}. However, the flight time is a variable that every designer desires to maximize. Thus, fuel consumption m_{fuel} and flight duration t_f should be considered as contradictory objectives.

In brief, the optimized variables consist of the maximum engine power $P_{ICE,max}$, the maximum motor power $P_{EM,max}$, fuel mass m_{fuel}, battery mass m_{batt}, flight duration t_f, and power-split variable σ_p. Two objective functions are defined by:

$$\min f_1 = m_{fuel}, \tag{3-7}$$

$$\min f_2 = -t_f.$$

3.3.2 Constraints

One of the constraints of sizing hybrid propulsion system is that the performance of the prototype aircraft cannot be significantly compromised. Specifically, the take-off and climbing performance are requested not to be sacrificed. In other words, the hybrid aircraft has to achieve larger RoC and shorter take-off distance, or at least the same value. The typical stall and endurance speed are not fixed, but the difference between those two values has to be maintained (see Eq. (3-8)).

Furthermore, the hybrid propulsion system has to meet other mission requirements, such as electric-only cruising and battery charging. Therefore, a certain amount of on-board fuel and electrical energy source (battery) is also needed to complete the whole flight mission.

In sum, all performance and mission requirements can be categorized into three points: airspeed requirement, power requirements, and energy requirements. All of them can be governed by the inequality constraints expressed by Eqs. (3-8)-(3-13).

$$V_{stall} + \Delta V \leq V_{endur}, \tag{3-8}$$

$$(P_{ICE,max} \cdot e_{air} + P_{EM,max} \cdot e_{elec}) \cdot e_{mech} \geq max\{P_{takof}, P_{climb}\}, \tag{3-9}$$

$$P_{EM,max} \cdot e_{elec} \cdot e_{mech} \geq P_{min}, \tag{3-10}$$

$$P_{ICE,max} \cdot e_{air} \cdot e_{mech} \geq max\left\{P_{cruise} \cdot \left(1 - \sigma_p(t)\right)\right\}, \tag{3-11}$$

$$m_{fuel} \geq \frac{E_{fuel}}{e_{air} \cdot e_{mech}} \cdot \varepsilon_f, \tag{3-12}$$

$$m_{batt} \geq \frac{E_{batt}}{e_{elec} \cdot e_{mech}} \cdot \frac{1}{\varepsilon_b}. \tag{3-13}$$

Eq. (3-9) guarantees that the combination of the maximum engine and motor power can satisfy the take-off and climbing requirements. e_{air} is an altitude-related factor for correcting the engine output capability. e_{elec} consists of the motor, DC/DC efficiency and battery efficiency. e_{mech} represents the mechanical efficiency mainly affected by the propeller. Eq. (3-10) means the electric motor has the ability to power the aircraft by itself; while Eq. (3-11) ensures that the engine has extra power to charge the battery during the cruising, if necessary.

With regards to Eqs. (3-12) and (3-13), E_{fuel} and E_{batt} denotes the consumed fuel and battery energy, respectively. The total fuel consumption is equal to the fuel used during the flight; while the battery energy storage has to cover the additional usage for the emergency condition, such as engine failure. The calculations of consumed fuel and battery energy are addressed by Eqs. (3-14) and (3-15):

$$E_{fuel} = \int_0^{t_f} \left(P_{ICE}(t)\right) dt = \int_0^{t_f} \left(P_{req}(t) \cdot \left(1 - \sigma_p(t)\right)\right) dt, \tag{3-14}$$

$$E_{batt} = \int_0^{t_f} \left(P_{EM}(t)\right) dt = \int_0^{t_f} \left(P_{\mathrm{req}}(t) \cdot \sigma_p(t)\right) dt + \int_0^{t_{emerg}} (P_{min}) dt, \tag{3-15}$$

where power requirements $P_{req}(t)$ changes at different flight phase, for example $P_{req}(t) = P_{climb}$ during the climbing period. ε_f is the Specific Fuel Consumption (SFC)

of the engine, while ε_b is the energy density of the battery. The emergency time t_{emerg} represents the time duration for aircraft safe-landing using the electric power source. This parameter (t_{emerg}) can also be considered as the maximum time for continuously electric-only fly.

3.4 Non-dominated Sorting Genetic Algorithm

NSGA is one of the multi-objective evolutionary algorithms that can find multiple Pareto-optimal solutions in one single simulation run. As one of the first such proposed evolutionary algorithms, the NSGA approach has been widely used though some shortage had been concerned [52]. To address these issues, the same research group led by Kalyanmoy Deb proposed an elitist version–NSGA-II [52] in 2002.

The development of the optimization algorithm in this thesis is based on an open source NSGA-II programmed by Aravind Seshadri [152]. Some changes are made to improve the computing efficiency. A new non-dominated sorting algorithm is developed to replace the FNS approach by Kalyanmoy Deb [52]. Also, the constraint handling is incorporated into the program.

3.4.1 Non-dominated Sorting Algorithm

Non-dominated sorting is a procedure where solutions in the population are assigned to different Pareto fronts based on their dominance relationships. It plays a critical role in the sorting operation of the NSGA. Note that the strong dominance definition [56] is used in this thesis. If there is no any other individual/solution whose objectives are all better than this solution, this solution is the non-dominated solution in the population.

Assume that the individuals in the population P can be categorized into K fronts, denoted as F_i, $1 \leq i \leq K$. According to the non-dominated sorting, all non-dominated solutions in P are first assigned to the front F_1; then, the non-dominated solutions in $P - F_1$, are assigned to F_2. This procedure repeats until all solutions in P are assigned to a front F_i, $1 \leq i \leq K$.

Non-dominated sorting can acquire multiple fronts in one simulation run, but its operation is computationally intensive. Dominance comparisons between the solutions

are the main operation in the non-dominated sorting. The interesting factor is that many dominance comparisons between solutions are unnecessary and can be spared. As illustrated in the Ref. [57], one dominance comparison can be categorized into the following four cases, when the solution p_m is compared with the solution p_n:

1) Case 1: p_m is dominated by p_n, or p_n is dominated by p_m;
2) Case 2: p_m and p_n are non-dominated, and they belong to the same front F_i, where F_i is the current front;
3) Case 3: p_m and p_n are non-dominated, and they belong to the same front F_i, where F_i is not the current front;
4) Case 4: p_m and p_n are non-dominated, but they belong to different fronts.

For non-dominated sorting, comparisons in Case 1 and comparisons in Case 2 cannot be avoided. Thus, they are termed necessary comparisons. Most of the comparisons in Cases 3 and 4 are unnecessary comparisons. The necessary comparisons in Case 1 refer to the comparisons between solutions in different fronts, while the necessary comparisons in Case 2 refer to comparisons between solutions in the same front. The number of necessary comparisons in Cases 1 and 2 is the theoretical minimum number of needed dominance comparisons for any non-dominated sorting algorithm. Unfortunately, most popular non-dominated sorting approaches have a total number of dominance comparisons much higher than this minimum number. The reason is that those non-dominated sorting algorithm cannot avoid the unnecessary comparisons existing in Cases 3 and 4.

To improve the computational efficiency, many existing non-dominated sorting algorithms focus on the reduction of the number of unnecessary comparisons. The new non-dominated sorting algorithm proposed in this thesis can further reduce the unnecessary comparisons belonging to Cases 3 and 4.

3.4.1.1 Hierarchical Non-Dominated Sort Framework

ENS strategy was proposed in 2015 [57] and referenced by many studies, since it can considerably reduce the number of unnecessary comparisons existing in Cases 3 and 4. The chief merit of ENS is that it determines the front to which each solution belongs separately. Consequently, a solution to be assigned only needs to be compared with solutions that have already been assigned to a front.

Hierarchical Non-Dominated Sort (HNDS) algorithm was proposed in 2017 [153], also based on ENS. The HNDS first sorts all candidate solutions in ascending order by their first objective. Then it compares the first solution with all others one by one to make a rapid distinction to decide if this solution belongs to the current front. The HNDS was proved to be more computationally efficient than the FNS, Arena's principle and deductive sort. The operation of HNDS is illustrated as follows.

Before conducting the sorting algorithm, the n solutions in the population P are sorted in an ascending order according to the first objective value. The sorted solution is contained in the set Q. If the first objective values of two solutions are the same, then they are sorted according to the second objective value. This procedure continues until all individuals in the population are sorted. If solutions have the same value in all objectives, their order can be arbitrary. Since all the solutions are sorted by one objective, the following conclusions can be inferred: 1) the first solution must belong to the current front; 2) the succeeding solution can never dominate the preceding solution; 3) if a succeeding solution is not dominated by the preceding solution, the remaining objectives of this succeeding solution cannot be worse than the remaining objectives of the preceding solution.

To find the solutions in the set Q that belongs to the current front F_k, HNDS divided the comparison into several rounds. In the first round, the algorithm assigns the first solution to the current set and compares the first solution with all succeeding solutions. The succeeding solutions dominated by the first solution are discarded and allocated to the set R, since they are determined to not belong to the current front. On the other hand, the solutions not dominated by the first solution need another round to determine if they belong to this front. The algorithm moves these non-dominated solutions to a new set Q and starts the second round comparison. The same procedures as the first round are performed in the second round. More discarded solutions are transferred to the set R and another new set Q is created for the third round comparison. This comparison loop will be repeated until the new set Q becomes empty. All solutions in the current front are identified during each round. To start the determination of the next front, the solutions in set R is assigned to the set Q.

An example is given in Figure 3-5. Each circle stands for one solution. Without loss of generality, assume that each solution has two objectives and the number shown in the circle is the value of the second objective. Also, if the number in the circle is 6, we term this circle solution 6. The first solution of each round, highlighted by the red colour, belong to the current front. As shown in Figure 3-5, solution 6 is the first one of set Q and must be assigned to the current front F_k. For the remaining solutions, solutions 3, 1, 2 and 5 are non-dominated by solution 6 and allocated to the new set Q, while solutions 9 and 7 are discarded and assigned to the set R. In the second round comparison, except for the first solution (solution 3), solutions 1 and 2 belong to the next new set Q, while solution 5 has to be discarded. For the third round, solution 2 is finally allocated to the set R and listed after solution 5. It is clear that HNDS may leads to the disorder of the original sequence of solutions. Therefore, sorting of the set R according to the first objective value is also requested before the next front screening.

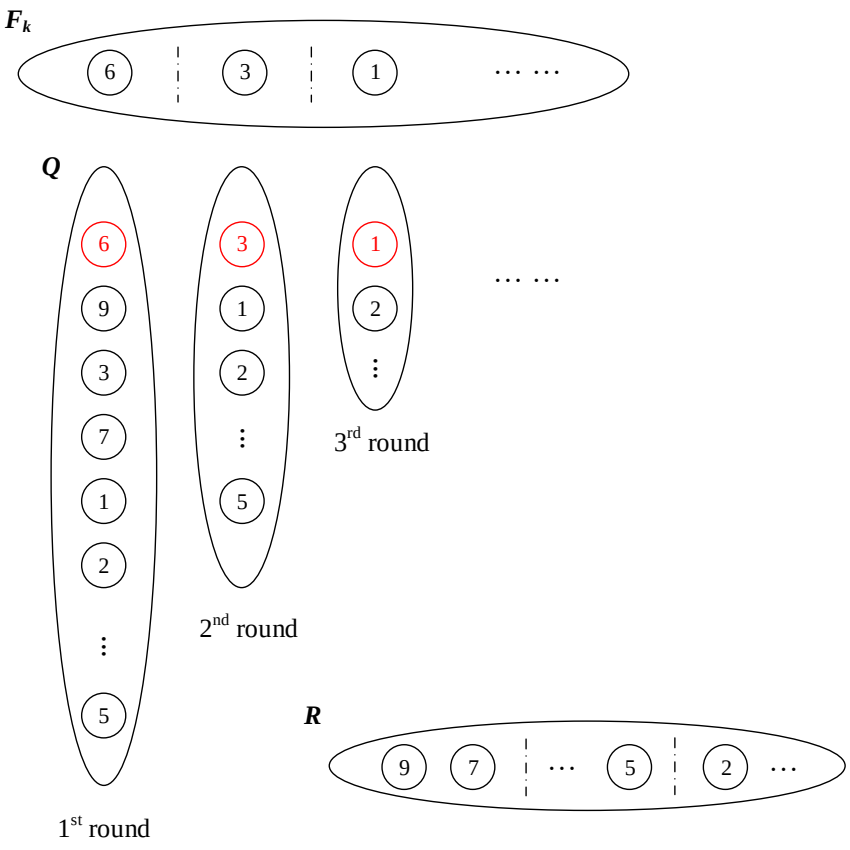

Figure 3-5 Hierarchical non-dominated sort algorithm

3.4.1.2 New Algorithm

HNDS can avoid lots of dominance comparisons between solutions in different fronts. However, it still performs many unnecessary comparisons, since it enforces the comparisons between the first solution and all succeeding solutions. In this study, the idea of the benchmark solution is proposed to reduce the unnecessary comparisons further. Our algorithm can also be classified into several rounds. In the first round, the first solution in the set Q is included in the current front and selected as the benchmark solution. Different from HNDS, the first solution will be compared with the succeeding solutions until the first non-dominated solution occurs. Then, this non-dominated solution is included in the current front and assigned as the new benchmark solution, which means that the second round comparison starts. The loop end condition is the same as HNDS. The pseudocode of the new non-dominated sorting algorithm is presented in Table 3-2.

Table 3-2 A new non-dominated sorting algorithm

Algorithm 1: Find the current front set F_k

Input: The solution set Q with sorted individuals; Q is not an empty set

Output: The current front F_k

$F_k = \{Q[1]\}$; {assign the first solution to the current front}

$R = \{\ \}$; {the set containing solutions not belonging to the current front}

$n = length\{Q\}$; {the number of solutions in the solution set}

$i = 1$; {the number of solutions in the current front}

$s = i$; {the position of the benchmark solution}

$Qs = Q[s]$; {select the first solution as the benchmark}

while $n > 0$ **do**

    $s++$;

    for $j = s{:}n$ **do**

        if $Q[j]$ is non-dominated by Qs **then**

            $F_k = \{F_k, Q[j]\}$;

            $Qs = Q[j]$;

            $s = j$;

            $i++$;

            $n--$;

            break;

        else

            $R = \{R, Q[j]\}$;

$n--$;
end if
end for
end while
$Q = R$ {prepare the solution set for next front run}

Algorithm 1 starts with assigning the first solution to the current front set F_k. Several parameters and sets are also initialized, such as the number of solutions in the solution set and current front, denoted by n and i seperately. The set R contains the solutions not belonging to the current front and is initialized as an empty one. The benchmark Qs is firstly set using the value of the first solution. Then, the while loop of Algorithm 1 separates the solutions non-dominated by Qs and those dominated by Qs, by comparing each solution with the benchmark one. If the solution and the benchmark Qs is non-dominated by each other, this solution is included in the current front set F_k and assigned as the new benchmark. The number of solutions in the current front (i) is also increased by one. Conversely, if Qs can dominate the solution, then this solution has to be discarded and contained in the set R. The number of solutions in the solution set (n) will be decreased by one after each comparison. Therefore, the while loop can continue until n becomes zero. Finally, the set R is assigned to new solution set and needs to be compared again at the sorting of next front.

An example is given in Figure 3-6. The benchmark solution Qs of each round is highlighted by the red colour. Solutions 6, 3, and 1 are set as benchmark, respectively and all belong to the current front F_k. Solution 6 is the first benchmark solution. Solution 9 is dominated by solution 6 and allocated to the set R. Since solution 3 is non-dominated by solution 6, it is directly assigned to the current front and set as the new Qs. This indicates the beginning of the second round. For the next second round, solution 7 is discarded and solution 1 is selected as the new benchmark. In the third round comparison, solutions 2 and 5 are all discarded since they are dominated by solution 1. Note that our new algorithm can keep the original sequence between solution 2 and 5. Therefore, the operation of re-sorting of the set R can be avoided.

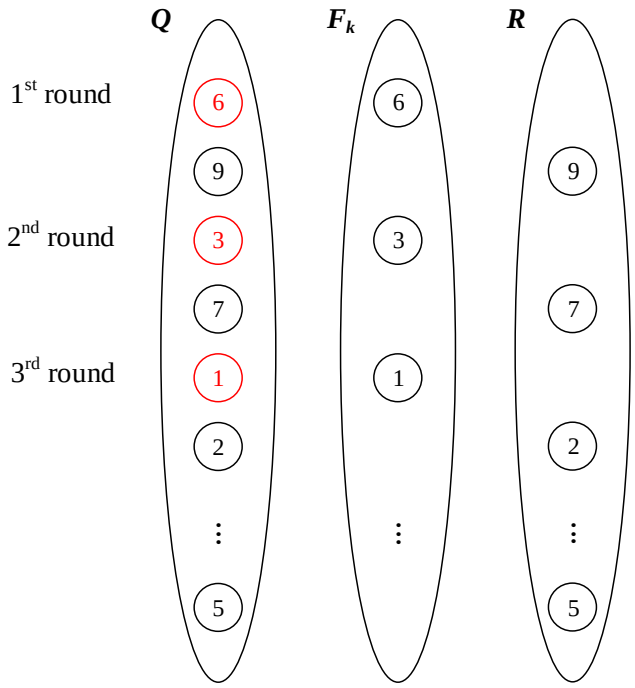

Figure 3-6 New non-dominated sort algorithm

The proposed algorithm has several advantages, in addition to HNDS: 1) at each round comparison, creating new set Q is not needed anymore; 2) the new algorithm will not change the sequence of solution in the set R, overcoming the drawback of HNDS; 3) many unnecessary comparisons are further avoided, since each benchmark solution does not need to be compared with all succeeding solutions; 4) new algorithm is friendly to the comparison between the identical solutions, since the succeeding solution can replace the preceding one to be the new benchmark solution.

The time complexity of the proposed non-dominated sorting algorithm consists of two main parts. First, the initial population is sorted in ascending order according to the first objective. Second, the solutions in the sorted population are compared and assigned to different fronts. The time complexity of the first step is $O(N\ log\ N)$ if 'Merge Sort' is applied. Regarding the second step, the worst case happens when every solution in the sorted population belongs to different fronts and is dominated by its all preceding solutions. In this case, all solutions have to be compared with each other, so the worst time complexity is $O(MN^2)$. For the best case, all solutions in the sorted population are non-dominated by each other and can be assigned to one front. Put differently, each solution only needs to be compared with the one next to it in the sorted population, so the best time complexity is $O(MN)$.

3.4.2 Constraint Handling

The constraint is traditionally handled with the Lagrangian function using the penalty term. If constraints are treated as another cost when implementing non-dominated sorting, the penalty term can be removed. The definition of domination is adjusted so that the solution with a smaller constraint violation has a better rank and feasible solution always dominates the infeasible solution.

The pseudo-code of constrained non-dominated sorting is provided in Table 3-3. Before the while loop of Algorithm 2, the initial population P is separated into the feasible part Q and infeasible part I. Those two parts are sorted according to the first objective value and the constraint violation value, respectively. The front set F is set to be empty. The fronts of feasible solutions Q can be acquired by implementing the while loop. The while loop will call Algorithm 1 to sort out each front F_k, until the solution set Q becomes empty. The executing condition of while loop is realizable since Algorithm 1 will update the solution set Q at each loop. When every solution is assigned to one front, the loop ends. Especially, the executing condition of while loop also ensures that the set Q used in the Algorithm 1 is not empty. Finally, all infeasible solutions are considered to belong to one front, so the set I can be attached at the end of front set F.

Table 3-3 Constrained non-dominated sorting algorithm

Algorithm 2: The main program of constrained non-dominated sorting algorithm

Input: The initial population P

Output: The set of fronts F

Calculate the objective values and constraint violation values of all solutions;

Separate feasible and infeasible solutions;

$Q =$ feasible P;

$I =$ infeasible P;

Sort Q in an ascending order of the first objective value;

Sort I in an ascending order of the constraint violation value;

$F = \{\ \}$;

$k = 1$; {initialize the front number}

while $Q \neq \emptyset$ **do**

$F_k = \{\ \}$;

Find the solutions belonging to the to a front F_k according to **Algorithm 1**;

$F = \{F; F_k\}$;

$k++;$

end while

$F = \{F; I\};$

3.4.3 Discretization

Since NSGA-II is a numerical optimization, all variables dependent on time t are requested to be discretized. As mentioned in Section 3.3.1, optimized variables are $[P_{ICE,max},\ P_{EM,max},\ m_{fuel},\ m_{batt},\ t_f,\ \sigma_p]$, where σ_p is the only one needed to be discretized at specific time nodes t_k, $t_k \in [0, t_f]$. The integer k indicates the number of the node, i.e. $k = 1, \ldots, N$. Following this, constraints are converted to a discrete formation and imposed at the collocation points.

Optimization parameter N is called the number of discretization, which is an index to evaluate the computational burden of one algorithm and have the impact on the accuracy of optimization. The sensitivity of optimization results to the variation of N will be analysed in the Section 3.6.

3.5 Optimization Results

The result of NSGA-II is not a single dominating-optimal point, but a series of feasible solutions that cannot be improved in any of the objectives without degrading at least one of the other objectives. Those solutions do not dominate each other, and the set of them is called the Pareto front or Pareto frontier. This section will give the Pareto front of hybrid propulsion system optimization and select one from all Pareto optimal solutions according to the practical demands. Later, the selected optimal solution and prototype propulsion system is compared. Meanwhile, the performance between the original and hybrid aircraft is also analysed.

Before moving to the optimization results, the boundaries of optimized variables are first provided in Table 3-4. The maximum power of engine and motor are both not allowed to exceed the one of prototype engine. The upper bound of fuel and battery mass is the useful load mass of prototype aircraft, while the lower bound of battery

mass is equal to the prototype battery mass. The feasible value of the duration t_f is not limited between 2-3 h, but a wider range (from 1 h to 5 h) is applied to search more possibilities. The maximum value of power split σ_p cannot be larger than 1 based on the definition of σ_p. On the other hand, since part of engine power should be used to power the aircraft, the power for battery charging cannot be too high. Considering this, the minimum value σ_p is set to -10.

Table 3-4 Variable Bounds

Variable	Lower Bounds	Upper Bounds
$P_{ICE,max}$	0	56 kW
$P_{EM,max}$	0	56 kW
m_{fuel}	0	233 kg
m_{batt}	20 kg	233 kg
t_f	1 h	5 h
σ_p	-10	1

The parameters needed are listed in Table 3-5, reflecting other system requirements and component features. The minimum difference between stall and endurance speed is set as 13 km/h, the same as the prototype aircraft. The minimum time for emergency landing using electrical energy is around 15 minutes, which is estimated based on the landing performance of the prototype aircraft. Generally, the energy density of the Lithium-ion battery is between 110 Wh/kg and 240 Wh/kg, while one of some high-performance cell can be up to 260 Wh/kg [154]. The average value (180 Wh/kg) is selected initially to study the universal situation.

Table 3-5 Parameters

	Symbol	Value
Requirement	ΔV	13 km/h
	t_{emerg}	15 min
Component	ε_b	180 Wh/kg

3.5.1 Pareto Front

The Pareto optimal outcomes in Figure 3-7 show optimal trades of fuel consumption and flight duration. When the duration boundary is restricted between 1 h and 5 h, the minimum fuel mass varies from 10 kg to 60 kg, and higher fuel usage is needed if longer duration intended to complete. To reduce the fuel usage as much as possible and at the same time do not sacrifice the duration performance, the Pareto optimal solution with 3 h duration is selected as the preferred solution.

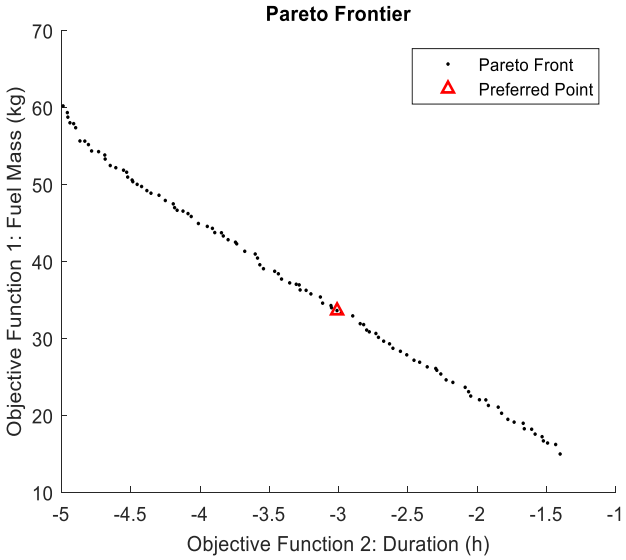

Figure 3-7 Pareto frontier and preferred solution of propulsion system sizing problem

The values of other variables at the Pareto front are also given in Figure 3-8, including the mass of fuel and battery, the maximum power of engine and motor, and the maximum take-off weight. Note that the flight duration variable is displayed monotone increasingly, as well the display of other variables changed correspondingly. The preferred solution is also plotted on each graph using the red triangle. From Figure 3-8 (a) and Figure 3-8 (b), it is evident that the value of fuel mass increases with the duration, while the battery mass has the opposite trend. The MTOW in Figure 3-8 (d) remains relatively stable for different solutions.

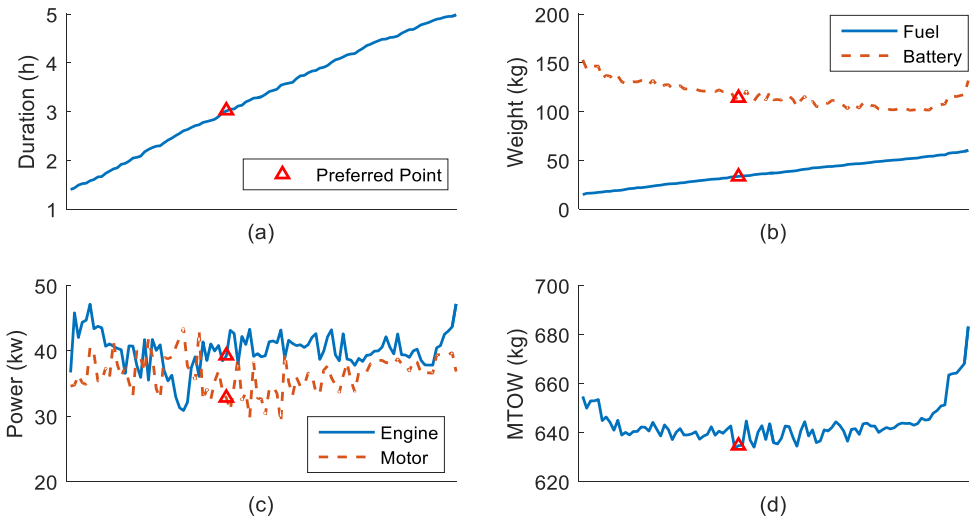

Figure 3-8 Optimization results sorted by the variable–duration

Different from these correlations, the optimized engine and motor power (shown in Figure 3-8 (c)) are weakly related to the duration and fuel/battery mass. This also makes sense since the needed maximum output power mainly depends on take-off and climbing performance and aircraft global weight. Following the same law, the MTOW in Figure 3-8 (d) increases to roughly 680 kg when the maximum engine and motor power (see Figure 3-8 (c)) grows up to 48 kW and 40 kW, respectively. This is also the reason that the battery weight has a slight growth even with the rising of fuel weight and duration.

In sum, the maximum engine and motor power impact little on two objectives. In other words, both the fuel usage and flight duration are not determined by the DoH, while the hybrid of energy is the most significant factor affecting the fuel economy for middle to long endurance flying (above 2 h flight).

3.5.2 Comparison

The details of the preferred solution are listed in Table 3-6. The performance of hybrid powered aircraft is also calculated and compared with the prototype one. The power capability of the hybrid propulsion system is higher than the original one, with the combination of both engine and motor power. Therefore, the hybrid propulsion system can provide the potential for larger take-off weight. Most of the additional weight is used

to carry the battery (114 kg), since the load weight and needed fuel weight are less than ones of the prototype aircraft. It is worth mentioning that the real load capability (190 kg) is not sacrificed when the aircraft is equipped with the hybrid system, since the fuel is generally considered as part of the load.

Table 3-6 Comparison between prototype aircraft and hybrid powered one

		Prototype	Hybrid
Maximum	Engine Power	56 kW	39 kW
Propulsion	Motor Power	0	33 kW
System Power	Total	56 kW	72 kW
Weight	MTOW	572 kg	634 kg
	Load weight	233 kg	223 kg
	Fuel weight	43 kg	33 kg
	Battery weight	10 kg	114 kg
	Additional Gear weight	0	5 kg
Performance	Maximum speed	177 km/h	186 km/h
	Cruise speed	153 km/h	162 km/h
	Rate of climb	2.7 m/s	3.5 m/s
	Take-off roll	230 m	200 m
	Endurance	3.5 h	3.3 h
	Range	452 km	396 km
Fuel Save	300 km Cruising (%)	0	17.3%

Regarding aircraft performance, the hybrid aircraft can achieve higher cruising speed and RoC due to higher power capability. For the same reason, the take-off roll is further minimized to 200 m. The best endurance and range of hybrid powered aircraft are compromised a little with less on-board fuel. However, for the same mission (300 km),

the hybrid propulsion can save 17.3% fuel compared with the conventional combustion engine.

Figure 3-9 compares the weight fraction of components for the original combustion system and HEPS. The weight fraction was calculated using the mass of components and MOTW of aircraft. Firstly, the dry mass (excluding fuel and battery) ratio is given in Figure 3-9 (a). The dry mass of the original propulsion system only includes the engine mass, while hybrid dry components comprise the engine, motor, motor controller and clutch.

The weight fraction of original propulsion system is over twice larger than one of HEPS 'dry' components. This is partly since the electric motor has higher power density than the combustion engine. Another reason is that lower power requirement means a two-cylinder engine can be used instead of the original four-cylinder engine which was much heavier. Even so, the weight of the two-cylinder engine still occupies the highest portion of the whole dry mass, for the hybrid powertrain.

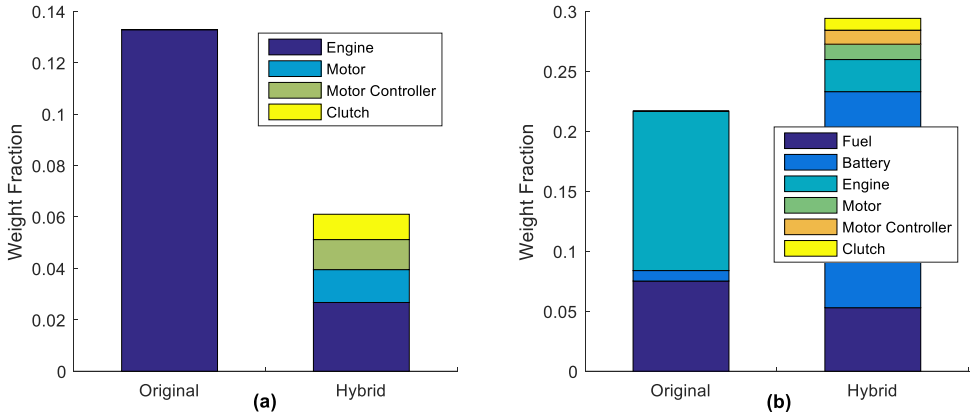

Figure 3-9 Comparison of component weight for original and hybrid propulsion system, regarding the dry mass (a) and total mass (b)

Figure 3-9 (b) provides the weight fraction of the total mass of the original combustion system and HEPS, including both the wet mass (fuel and battery mass) and dry mass. The weight fraction of the total mass of the complete HEPS is higher than for the original propulsion system. Another interesting factor is that for the original combustion system the dry mass takes up the largest ration, while for the HEPS the wet mass consumes most weight. Explicitly, for the original system the engine accounts for over half the total weight, and for the hybrid system it is the battery that accounts for over

half the total weight. It can be concluded that the increase of battery energy density can significantly benefit the reduction of hybrid system weight.

In short, the optimized hybrid electric propulsion system can achieve better fuel economy, without any sacrifice of significant performance (load, take-off and climb capability). Higher cruising speed and RoC are also benefits due to being equipped with the hybrid system. Furthermore, the hybrid propulsion system uses less weight to reach much more power output. Therefore more weight can be exploited to carry the energy source (such as fuel and battery).

3.6 Sensitivity Analysis

This section describes the sensitivity of optimization results to the variation of optimization parameters, system parameters and aircraft performance. Specifically, those parameters are discretization number, battery energy density, emergency time, take-off distance, and RoC. Note that the test case in Section 3.5 is regarded as the benchmark.

3.6.1 Discretization Number

For any numerical optimization involving discretization, the number of discretization would affect the precision of optimization results. Generally, larger discretization number gives a more accurate solution but also leads to heavier computational burden. As mentioned in Section 3.4.3, σ_p is the only variable needed to be discretized, so the discretization number of σ_p is equal to discretization number of the optimization problem. The value of σ_p should be different at take-off, climbing and cruising phase. Therefore, the minimum discretization number for the analysis test can be given by $N = 3$. The Pareto front results of test cases with the minimum number and other three larger numbers are graphed in Figure 3-10. Here, the frontier with $N = 12$ is the optimization result in the Section 3.5 and highlighted with the underline. It is clear that the precision of the Pareto front does not sacrifice much with smaller discretization number.

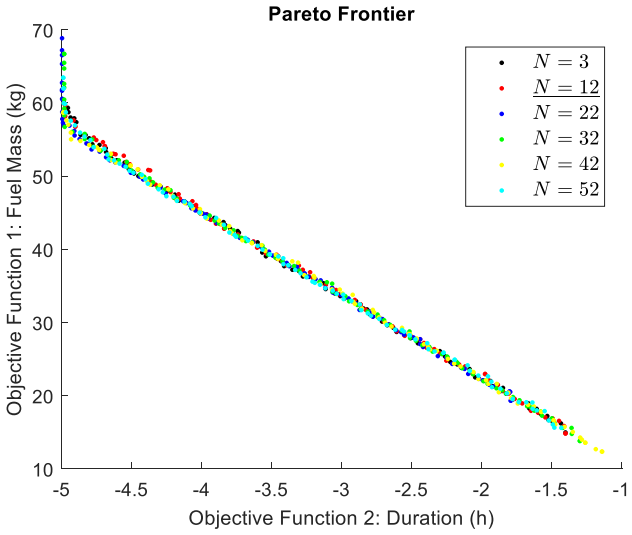

Figure 3-10 Pareto frontiers with different discretization numbers

Table 3-7 compares the optimization time, convergence generations and normalized spread of solutions. The convergence generation is recognized when the average change in the spread of Pareto optimal solutions is less than the pre-set tolerance. With the largest spread, the case with $N = 22$ achieves the best Pareto front spread among four tests. However, its optimization time is twice over time of the case with $N = 12$. The spread increases with the rising of discretization number, from $N = 3$ to $N = 22$. The spread of $N = 32$ case is even smaller than one of $N = 3$ case. On the contrary, the spread decreases when the discretization number increases from $N = 32$ to $N = 52$. This implies that the optimization performance will be improved with larger discretization number, but overlarge number leads to poorer performance might due to overmuch computation demand.

Table 3-7 Comparison of optimization indices from different discretization numbers

N	Optimization Time (s)	Generations	Spread
3	37	102	0.1284
12	115	103	0.1459
22	266	185	0.1695
32	393	167	0.1231
42	555	151	0.1229

52	744	136	0.1038

In sum, the smaller discretization number will not sacrifice the precision of Pareto front; while the larger number can achieve better distribution performance with the trade-off of longer computation time. Another worth mentioning factor is that the overlarge number may lead to even poorer optimization performance.

3.6.2 Requirements and Parameters

The sensitivity of optimization results to the variation of performance requirements and system parameters is illustrated in detail in the following text. First, the Pareto frontiers of study cases with different d_{tkof} (230 m, 180 m, 130 m) and R_c (2.8 m/s, 3.4 m/s, 4.0 m/s) are compared in Figure 3-11. It shows that the variation of take-off distance and RoC will not influence the outcome of Pareto fronts. This is because that those two requirements mainly affect the take-off and climbing phase, which have little impact on two costs (fuel usage and flight duration).

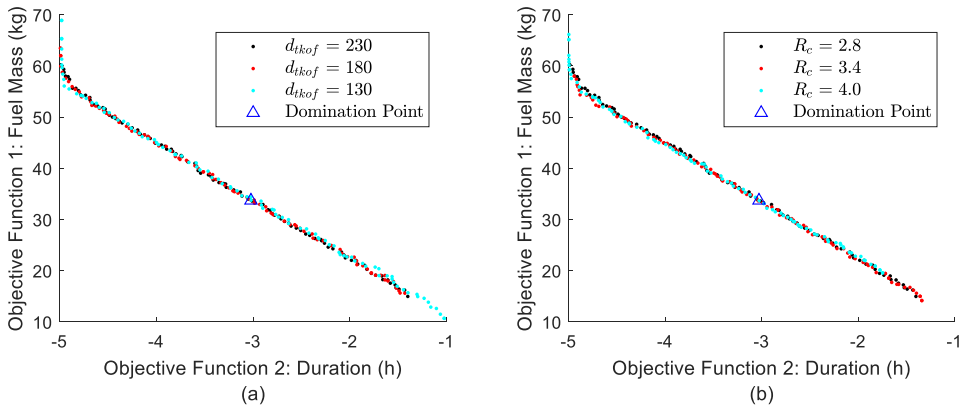

Figure 3-11 Pareto frontiers with different take-off distance (a) and rate of climb (b)

The above-mentioned phenomenon is also validated in Table 3-8, which lists the details of the preferred solution from different requirements and parameters. Note that the figure with underline means it is the result of the benchmark case used in Section 3.5. The minimum fuel mass does not change much for the same flight duration, even though the shorter take-off roll and higher RoC are requested. The most signification

effect of the variation of d_{tkof} and R_c is the combined maximum power, which becomes larger to achieve better performance. Another common consequence is that more powerful electric motor is sized instead of the combustion engine, because of the higher power-weight ratio of motors. The global weight is also increased to cover bigger propulsion component and additional battery weight. The fuel saving for 300 km cruising compared with the prototype aircraft falls slightly, since more fuel is consumed at the take-off and climbing segment.

Table 3-8 Comparison of optimized variables from different requirements and parameters

	$P_{ICE,max}$ (kW)	$P_{EM,max}$ (kW)	$P_{total,max}$ (kW)	m_f (kg)	m_b (kg)	m_g (kg)	Fuel Save (%)
d_{tkof} (m)							
230	39	33	72	33	114	635	17.3
180	39	34	73	33	118	641	17.3
130	40	46	86	34	115	642	16.7
R_c (m/s)							
2.8	39	33	72	33	114	635	17.3
3.4	39	41	80	33	122	647	16.3
4.0	39	48	87	34	115	642	15.5
t_{emerg} (min)							
15	39	33	72	33	114	635	17.3
30	39	33	72	36	122	647	10.8
45	43	36	79	43	180	713	0
ε_b (W*h/kg)							
180	39	33	72	33	114	635	17.3
260	41	33	74	31	123	642	23.8
340	42	35	77	28	158	675	33.3

Different from above-analysed variables, the variation of emergency time and battery energy density does affect Pareto fronts and the corresponding preferred points significantly (see Figure 3-12). The fuel mass is increased due to the rising of emergency time (electric-only flying), while the opposite trend occurs with the increase of battery energy density.

More details are provided in Table 3-8. The battery weight grows and the fuel-saving decreases, if more time of continuously electric-only flying is demanded. Furthermore, when the requested time rises to 45 min, the hybrid powered aircraft performs equally to the prototype one in terms of fuel economy. On the other hand, if the best commercially off-the-shelf battery (260 W*h/kg) is implemented in this research, 6% more fuel can be saved compared with the benchmark test case. The fuel saving can be even up to 33.3% if the energy density could realize 340 W*h/kg. Regarding the optimal weight and propulsion power, the global take-off mass and the total maximum power is sized higher for larger t_{emerg} and ε_b.

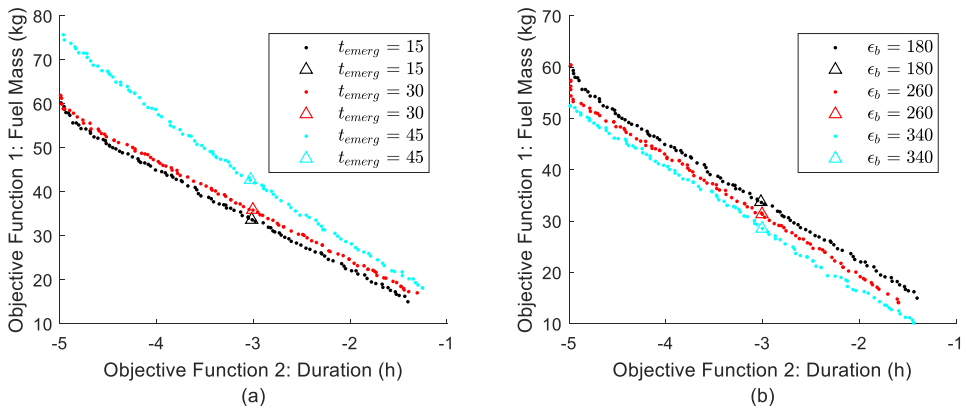

Figure 3-12 Pareto frontiers with different batter energy density (a) and emergency time (b)

In sum, the Pareto fronts and the corresponding preferred points are more sensitive to the variation of emergency time and battery energy density, than take-off distance and RoC. Put differently, the retrofitted (hybrid) aircraft can be sized to achieve better take-off and climbing performance, at the same time reserving the fuel saving advantage. Another conclusion from sensitivity analysis is that the prototype aircraft is not suitable to be retrofitted for over 45 min continuously electric-only flying. Following common sense, the improvement of battery technology (energy density) makes the hybrid propulsion system even more competent.

3.7 Components Selection

The off-the-shelf or custom-made devices for each component (see Figure 3-4) are illustrated in this section.

2EK C72AE from Sensenich Technologies, Inc. is selected as the initial propeller. 2EK C72AE is a two-blade propeller, equipped with Sensenich's new pitch cartridge system. The system enables the user to change and set the pitch on the ground easily. The propeller is manufactured using an internal pressure, closed mould system to produce a hollow, one-piece blade. This process yields very repeatable blades with maximum strength, durability, and low weight. 2EK C72AE can give around 75 kW at 2750 rpm. It is suitable for 162-209 km/h airspeed flight.

As concluded from Section 0, the rotary engine normally has a higher power-to-weight ratio than the piston one. The rotary engine has other advantages worth mentioning: 1) less output vibration and smooth operation because of longer process time; 2) compact size and lightweight, which becomes more attractive in aerospace application; 3) simple structure and fewer components due to unique intake and exhaust mechanism; 4) less vibration and low noise due to the absence of piston. All these benefits gain reliability and durability of rotary engines.

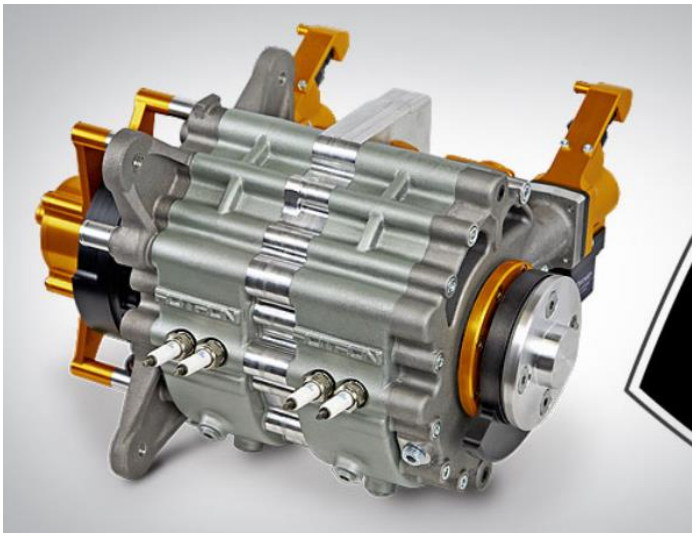

Figure 3-13 RT600 LCR rotary engine

The RT600 LCR [155] given in Figure 3-13, built by Rotron Power Ltd., is one of the high-performance rotary engines. This compact, two-rotor engine utilises the most advanced rotary technology and premium materials to produce industry-leading

performance in a lightweight, reliable and efficient package. RT600 LCR can achieve low levels of torsional vibration and zero radial vibration at mid-to-high speed range. It is integrated with an altitude compensation control, thereby being a good choice for aircraft application.

RT600 LCR can achieve the maximum torque around 6500 rpm with the liquid cooling technology from the company. Different from the conventional general aviation piston engine, the rotary engine tends to run at higher speed, like between 3000-8000 rpm (see Figure 3-14). Also, its best efficiency region is between 4500-5500 rpm and 40-50 N*m. Though the area with 7000-8000 rpm and 50-55 torque also has good efficiency, this working region is not recommended since continuously operating at high speed/torque condition easily causes the damage and over-heating for rotary engines. Considering the output ability and durability, the maximum speed of RT600 LCR is set as 6500 rpm for our HEPS. As a result, the normal working range of RT600 LCR is limited between 2000-6500 rpm, while 4500-5500 rpm is its ideal operating range. To apply the rotary engine to general aviation aircraft and the propeller 2EK C72AE, a reduction gear is needed and its ratio is set as 2.37. The reduction gear is normally attached to the output of the engine so called as the reduction drive.

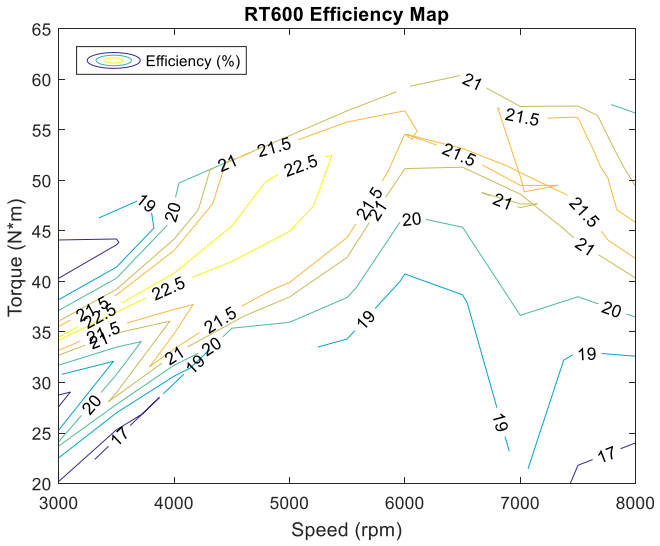

Figure 3-14 RT600 LCR efficiency map

Concerning the electric motor, the PMSM has the same advantages as the BLDC motor. The primary profit is the high power-weight and power-size density, which leads to light and compact motors. Secondly, they are inherently more energy efficient than induction motors since the rotor's magnetic field is not electrically produced. This can

significantly benefit the reduction of battery weight. In addition, the PMSM is superior to the combustion engine in many aspects. It can deliver high continuous output torque over their entire speed range. Better dynamic performance is also guaranteed under high load.

The EMRAX2x8 series of Company EMRAX d.o.o. [156] is widely applied in the automotive, marine and aerospace industries. The EMRAX motor ranks as one of the best high power-density motors in the global market. Its power density can be up to 4-5 kW/kg. The mechanical and no-load electrical losses of EMRAX motors are very small. This is important to our hybrid propulsion system since the electric motor has a high chance to operate on the low load condition. Moreover, the optimum operating range of EMRAX motors fits the speed range of the Sensenich propeller. This allows a gearless drive from the motor output, thereby reducing the power losses and avoiding the extra weight. Figure 3-15 gives the efficiency map of EMRAX228. The optimum speed range is between 2000-2500 rpm.

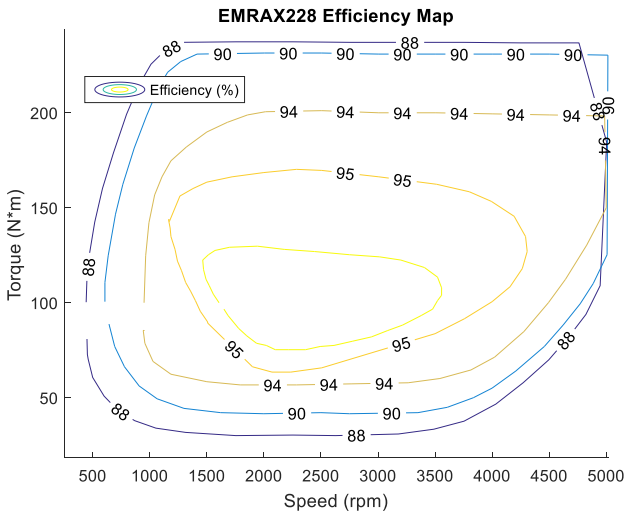

Figure 3-15 EMRAX228 efficiency map

Different EMRAX motors have similar efficiency map, but the output capability varies with different types. The continuous maximum power of EMRAX208, EMRAX228 and EMRAX268 are shown in Figure 3-16. The required power in the graph indicates that the sized hybrid propulsion system requests the electric motor to produce 33 kW around 3000 rpm. It is apparent that EMRAX228 is the most appropriate selection, while the power of EMRAX208 is insufficient and EMRAX268 is overly powerful.

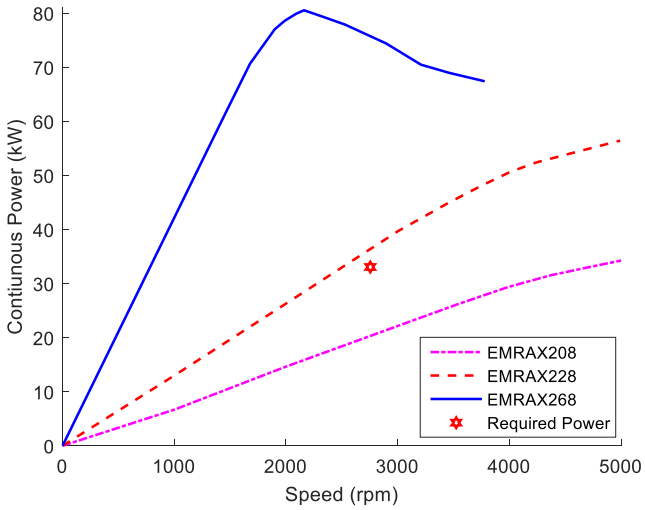

Figure 3-16 Continuous power output of EMRAX2x8 series motors

The EMRAX228 motor/generator is the medium-power one in the EMRAX2x8 series. Its size is only ⌀228 x 86 mm, as shown in Figure 3-17. It can work as a Permanent Magnet Synchronous Generator (PMSG) with the same technical data. Note that the motor controller of EMRAX228 is custom-made. Furthermore, the efficiency data of EMRAX228, as given by Figure 3-15, are acquired using this custom-made motor controller.

Figure 3-17 EMRAX228 motor

Meanwhile, a Lithium-ion Polymer (LiPo) battery pack are custom-made according to the voltage and current requirements of EMRAX228. The specific load-speed-rating of EMRAX228 is roughly 10 rpm/V, and the maximum speed it reaches is under 3000

rpm. Therefore, the 296 V nominal voltage battery could meet the requirements. Then, the battery capacity (Ah) can be estimated using the battery voltage and demanded electrical energy that is given by the optimal results of the propulsion system sizing.

Table 3-9 Components Overview

Components	Parameters	Values
RT600 LCR	Weight	21.2 kg
	Continuous maximum power	42 kW @ 7500rpm
	Available maximum power	40 kW @ 6500rpm
EMRAX228	Weight	12 kg
	Peak power	100 kW @ 5500rpm
	Continuous maximum power	56 kW @ 5000rpm
	Available maximum power	36 kW @ 3000rpm
Battery	Weight	106 kg
	Nominal voltage	296 V
	Capacity	70 Ah
Reduction drive	Weight	5 kg
	Gear ratio	2.37

An overview of all products is given in Table 3-9, while specific parameters are presented in the Chapter 4 Modelling. The rotation speed following a power value via @ indicates that this is the power reached at the stated speed. Note that both RT600 LCR and EMRAX228 cannot operate in its maximum-power condition, due to the constraint of the propeller speed and the gear ratio. The available power of RT600 LCR and EMRAX228 are 40 kW and 36 kW, reached around 6500 rpm and 3000 rpm, respectively.

Table 3-10 lists and compares the power and weight data of selected components and the corresponding optimized variables. The adjusted HEPS has higher combined power and dry weight. The selected motor costs three kilograms more than the optimized one, since a more powerful motor is selected. On the other hand, the weight of selected devices is not always the same as the optimized variable even though the power is equal. Those minor differences are usually acceptable for conceptual system

design. The selected engine and motor controller are heavier than the optimal ones since the best models are not always available among the off-the-shelf products. The battery weight is however reduced since the higher energy density cell is available from the manufacturer. If the load and the fuel weight are remained unchanged, the final MTOW of hybrid aircraft will be 633 kg. The adjusted global weight is 1 kg higher than the optimized one.

Table 3-10 Power and Weight Adjusting for Hybrid Aircraft

		Optimal	Adjusted
Available	Engine	40 kW	40 kW
Maximum Power	Motor	31 kW	36 kW
	Total	71 kW	76 kW
Weight	Engine	17 kg	21 kg
	Fuel	33 kg	33 kg
	Motor/Generator	8 kg	12 kg
	Controller	7 kg	8 kg
	Battery	114 kg	106 kg
	Load weight	223 kg	223 kg
	Fuel weight	33 kg	33 kg
	Additional Gear weight	5 kg	5 kg
	MTOW	632 kg	633 kg

3.8 Conclusion

A parallel hybrid electric propulsion system was designed for the prototype aircraft in this chapter. The chapter first presented the aerodynamics and requirements of the prototype aircraft before implementing the system sizing. The propulsion system sizing was established as a multi-objective optimization problem, in which the fuel usage was minimized and the flight duration was maximized. The requirements of the prototype aircraft were formulated as constraints.

The sized hybrid propulsion system can ensure that no substantial performance is compromised when saving the fuel burn. Using the multi-objective optimization, more characteristics of the hybrid system can be evaluated in one optimization run. A new non-dominated sorting algorithm was developed to improve the computational efficiency of the multi-objective optimization. This method can reduce lots of unnecessary comparisons and achieve $O(MN)$ of the best time complexity of the comparison. The potential of the hybrid electric technology is reflected via the Pareto fronts and the corresponding preferred points.

The Pareto frontier can give the best balance between fuel consumption minimization and duration maximization. Every possibility was evaluated and a series of optimal solutions is achieved, considering two contradictory cost functions. It is clear from the Pareto solutions that how the variables change with the objectives and which variables affect the costs mostly. The interesting conclusion is that the DoH has little impact on fuel usage and flight duration, while the hybrid of energy is the most significant factor affecting the fuel economy. One preferred solution (3-h duration) at Pareto frontier was selected to form the optimized hybrid electric system. It achieves around 17% fuel saving and better cruising and climbing performance, when using the battery with the energy density of 180 Wh/kg. Furthermore, the hybrid propulsion system has higher power-weight ratio than the conventional combustion powertrain, due to the introduction of the electric power system.

The result section also presented the sensitivity analysis of Pareto front and the preferred solution to the variation of discretization number, battery energy density, emergency time, take-off distance, and RoC. One of advantages of NSGA in this study is that the smaller discretization number not only reduces the computation considerably, but also has no sacrifice of the precision of the Pareto front. Another worth mentioning factor is that the overlarge number may lead to even poorer optimization performance. On the other hand, the hybrid propulsion system can be sized to achieve better take-off and climbing performance, also keeping the same amount of fuel saving. HEPS will lose its advantage on fuel saving if 45-minute continuously electric-only flying is required for the hybrid aircraft, but the advance of battery technology (energy density) can help HEPS to get rid of this limitation.

The off-the-shelf components were selected and compared with the optimized ones in the last section. The rotary engine RT600 LCR and PMSM EMRAX228 were chosen according to the optimized maximum power from the sizing results. The battery voltage

was determined following the requirement of EMRAX228. The reduced weight of battery compensates the increased weight of other devices (engine, motor and its controller). The adjusted MTOW of hybrid aircraft is 1 kg higher than the original optimized one.

4 **Modelling**

This chapter will present the modelling of the engine, motor/generator, battery and DC/DC converter in detail.

The dynamics of the engine is governed by the mean value model, which considers the engine unit control. The static fuel performance is given by the fuel map. The engine model is validated by comparing the simulation data with the experimental data.

D-q model is introduced to simplify the integration of torque loss and the control of permanent magnetic motor/generator. The steady-state torque loss of motor/generator is estimated using the efficiency map supplied by the manufacturer. The design of vector control follows the estimation of torque loss, to convert the original AC model into a DC model.

The Shepherd model is applied to estimate the open circuit voltage of the lithium battery. The parameters of the model are directly identified using the battery discharge curve. The identified model is also validated by the comparison with the experiment results.

The average model of bidirectional DC/DC converter is provided in the last section of this chapter.

4.1 Engine

4.1.1 Model

For this study, the MVM is too complicated while a model based on first-order or second-order transfer function cannot reveal the relationship between the throttle position and output capability. Therefore, a simplified mean value engine model is proposed in this study. It does not include manifold dynamics and flow rate dynamics, but can reserve the dynamics between the throttle demand and the engine speed, which are both needed to estimate the engine torque request, $T_{ice,ref}$. The engine torque request is the sum of Engine Control Unit (ECU) output and torque make-up from the idle speed controller:

$$T_{ice,ref} = f(\delta_{ice}, \omega_{ice}, e_{air}) + T_{ice,idle}, \quad \textbf{(4-1)}$$

where $f(\delta_{ice}, \omega_{ice}, e_{air})$ is an experimental-data based function which realizes the utility of the ECU. $T_{ice,idle}$ is the idle torque from idle speed controller. δ_{ice} is a throttle command and generated by the engine speed controller. e_{air}, the altitude-related coefficient, is also introduced to compensate the engine loss due to the variation of air density. It is worth noting that $f(\delta_{ice}, \omega_{ice}, e_{air})$ also includes other engine losses. Therefore, there is no need to estimate torque losses of the engine.

The relationship between the engine torque request and the induced torque is given by:

$$\dot{T}_{ice}(t) = -\frac{1}{\tau_{ice}} T_{ice}(t) + \frac{1}{\tau_{ice}} T_{ice,ref}\left(t - \delta_{ice,prc}\right), \quad \textbf{(4-2)}$$

where T_{ice} is the induced engine torque and τ_{ice} is the engine time constant due to fuel/air injection. $\delta_{ice,prc} = \vartheta_{rotary}/\omega_{ice}$ represents the time for one engine process, namely the combustion stroke to exhaust stroke. Since the working principle of the rotary engine is different from the piston engine, this process time needs to be changed according to the characteristics of the rotary engine.

The rotational dynamics of the engine is governed by:

$$\frac{d\omega_{ice}}{dt} = (T_{ice} - T_{ice,load})/J_{ice}, \quad \textbf{(4-3)}$$

where J_{ice} is the inertia of engine and $T_{ice,load}$ is torque of the load.

When the engine is decoupled from the motor/generator, $T_{ice,load}$ is equal to zero. On the contrary, if the rotational dynamics of engine and motor/generator are coupled, the load torque $T_{ice,load}$ is dependent on devices connected to the engine output shaft, such as motor/generator and propeller. The calculation of load torque will be given in Section 4.1.3. Lastly, the restriction of engine speed is imposed on the output of rotational dynamics module.

The parameters needed for the engine modelling are given in Table 4-1.

Table 4-1 Parameters of Engine

Parameters	Symbols	RT600
Maximum speed (rpm)	-	8000
Idle speed (rpm)	-	2000
Time constant (s)	τ_{ice}	0.002
Angle for one process (degree)	ϑ_{rotary}	90
Moment of inertia (kg*m^2)	J_{ice}	0.07638

The complete engine model and its speed control loop are illustrated in Figure 4-1. The output of speed controller is the throttle command, while the input of speed controller is the speed reference $\omega_{ice,ref}$ and instantaneous engine speed. The speed controller of the engine is modelled as a PI controller, the same as the idle-speed controller.

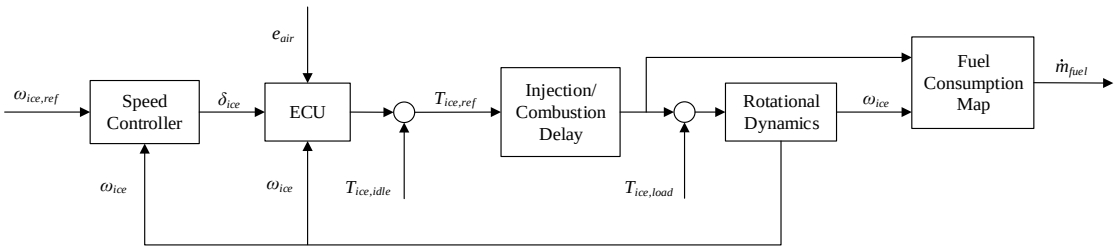

Figure 4-1 Speed control loop of engine

The fuel estimation module is attached at the end of the whole model, using the static fuel map. The static fuel map is a function of the torque and engine speed (see Figure 4-2). The static map has been proven to give a satisfactory prediction of fuel consumption under different operating conditions [26]. The Specific Fuel Consumption (SFC) values are used here to emphasize the trend of fuel consumption per power. As shown in Figure 4-2, the engine reaches the best fuel economy per power at the high torque among the range of 4500-5500 rpm.

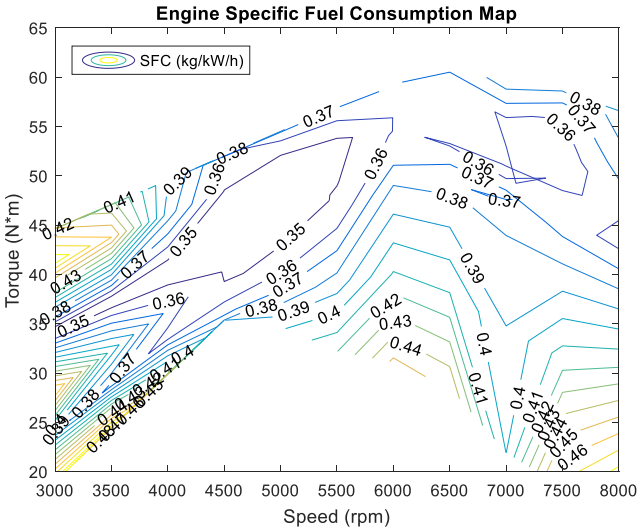

Figure 4-2 Specific fuel consumption map of engine

4.1.2 Validation

The steady-state characteristics of the engine model is validated by comparing the simulation data with experimental measurements. Figure 4-3 shows the torque and power percentage errors under different steady states. Among the speed range considered, the error is defined as:

$$err = \frac{(D_s - D_e)}{D_e}, \qquad \textbf{(4-4)}$$

where D_s means simulation data while D_e represents experimental one. The calculated error percent is always less than 2.5%. Note that the continuous-operation speed (recommended speed) of RT600 is between 3000-6500 rpm.

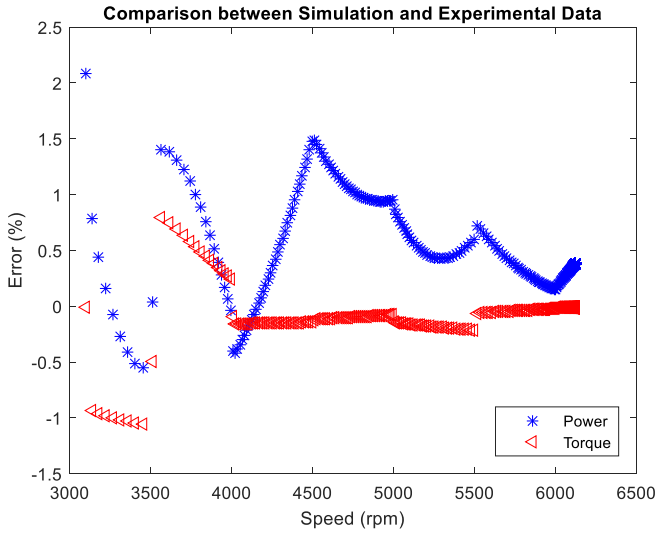

Figure 4-3 Comparison between simulation and experimental data of engine

4.1.3 Reduction Drive

A sprag clutch is integrated into the reduction drive of the engine. Its working state depends on the speed of input and output shaft of the clutch. The speed of input shaft of the clutch is equal to the engine speed ω_{ice}, while the speed of output shaft is the same as the motor/generator speed ω_{mg}.

When the engine and motor/generator is coupled, the following constraints have to be satisfied:

$$\omega_{ice} = G\omega_{mg}, \tag{4-5}$$

$$GT_{ice,load} = T_{mg,drive}, \tag{4-6}$$

where $T_{mg,drive}$ indicates the torque drives the following devices (motor/generator and propeller etc.). At this state, the speed of input shaft has to be no less than one of output shaft, namely $\omega_{rd,in} \geq \omega_{rd,out}$.

If the speed of output shaft is larger than one of input shaft, i.e. $\omega_{rd,in} < \omega_{rd,out}$, the two shafts would be decoupled. The output shaft speed will be free from the input shaft speed. Furthermore, $T_{ice,load}$ and $T_{mg,drive}$will become zero after decoupling.

4.2 Motor/Generator

This thesis introduces the d-q model to approximate the dynamics of the permanent magnet motor/generator. Concerning the steady-state behaviour, Evangelou and Shukla studied a creative method to estimate a general-purpose friction torque, using the efficiency map [69]. In the study by Evangelou and Shukla, it is proved that the friction torque loss of the motor they used can be approximated by the function which is only dependent on rotor speed. In our study, without sacrifice of complexity, the torque loss is given as the function of both electromagnetic torque and rotor speed. The calculated torque loss is then integrated into the d-q model.

Different from the engine, the control of PMSM/PMSG is separated into three parts: vector control, torque control and speed control. The vector control is used to convert PMSM/PMSG into equivalent separately excited Direct Current (DC) machines, which have highly desirable control characteristics. The torque and speed control are implemented on the basis of the vector control.

Lastly, the average model of the voltage source converter (inverter/rectifier) is described by the input-output electrical relationships of the average Pulse-Width-Modulated (PWM) converter in the d-q frame [157,158].

4.2.1 Motor

Under some assumptions [68], the dynamic behaviour of the three-phase PMSM can be described by the following differential equations, in the rotor d-q reference frame [67]:

$$\frac{di_d}{dt} = (v_d - R_s i_d + \omega_s L_q i_q)/\, L_d, \qquad \textbf{(4-7)}$$

$$\frac{di_q}{dt} = (v_q - R_s i_q - \omega_s L_d i_d - \omega_s \lambda_m)/L_q, \quad \textbf{(4-8)}$$

where v_d and v_q are the d- and q- axis stator voltages, whereas i_d and i_q are the d- and q- axis stator currents. L_d and L_q are the d- and q- axis stator inductances, respectively. λ_d and λ_q are the d- and q- axis stator flux linkages, while λ_m is the magnet mutual flux linkage. R_s represents the stator resistance and ω_s is the inverter frequency.

The equation of the motor rotational dynamics is:

$$\frac{d\omega_{mot}}{dt} = (T_{mg,drive} + T_{mot} - T_{mot,loss} - T_{prop})/J_{mot}, \quad \textbf{(4-9)}$$

in which ω_{mot} is the rotor speed, J_{mot} is the moment of inertia, and T_{prop} is the load torque caused by the rotating of the propeller. The electromagnetic torque (T_{mot}) produced by the motor is given by [67]:

$$T_{mot} = 3p\left[\left(\lambda_m i_q + \left(L_d - L_q\right) i_d i_q\right)\right]/2 = \frac{3}{2} p \lambda_m i_q, \quad \textbf{(4-10)}$$

where p is the number of pole pairs and the inverter frequency is related to the rotor speed with $\omega_s = p\omega_{mot}$. It should be noted that the right hand side of Eq. (4-10) is obtained by forcing i_d to zero. Therefore, i_q can be represented by $\frac{2T_{mot}}{3p\lambda_m}$.

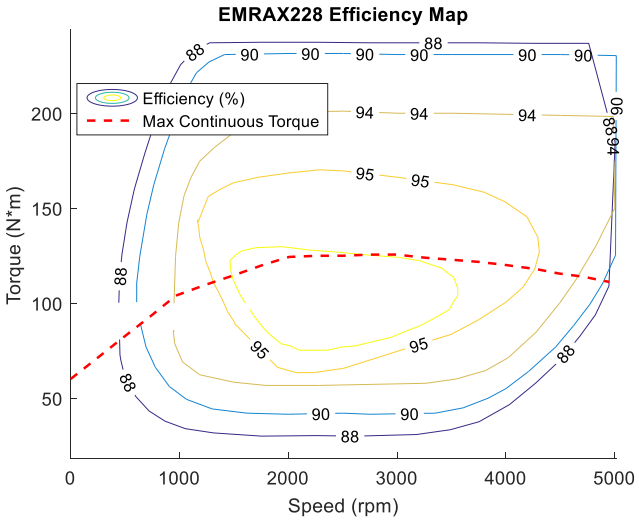

Figure 4-4 Efficiency map of PMSM

On the other hand, the motor torque loss $T_{mot,loss}$ including friction loss and damping is approximated by the efficiency map supplied by the manufacturer (see Figure 4-4). Note that the y-axis of Figure 4-4 represents the output torque of motor or the input torque of the generator. In other word, if the electric device works as the motor, the torque given in the efficiency map is equal to the load torque T_{prop}; otherwise, this torque is equal to the driving torque $T_{mg,drive}$.

The efficiency of the motor η is defined as:

$$\eta = \frac{P_{out}}{P_{in}} = \frac{T_{prop}\omega_{mot}}{P_{in}}, \tag{4-11}$$

in which P_{in} represents the total electromagnetic power and is expressed by [69]:

$$P_{in} = 3(v_d i_d + v_q i_q)/2. \tag{4-12}$$

According to mechanical characteristics under equilibrium conditions, the torque loss acting on the rotor is:

$$T_{mot,loss} = T_{mot} - T_{prop}, \tag{4-13}$$

when there is no driving torque from the reduction drive, $T_{mg,drive} = 0$. If T_{mot} in Eq. (4-13) is substituted using equations (4-10)-(4-12), a quadratic equation of $T_{mot,loss}$ can be addressed:

$$kT_{mot,loss}^2 + \left(\omega_{mot} + 2kT_{prop}\right)T_{mot,loss} + kT_{prop}^2 + \left(1 - \frac{1}{\eta}\right)\omega_{mot}T_{prop} = 0, \tag{4-14}$$

where $k = \frac{2R}{3\lambda_m^2 p^2}$. Different from the study in [69], the torque loss is not approximated by the function that is only dependent on rotor speed, while it is given as the function of electromagnetic torque and rotor speed. The details of result are presented in the next Section 4.2.2.

4.2.2 Generator

The electrical dynamics of the PMSG is the same as one of the PMSM. The reversal of the flow of current and voltage is reflected by changing the signs of the corresponding variables. That is:

$$\frac{di_d}{dt} = (-v_d - R_s i_d + \omega_s L_q i_q)/\, L_d, \tag{4-15}$$

$$\frac{di_q}{dt} = (-v_q - R_s i_q - \omega_s L_d i_d + \omega_s \lambda_m)/L_q. \tag{4-16}$$

The rotational dynamics of the generator is governed by the following equation:

$$\frac{d\omega_{gen}}{dt} = [T_{mg,drive} + T_{gen} - T_{gen,loss} - T_{prop}]/J_{gen}, \tag{4-17}$$

in which ω_{gen} is the generator rotor speed. Note that the electromagnetic torque T_{gen} is negative when the device functions as the generator. $T_{mg,drive}$ and T_{prop} have the same meaning as given in the above section. J_{gen} is the inertia of generator. The electromagnetic torque T_{gen} and power P_{out} of the generator are:

$$T_{gen} = \frac{3}{2} p \lambda_m i_q, \tag{4-18}$$

$$P_{out} = 3(v_d i_d + v_q i_q)/2, \tag{4-19}$$

if the vector control is applied and i_d is forced to zero.

It is noted that, when acting as the generator, the PMSG must be coupled with the engine via the sprag clutch. To estimate the torque loss, the load torque T_{prop} should be set to zero at the steady state, instead of the driving torque. Therefore, the generator torque loss $T_{gen,loss}$ is related to driving torque $T_{mg,drive}$ with:

$$T_{gen,loss} = T_{mg,drive} + T_{gen}, \tag{4-20}$$

when all driving torque is used to generate electricity. The efficiency of the generator is given by:

$$\eta = \frac{P_{out}}{P_{in}} = \frac{P_{out}}{T_{mg,drive}\omega_{gen}}. \quad \textbf{(4-21)}$$

Following the similar deduction as one for $T_{mot,loss}$, a quadratic equation of $T_{gen,loss}$ can be addressed. The results of the loss estimation of motor and generator are both shown in Figure 4-5. It is obvious that the torque loss grows quickly when the speed is above 4500 rpm or the torque is higher than 200 N*m for both motor and generator mode.

Furthermore, the torque loss of the motor increases with the growth of torque when the torque is under 50 N*m, while the variation of speed have no big influence on the torque loss. More importantly, the minimum loss of the motor is around 2000-2500 rpm and 80-120 N*m. These characteristics are the same for the generator.

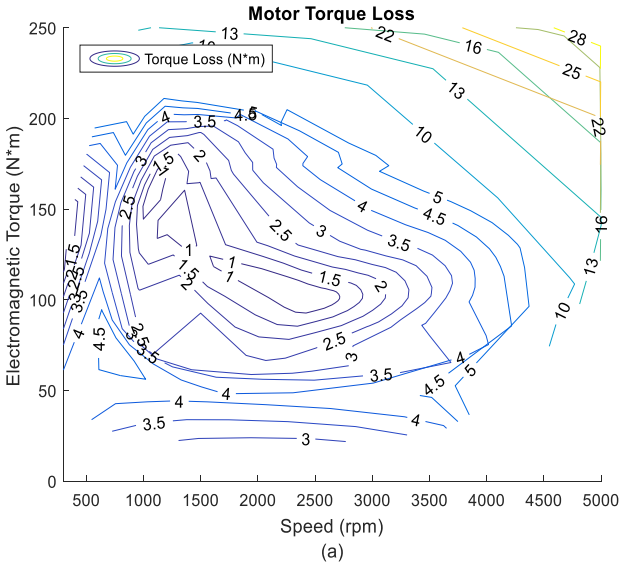

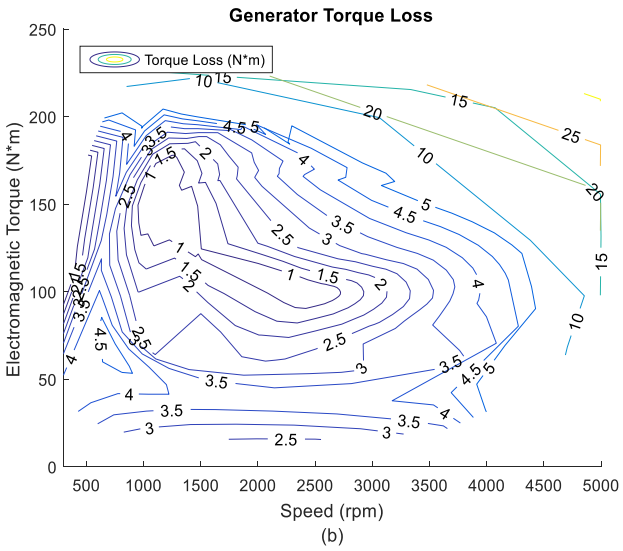

Figure 4-5 Torque loss of motor (a) and generator (b)

The parameters of PMSM/PMSG required for the modelling are shown in Table 4-2.

Table 4-2 Parameters of motor/generator

Parameters	Symbols	EMRAX228
Maximum speed (rpm)	-	5000
D-axis stator inductance (μH)	L_d	175
Q-axis stator inductance (μH)	L_q	180
Stator resistance (Ω)	R_s	0.018
Magnet mutual flux (Wb)	λ_m	0.0542
Moment of inertia (kg*m2)	J_{mot}/J_{gen}	0.0421
Number of pole pairs	p	10

4.2.3 Controllers

The control of PMSM/PMSG can be separated into three loops (see Figure 4-6): vector control, torque control and speed control. All control loops are realized using PI controls. To convert AC motors into equivalent DC motors which a re separately excited, the vector control is used to recreate the orthogonal flux by controlling i_q and i_d, respectively [68]. Then, the torque following is achieved by forcing i_d to zero and regulating i_q. Similarly, the required speed is obtained by controlling the torque. This

control structure can accept both speed and torque references. Meanwhile, the transition between speed and torque control modes is governed by the supervisory control.

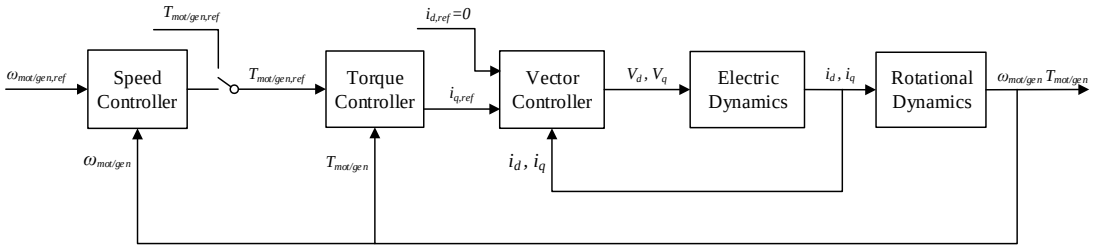

Figure 4-6 PMSM/PMSG control loops

4.2.4 Inverter/Rectifier

The average model of the inverter/rectifier is represented by the average PWM converter in the d-q frame [157]:

$$\begin{bmatrix} v_d \\ v_q \end{bmatrix} = \begin{bmatrix} d_d \\ d_q \end{bmatrix} V_{bus}, \tag{4-22}$$

$$I_{bus} = \frac{3}{2}\begin{bmatrix} i_d & i_q \end{bmatrix} \begin{bmatrix} d_d \\ d_q \end{bmatrix}, \tag{4-23}$$

in which d_d, d_q are continuous duty cycle functions in the d- and q- axis, respectively. Their values are be obtained from the actual values of V_{bus}, v_d and v_q (see Eq. (4-22)). V_{bus} is the voltage connected to the DC/DC converter bus. Then, the current I_{bus} drawn by the inverter/rectifier from the DC/DC converter can be derived using Eq. (4-23).

4.3 Battery

4.3.1 Model

The battery model applied in the thesis is the one proposed by Shepherd in 1965 [74] and improved by Tremblay in 2007-2009 [75,76]. This model follows the approach

proposed by Shepherd, which neglects the faster RC circuit dynamics and pays attention to the open circuit voltage and current of the battery. Both the battery open circuit voltage and internal resistance are primarily dependent on the battery SoC and electrolyte temperature. Here, we assume that the open circuit voltage is immune to the temperature and the internal resistance is a constant value [74]. As a result, the discharge characteristics of LiPo batteries are governed by:

$$V_b = E_0 - K \cdot \frac{Q}{Q - Q_{batt,c}} \cdot Q_{batt,c} - K \cdot \frac{Q}{Q - Q_{batt,c}} \cdot i^* + Ae^{-B \cdot Q_{batt,c}}; \quad \textbf{(4-24)}$$

where V_b is the battery open circuit voltage, E_0 is the battery constant voltage, i^* is the filtered current obtained by a low-pass filter, K is the polarization resistance (Ω), A is the exponential voltage coefficient (V), and B is the exponential capacity coefficient ($(Ah)^{-1}$). Q is the battery capacity and $Q_{batt,c} = \int I_{batt} dt$ is called actual battery charge, in which $Q_{batt,c}(0) = Q - Q_0$ and Q_0 is the battery energy at the initial state. The definition of battery SoC is established on the battery capacity and actual battery charge:

$$SoC = \frac{Q - Q_{batt,c}}{Q}. \quad \textbf{(4-25)}$$

The filtered current i^* is used to obtain a ripple-free battery current. It can also solve the algebraic loop issue caused by directly multiplying $(Q - Q_{batt,c})/Q$ by i in Eq. (4-24). Additionally, filtered current i^* can reproduce a slow dynamic behaviour of battery voltage for a step response, which is more compatible with the experimental results [76]. Also derived from the experimental experience, $Q_{batt,c}$ instead of i, is multiplied by $K \cdot (Q - Q_{batt,c})/Q$.

For the charge mode, the polarisation resistance K increases when actual battery charge $Q_{batt,c}$ decreases. This feature is expressed by the term $K \cdot Q/Q_{batt,c}$. As a result, the charge characteristics is given by:

$$V_b = E_0 - K \cdot \frac{Q}{Q - Q_{batt,c}} \cdot Q_{batt,c} - K \cdot \frac{Q}{Q_{batt,c}} \cdot i^* + Ae^{-B \cdot Q_{batt,c}}. \quad \textbf{(4-26)}$$

Since $Q_{batt,c} = \int_{Q-Q_0} I_{batt} dt$, the term $K \cdot Q/Q_{batt,c}$ will become the infinite when the battery is fully charged ($Q_{batt,c} = 0$). This not only leads to the computation problem, but also not conforms to the practice. The experimental results shows that the contribution of the polarisation resistance is shifted by about 10% of the battery capacity [75]. Therefore, the charge equation can be rewritten to:

$$V_b = E_0 - K \cdot \frac{Q}{Q - Q_{batt,c}} \cdot Q_{batt,c} - K \cdot \frac{Q}{Q_{batt,c} - 0.1Q} \cdot i^* + Ae^{-B \cdot Q_{batt,c}}. \quad \textbf{(4-27)}$$

Finally, the output voltage V_{batt} is obtained by:

$$V_{batt} = V_b - I_{batt} \cdot R_b, \quad \textbf{(4-28)}$$

in which I_{batt} is the output current and R_b represent the internal resistance.

4.3.2 Parameter Identification

One of advantages of the Shepherd model is that it is straightforward to identify the parameters for the dynamic model. One discharge curve and the value of internal resistance are sufficient for the parameter identification. Three points on the discharge curve are required to be identified. Those three points are: fully charged point (V_{full}, Q_{cut}), the end of the exponential zone (V_{exp}, Q_{exp}), and the end of the nominal zone (V_{norm}, Q_{nom}). The final results of the parameter identification contain the values of constant voltage (E_0), polarization resistance (K), exponential voltage coefficient (A), and exponential capacity coefficient (B).

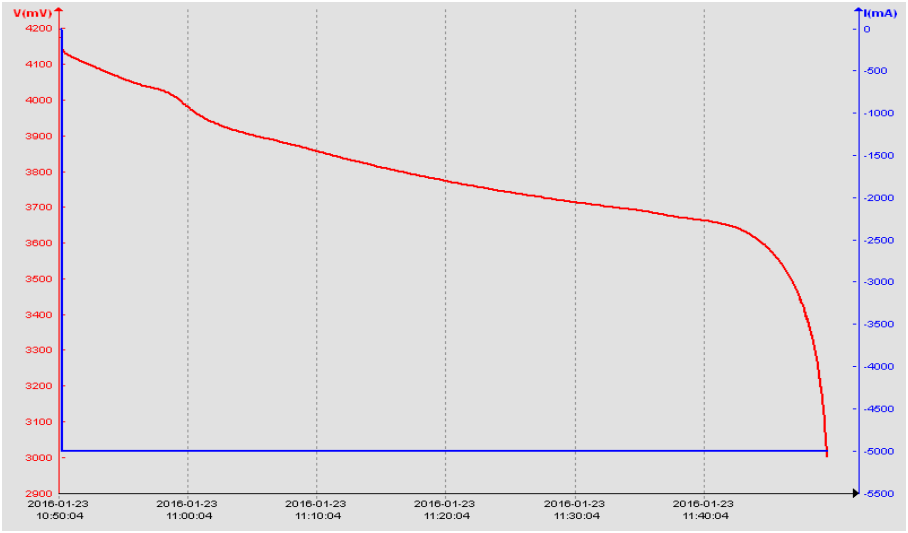

Figure 4-7 Experimental discharge curve of one cell

The one-cell discharge curve supplied by the manufacturer is shown in Figure 4-7. Note that the manufacturer curve is obtained at constant discharge current. Here, the battery is discharged with the 5.007 A. The related values of three key points are all given in Table 4-3.

Table 4-3 Parameters of battery

Parameters		Symbols	LiPo
Full zone	Full Voltage (V)	V_{full}	4.175
	Capacity (Ah)	Q	4.951
Exponential zone	Exponential Voltage (V)	V_{exp}	3.5500
	Exponential Capacity (Ah)	Q_{exp}	4.6410
Nominal zone	Nominal Voltage (V)	V_{nom}	3.5710
	Nominal Capacity (Ah)	Q_{nom}	4.6007
Discharge Current (A)		i	5.007
Internal Resistance (Ω)		R_b	0.296

In terms of the fully charged voltage, both the extracted discharge ($Q_{batt,c} = 0$) and the filtered current (i^*) are zero. The output voltage at the fully charged point becomes:

$$V_{full} = E_0 + A - i \cdot R_b. \quad \textbf{(4-29)}$$

Concerning the end of the exponential zone and nominal zone, the multiplication inverse of B is approximated to one third of Q_{exp}, since the energy of the exponential term ($e^{-BQ_{exp}}$) is almost zero (0.05) when the argument is larger than three [76]. The filtered current (i^*) is equal to i since the current is at the steady state:

$$V_{exp} = E_0 - K \cdot \frac{Q}{Q - Q_{exp}} \cdot (Q_{exp} + i) + Ae^{-BQ_{exp}} - i \cdot R_b, \quad \textbf{(4-30)}$$

$$V_{nom} = E_0 - K \cdot \frac{Q}{Q - Q_{nom}} \cdot (Q_{nom} + i) + Ae^{-BQ_{nom}} - i \cdot R_b, \quad \textbf{(4-31)}$$

The identified parameters of the LiPo battery are shown in Table 4-4.

Table 4-4 Identified Parameters of battery

Identified Parameters	Symbols	LiPo
Constant voltage (V)	E_0	4.1484
Polarization resistance (Ω)	K	0.0011
Exponential voltage coefficient (V)	A	0.4772
Exponential capacity coefficient ((Ah)$^{-1}$)	B	0.6464

Then, the steady-state characteristics of the battery model is verified by the comparison between the simulation data and experimental measurements. Figure 4-8 (a) compares the discharge curve derived from the Shepherd model with the discharge curve from experiments. Note that one shortage of the Shepherd model is that it cannot predict the battery voltage beyond the nominal zone (lower than 3.5 V). This deficiency can be accepted in practical applications since the battery usually is not permitted to operate at the low voltage (SoC) condition. Figure 4-8 (b) provides the error of the voltage between the engine model and experimental data, under different equilibrium states. It is clear that the model achieves a very good match, since all errors are lower than 1%.

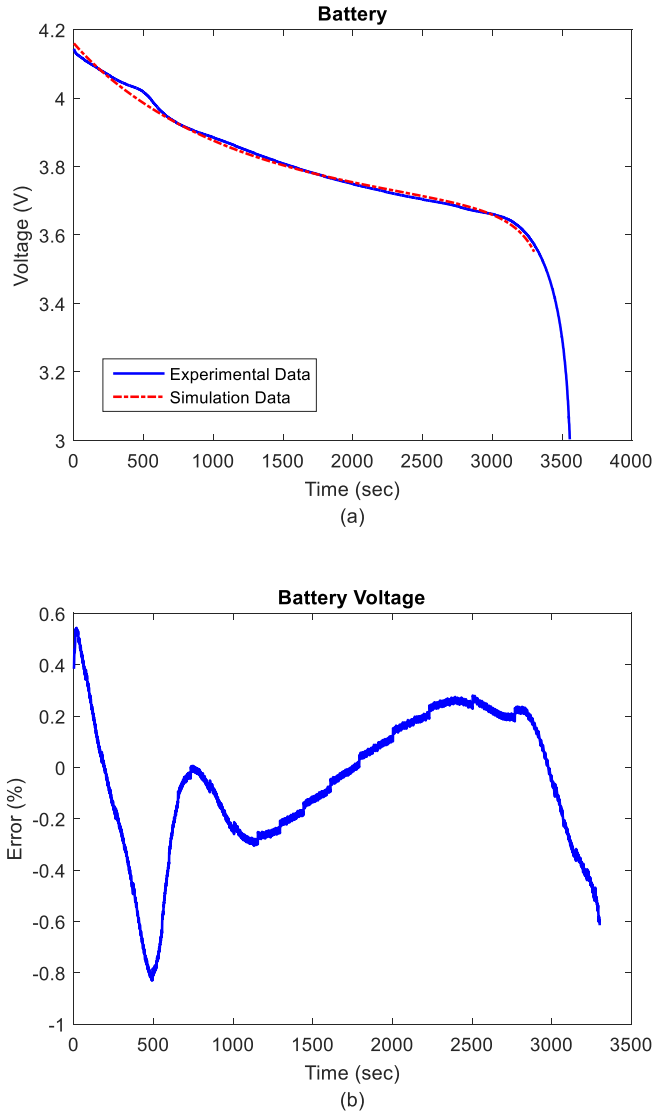

Figure 4-8 Comparison between simulation and experimental data of battery

4.4 DC/DC Converter

The bidirectional DC/DC converter is applied to stable the voltage and manage the battery charge. Another role of the DC/DC converter in our HEPS is to boost the voltage to a high value during take-off and climb.

According to the placement of energy storage source, the bidirectional DC/DC converter can be categorized into the buck and boost type. The buck type is to have energy storage placed on the high voltage side, while the boost type is to have it placed on the low voltage side [70]. Therefore, the DC/DC converter in our system is

the boost one, but it can work at both buck and boost mode. The transition between buck and boost modes is achieved by regulating the duty-cycle switching frequency.

As shown in Figure 4-9, Ref. [70] gives a simplified general circuit diagram of bidirectional DC/DC converter when the battery is on the low voltage side. Q_1 and Q_2 are two active switches that can change the duty cycle of the bidirectional DC/DC converter. C_1 indicates the bus capacitor bank at high voltage side. Since the low voltage side is the battery, a strong voltage source, the capacitor bank of this side is neglected. The equivalent inductance and its parasitic resistance are denoted by L_1 and R_L, respectively. Note that the inductance parasitic resistance should not be neglected for the high power application.

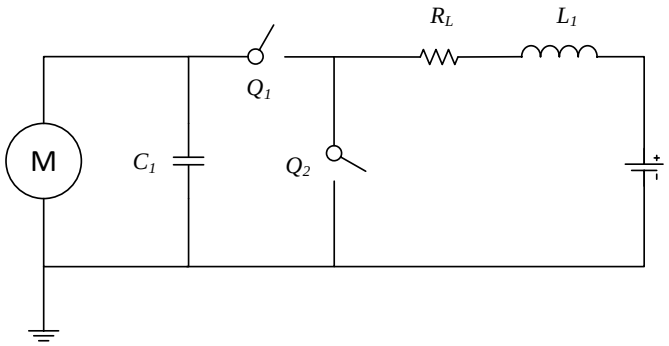

Figure 4-9 General circuit of bidirectional DC/DC converter

Then, the dynamics of the inductor current i_L and capacity voltage v_C are addressed by:

$$\frac{di_L}{dt} = \begin{cases} \dfrac{v_C - V_{batt} - R_L i_L}{L_1}, & Q_1 \text{ is on} \\ \dfrac{-V_{batt} - R_L i_L}{L_1}, & Q_2 \text{ is on} \end{cases} \tag{4-32}$$

$$\frac{dv_C}{dt} = \begin{cases} \dfrac{-I_{bus} - i_L}{C_1}, & Q_1 \text{ is on} \\ -\dfrac{I_{bus}}{C_1}, & Q_2 \text{ is on} \end{cases} \tag{4-33}$$

at two different subintervals of one switch cycle. The first equations of Eqs. (4-32) and (4-33) represent current and voltage variation in the first subinterval, respectively, when

the switch Q_1 is on and Q_2 is off. In the second subinterval, when Q_1 is off and Q_2 is on, the equivalent circuit is governed by the second equations of Eqs. (4-32) and (4-33).

The parameters needed for the converter modelling are listed in Table 4-5.

Table 4-5 Parameters of bidirectional DC/DC Converter

Parameters	Symbols	DC/DC Converter
Equivalent inductance (μH)	L_1	25
Bus capacitor bank (μF)	C_1	150
Inductance parasitic resistance (mΩ)	R_L	35

Assume that the inductor current ripple is small, then the state-space averaging model can be derived:

$$\frac{dI_L}{dt} = (\alpha V_C - V_{batt} - R_L I_L)/\, L_1, \tag{4-34}$$

$$\frac{dV_C}{dt} = (-I_{bus} - \alpha I_L)/C_1, \tag{4-35}$$

where α is the duty-cycle average value of the first subinterval. I_L and V_C are average values of their instantaneous corresponding ones. Lastly, the output of the DC/DC converter bus is:

$$V_{bus} = V_C,\ I_{batt} = -I_L. \tag{4-36}$$

The bus voltage can be regulated by controlling the switching duty-cycle. A PI controller is employed in this thesis.

4.5 Conclusion

This section presented the modelling of the ICE, PMSM, LiPo battery and bidirectional DC/DC converter.

The MVM of the engine was validated by comparing the simulation results with experimental data. The model simplifies the manifold dynamics and flow rate dynamics. The model represents the inherent dynamics between the throttle command and the output torque. The model has the low computational complexity since further calculation of the engine torque loss is not needed.

The d-q model was applied to simulate the electromagnetic dynamics of the motor/generator. Concerning the model behaviour at the steady state, the torque loss was estimated using the efficiency map supplied by the manufacturer. The d-q model and vector control simplify the speed and torque control of motor/generator, by converting the original AC model into a DC one.

The Shepherd model and its improved version were employed to estimate the battery voltage. The parameters of the Shepherd model can be easily extracted from the discharge curve of the battery. Not only a precise model is achieved, but also large amounts of identification experiments are avoided.

Lastly, the averaging model of bidirectional DC/DC converter was derived using a general circuit diagram.

5 Non-Causal Energy Management

In the non-causal control study, both dynamic programming and convex optimization are researched and compared, while only the convex optimization is presented in detail.

This chapter starts by first covering the primary energy management formulation, in which the minimization of the total fuel usage is selected as the objective. The convexity of the original problem is clarified via investigating the approximation to the experimental data.

The most challenging work of applying the convex programming is to convert the original problem into a convexified one. Two techniques—change of variables and equality relaxation are implemented to convexify the concave constraints. The discretization is implemented subsequently on the new convexified problem. The proof of equality between the original problem and convexified problem is also given in this study.

Two different hypothetical flight test scenarios are designed in this thesis to validate the convex optimization. The first test includes the complete flight mission, while the second test case extends the cruising phase of the first one.

5.1 Original Problem Formulation

Initially, the formulation of the original problem, including constraints and the objective, will be presented. In this study, the objective of the energy optimization is to minimize the fuel consumption of engine during the complete flight mission.

5.1.1 Powertrain Modelling

As explained in Section 2.2, the (quasi-) static models are employed in the energy optimization study. The HEPS combines the energy from the fuel and electric storage to power the vehicle, regardless of the hybrid powertrain configuration. Considering the instantaneous power flow in the powertrain, the power output of fuel combustion P_{fuel} in addition to electric storage, $P_{eletric}$, always equals to the sum of system power requirement, P_{req}, and power loss, P_{loss} (see Eq. (5-1)).

$$P_{fuel} + P_{eletric} = P_{req} + P_{loss}. \quad \textbf{(5-1)}$$

P_{fuel} is sometimes replaced by the engine power P_{ICE}, since the fuel map of the engine is normally represented as the function of power, P_{ICE}. If the minor mechanical power loss is omitted, the power loss, P_{loss}, needs contain only the electric power loss, then Eq. (5-1) can be re-written as:

$$P_{ICE} + P_{eletric} = P_{req} + P_{eletric,loss}. \quad \textbf{(5-2)}$$

If the battery is selected as the electrical energy source, the battery discharging/charging power will be the electric power displayed in Eq. (5-2), while the electric power loss will be the power loss from the electric motor (i.e the motor/generator in this thesis):

$$P_{ICE} + P_{batt} = P_{req} + P_{EM,loss}. \quad \textbf{(5-3)}$$

Put differently, the power demand P_{req}, in addition to the electric motor power losses $P_{EM,loss}$, appears as the sum of the contributions of engine power, P_{ICE}, and battery power, P_{batt}.

The role of HEPS energy management of is to split the power demand appropriately between the combustion and electrical energy sources. Thus, the control variable of the powertrain is typically formulated relative to the engine output power, i.e. $u = P_{ICE}$.

When selecting the battery for energy storage, the state variable of the hybrid propulsion system is the battery's State-of-Charge (SoC), and is denoted by x. According to the definition of SoC, the system state transition equation can be written as:

$$\dot{x} = -\frac{I}{Q_{max}}, \tag{5-4}$$

where I is the current flowing supplied by the battery and Q_{max} is the battery maximum capacity.

In the energy management analysis of hybrid vehicle, the battery model is commonly described by an ideal open-circuit voltage source in series with an internal resistance [75]. It uses the open circuit battery voltage V_b and internal resistance R_b to obtain the battery output power P_{batt}:

$$P_{batt} = I * V_b(x) - I^2 R_b, \tag{5-5}$$

in which the resistance R_b is assumed to be constant.

In addition to system dynamics, the optimization must consider the physical limitations of each component, which could be expressed by the bounds of variables:

$$P_{ICE,min}(\omega_{ICE}) \leq P_{ICE} \leq P_{ICE,max}(\omega_{ICE}), \tag{5-6}$$

$$x_{min} \leq x \leq x_{max}, \tag{5-7}$$

$$I_{min} \leq I \leq I_{max}, \tag{5-8}$$

where the engine rotational speed is ω_{ICE}, and the engine power upper and lower boundaries change with ω_{ICE}.

The engine rotational speed is determined by the reference speed due to the mechanical link constraint:

$$\omega_{ICE} = r * \omega_{req}, \tag{5-9}$$

where r is the transmission ratio of the drivetrain.

5.1.2 Objective

In this study, the objective of the energy optimization is to minimize the fuel consumption of the engine during the overall flight mission. The cost function can be expressed by:

$$J = \int_{t_0}^{t_f} \dot{m}_f(P_{ICE})\, dt, \tag{5-10}$$

where $\dot{m}_f$ denotes the fuel consumption rate of the engine. The time $t \in [t_0, t_f]$, where t_f is the final time and the initial time t_0 generally starts at zero.

In sum, the original Problem (5-11) is to minimize the objective, J, in Eq. (5-11a)

$$J = \int_{t_0}^{t_f} \dot{m}_f(P_{ICE})\, dt, \tag{5-11a}$$

subject to:

$$P_{ICE} + P_{batt} = P_{req} + P_{EM,loss}. \tag{5-11b}$$

$$\dot{x} = -\frac{I}{Q_{max}}, \tag{5-11c}$$

$$P_{batt} = I * V_b(x) - I^2 R_b, \tag{5-11d}$$

$$P_{ICE,min}(\omega_{ICE}) \leq P_{ICE} \leq P_{ICE,max}(\omega_{ICE}), \tag{5-11e}$$

$$x_{min} \leq x \leq x_{max}, \tag{5-11f}$$

$$I_{min} \leq I \leq I_{max}, \tag{5-11g}$$

$$\omega_{ICE} = r * \omega_{req}. \tag{5-11h}$$

5.1.3 Approximation of Fuel Rate

In this case, the fuel rate (the integrand of the objective function) is not a convex function of the control variable, but it is piecewise linear (affine) dependent on the engine torque at a given speed (see Figure 5-1). In other words, the fuel rate at each speed can be addressed by:

$$\dot{m}_f = k(\omega_{ICE})\frac{P_{ICE}}{\omega_{ICE}} + d(\omega_{ICE}), \tag{5-12}$$

where k and d are parameters that are estimated by the piecewise linear approximation and will vary depending on engine speed.

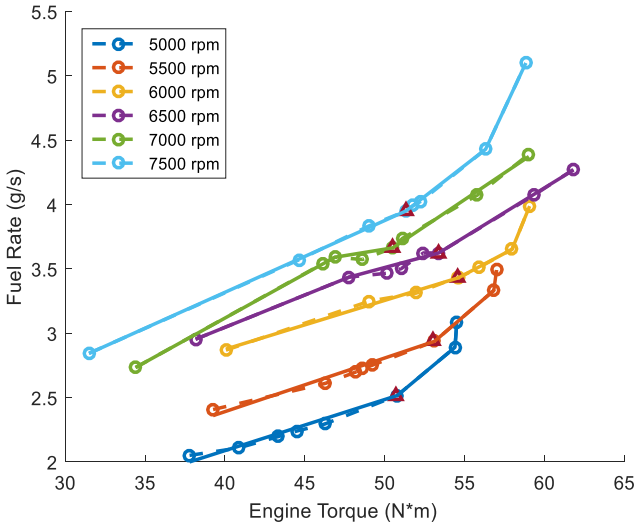

Figure 5-1 Piecewise linear approximation of the fuel rate at different speeds.

The results of piecewise linear approximation are plotted in Figure 5-1 as the solid curve. The first turning point (gradient change point) indicates the best efficiency for a

given speed, if the fuel rate curve is piecewise convex [62]. This condition is not fulfilled at 6500 rpm and 7000 rpm, so their best efficiency points move to the second turning point due to the presence of nonconvex segments. The best efficiency points at different speeds are marked by mauve triangular symbols in Figure 5-1. To avoid substantial distortion and shift of the best efficiency region, the best efficiency points need to be retained at their original values when implementing the approximation.

This following work will verify the piecewise linear approximation of fuel rate by comparing the original efficiency map and fitted data. Also, another efficiency map, which is computed from the fitted fuel rate using spline approximation, is also presented and compared with one using the piecewise linear approximation.

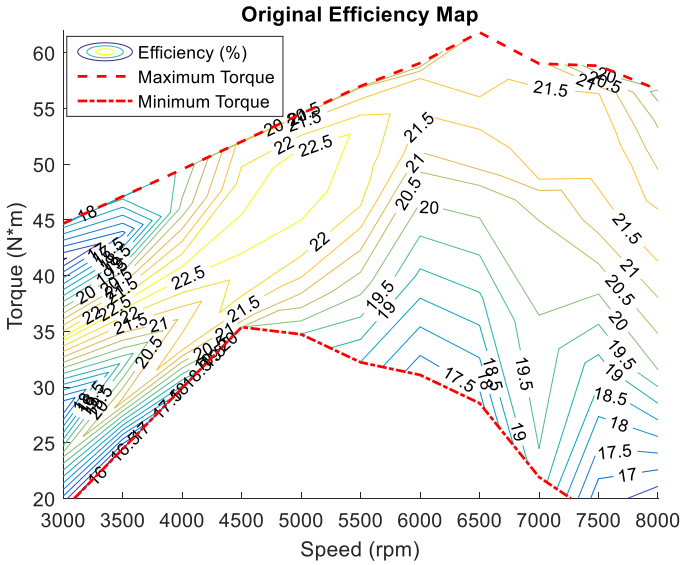

Figure 5-2 Original efficiency map

The original efficiency map of the engine is shown in Figure 5-2. It is obvious that the best efficiency region roughly falls between 4000-5500 rpm and 40-45 N*m. If possible, operating around this area can improve engine's efficiency and also extend its lifetime. For the same reason, it is not recommended to control engine to the region above the maximum continuous torque curve and below the minimum continuous torque curve.

A piecewise linear approximation of the engine fuel rate was introduced to convexify the cost function. The piecewise approximation was done by first specifying the best efficiency point at the current speed. The best efficiency point was kept at its original value when the fuel rate was approximated by a piecewise linear function, via the least square method. The efficiency map of the approximated data is shown in Figure 5-3,

with the original efficiency also shown. The dotted curve represents the original fuel rate data, with fitted data denoted by the dashed curve. It can be concluded that the piecewise linear fitting reflects the feature of the original data, especially around the area of best efficiency. The reason is that minimizing the fitting error for this portion of the data takes priority.

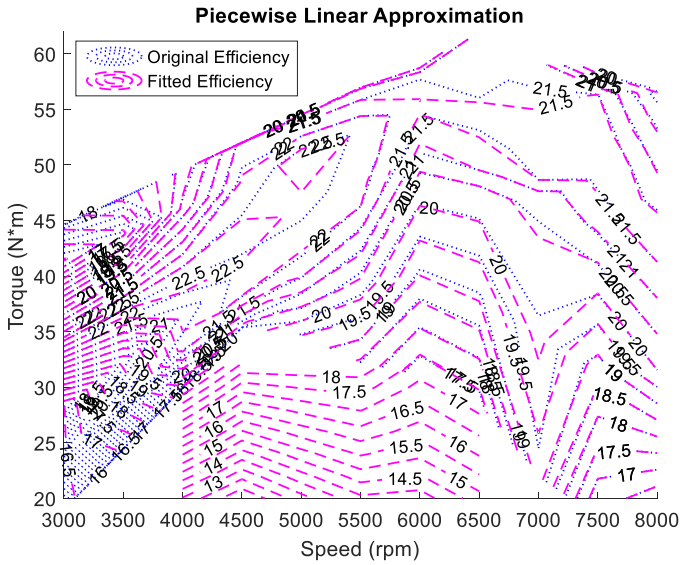

Figure 5-3 Piecewise linear approximation of the engine map

Another efficiency map from spline approximation is presented in Figure 5-4 as a comparison of piecewise linear approximation. The comparison demonstrates that both approaches can avoid a large shift of the best efficiency region, whereas the piecewise linear fitting performs better in keeping its original shape. On the other hand, the two methods both underachieve in fitting data around the region between 3000-4000 rpm and 20-35 N*m. This may be due to the deficiency of the original experimental data. However, it can be observed that our piecewise linear approximation tries to follow the gradient of the original data, while there occurs obviously overfitting for the spline approximation. The two techniques express different understandings when predicting the missing original data between 3000-7000 rpm and 20-35 N*m. It is not straightforward to judge which technique is better, but the piecewise linear approximation seems more reliable than the spline approximation that overreacts to minor fluctuations.

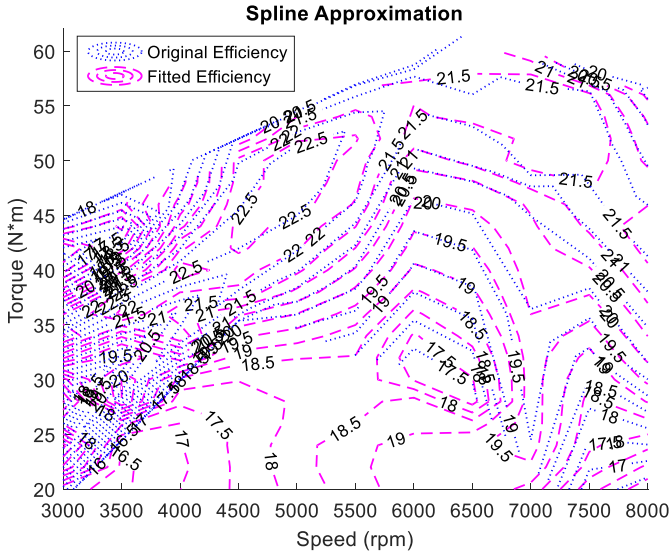

Figure 5-4 Spline approximation of the engine map

5.1.4 Flight Missions

There are two test cases for validating the designed optimization algorithm. The first test case is a complete mission that includes take-off, climbing, cruising and landing phases, where both the battery charge-depleting and charge-sustaining strategies are implemented in the hypothetical flight scenario. In the second, the charge-sustaining strategy is employed for the cruising flight phase.

The flight mission profile only highlights a few significant flight phases, by demonstrating their power demands. In our HEPS, the power requirement P_{req} is the sum of the power requested to drive the propeller and power demanded by the auxiliary devices of the aircraft (such as payloads, power electronics and supervisory controller). Note that the power requirement takes into account of the power loss of propeller propulsion. However, different from the estimation of power demand in the system sizing, the calculation of power demand here does not need to consider the power loss due to the variation of altitude. The reason is that the model of engine ECU control already takes the altitude coefficient e_{air} into account.

The test scenario 1 used in this thesis simulates a complete 30 minutes flight mission that includes take-off, climbing, cruising and landing phases. As shown in Figure 5-5, the system initialization and take-off are in the 1st minute, it then climbs to the cruising altitude in the time interval of the 1st-6th minute. The aircraft commences the cruising

phase at 7th minute. The cruising segment lasts for roughly 20 minutes. After the hypothetical cruising mission, the aircraft starts its landing around the 27th minute.

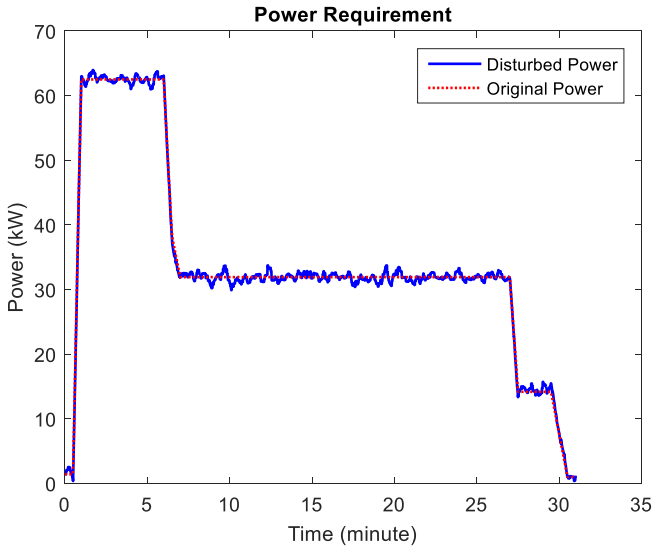

Figure 5-5 Power requirement of test case 1

Since in real flight, external factors such as wind will cause fluctuation of power demands, to increase the fidelity of the simulation, a disturbance is added to the original power requirement, as shown in Figure 5-5. The original power demand is normally used in the energy optimization control, while the disturbed power need is implemented on the simulation verification.

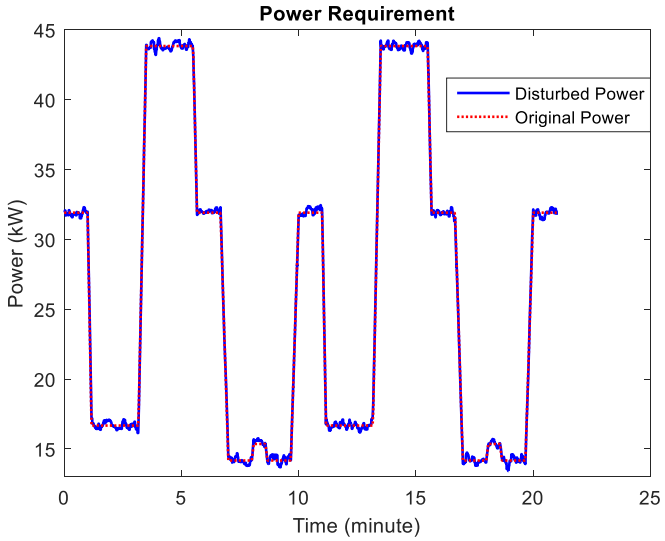

Figure 5-6 Power requirement of test case 2

As shown in Figure 5-5, the cruising phase is simplified to one segment with the constant power requirement. To investigate the optimization performance during the cruising, this segment is re-designed and set as the test scenario 2. Similarly, the power demand is added with the disturbance and compared with the original one in Figure 5-6. The power demand varies when the aircraft cruises at different airspeeds.

5.2 Dynamic Programming

Dynamic Programming (DP) is a numerical method originating to solve multi-stage decision-making problems. After being aware of its capability of finding the best control trajectory, researchers start to exploit it to solve optimal control problems. DP accords with the Bellman's principle of optimality [159]: An optimal policy has the property that whatever the initial state and initial decision are, the remaining decisions must constitute an optimal policy with regard to the state resulting from the first decision. In other words, from any point on an optimal trajectory, the remaining trajectory is optimal for the corresponding problem initiated at that point.

Consider the discrete-time system:

$$\dot{x}_{k+1} = f_k(x_k, u_k), \;\; k = 0,1, \dots, N-1, \tag{5-13}$$

where x_k and u_k are discretized state and control variable at collocation time point k, respectively. N is the number of discretization points.

The cost J of the decision $u(u_0, u_1, \dots, u_N)$ with initial state x_0 can be addressed by:

$$J(x_0, u) = L_N(x_N) + \sum_{k=1}^{N-1} L_k(x_k, u_k), \tag{5-14}$$

where L_k is the instantaneous cost function. $L_k(x_k, u_k)$ indicates the cost of moving from collocation time k to $k+1$. The minimum cost function is achieved with the optimal control u^*:

$$J^*(x_0) = \min_u J(x_0, u). \tag{5-15}$$

Then consider the remaining sub-problem of minimizing the cost-to-go Y from collocation time i to N:

$$Y(x_i, i) = L_N(x_N) + \sum_{k=i}^{N-1} L_k(x_k, u_k). \quad \textbf{(5-16)}$$

Bellman's principle of optimality states that the "tail policy", $\{u_i^*, u_{i+1}^*, \dots, u_{N-1}^*\}$, is the optimal solution for the remaining sub-problem. Put differently, the optimal control can be obtained by finding the best decision to minimize the cost-to-go at each step, from the final step N backward to the initial step.

Dynamic programming can be used to solve the optimal energy management problem defined in Section 5.1. Before applying the backward scanning, the candidate set of possible state (i.e. battery SoC) is created based on its bounds, at each step. The same procedure is done for the control variable, P_{ICE}. Then for the final step N, the instant cost $L_N(x_N)$ is computed using each state value in the candidate set. The backward searching starts from time $N-1$.

The instant cost $L_k(x_k, u_k)$ for all possible combinations of state and control is computed and stored. $L_k(x_k, u_k)$ indicates the fuel cost of moving from all possible SoC at step k to all admissible SoC at step $k+1$, using all reachable P_{ICE}. Then, a series of cost-to-go $Y(x_k, u_k, k)$ are computed to represent the cost to the end of time starting at step k from each possible state x_k using all possible u_k.

One of the most significant advantage of DP is that the cost-to-go $Y(x_k, u_k, k)$ can be calculated using the current cost $L_k(x_k, u_k)$ and the cost-to-go at time $k+1$. This can effectively reduce the computation since the algorithm proceeds backwards and $Y(x_{k+1}, u_{k+1}, k+1)$ have been computed. For each step, the control u_k resulting in minimum $Y(x_k, u_k, k)$ is marked and included to the optimal control sequence. When all time steps are examined, the control sequence with the lowest cost-to-go represents the complete optimal solution.

The most critical benefit of DP is that it is capable of providing the optimal solution to any problems, regardless of their complexity level. Therefore, DP can solve our discretized original problem directly. However, large computational cost exists in DP due to nonconvex characteristics of the energy optimization problem. Therefore, the optimization result from DP is usually used as a benchmark. More details on how to

develop the dynamic programming for hybrid propulsion system can be referred in [80,160].

5.3 Convex Optimization

Consider the optimization problem [161]:

$$\begin{aligned} &\text{minimize} && f_0(x) \\ &\text{subject to} && f_i(x) \le 0, \quad i = 1, \dots, m \\ & && a_i^T x = b_i, \quad i = 1, \dots, p \end{aligned} \tag{5-17}$$

where m and p are numbers of inequality and equality constraints, respectively. If $f_i(x)$, $i = 0, \dots, m$ are convex functions, the problem (5-17) is a convex optimization problem.

Comparing with the general standard form optimization problem, the convex problem has three additional requirements: 1) The objective function must be convex; 2) The inequality constraint functions must be convex; 3) The equality constraint functions must be affine.

Convex optimization is widely favoured since it can be solved, very reliably and efficiently [161]. Using interior-point methods, the problem can be guaranteed convergence to the global optimum with a deterministic upper bound on the number of iterations, without the requirement of a pre-supplied initial guess. In other words, the global optimality, lower complexity and no request of user-specified initial value make the convex programming very promising for practical applications.

The most challenging work of applying the convex programming is to convert the original problem into a convexified one. First, the convexity of cost and constraints is figured out with the approximation of experimental data. Then, the convexification is completed by changing variables (the battery power and SoC, etc.) and relaxing the power equivalent equation. The lossless of this convexification is also proved in this part of the study.

5.3.1 Approximation of Experimental Data

The approximation is normally employed to reveal the inherent correlation between different variables with an algebraic expression, by analysing the original numerical data from experiments. What is more, the convexity of cost and constraints can also be investigated thoroughly.

In this case, the fuel rate (the integrand of objective function) is not a convex function of the control variable, but it is piecewise linear (affine) dependent on engine torque at a given speed as presented in Section 5.1.3.

In this study, the plot of battery voltage as a function of SoC can be divided into three segments. The experimental data and turning points are shown in Figure 5-7. It is clear that the function V_b is nonlinear and also nonconvex. Fortunately, to extend the lifetime of the battery, the SoC is typically limited between 20% and 80%. The voltage between 20% and 80% is convex and can be accurately fitted with a quadratic function of the form: $V_b = a_v x^2 + b_v x + c_v$.

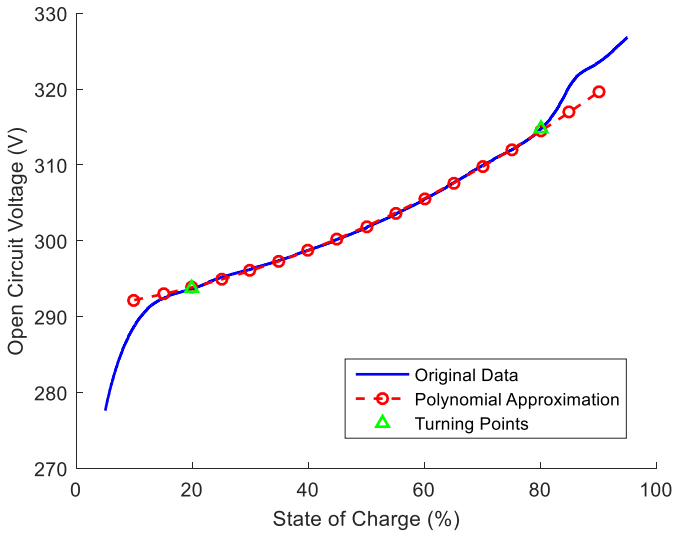

Figure 5-7 Approximation of open circuit voltage along the operating range of battery

The convex approximation result is also marked in Figure 5-7, using the dashed curve with red circles. When the coefficients (a_v, b_v, c_v) are (24.95, 9.319, 291.0), respectively, the coefficient of determination is 0.9993. Note that the voltage is broadly fitted with a constant or affine function, to further simplify the model. However, the

constant or affine function is neither applied here due to its lower accuracy. On the other hand, the quadratic function performs well but leads to concave inequality constraints. This issue will be illustrated in Section 5.3.2.1.

The power loss of electric motor was calculated using efficiency map supplied by the manufacturer. From the previous research in Section 4.2.1 and 4.2.2, the power loss of the electric motor is actually dependent on the speed and torque. In this thesis, the correlation between power loss and torque/speed was analysed first. It was found that the distance correlation between power loss and torque is only 0.0541. This means that the power loss is only slightly influenced by torque. This is demonstrated in Figure 5-8 that presents the relationship between power loss and speed under difference torques.

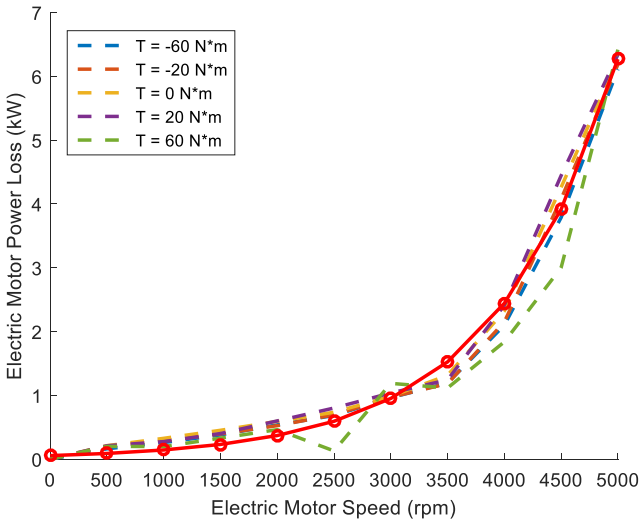

Figure 5-8 Approximation of the power losses of the electric motor

As a result, the power loss can be approximated in a formula which involves only speed, using the convex function $P_{EM,loss} = a_m * \exp(b_m \omega_{MG})$. The fitting results are also plotted in Figure 5-8, with the red solid line marked with circles. The fitted coefficient are $a_m = 0.0563$, $b_m = 9.4248 * 10^{-4}$, when the speed unit is revolutions per minute (rpm). The coefficient of multiple determination is 0.9919. It is worth noting that the observed data used in the fitting is the mathematical expectation of original power loss data at different torques.

By analysing the experimental data, the fuel rate map is estimated with a series of piecewise linear expression. The operating region of the battery voltage is also shown

to be convex. Meanwhile, the power loss of EMs is proved to be mainly dependent on output speed, instead of output torque.

5.3.2 Lossless Convexification

The convexity of the original Problem represented by Eq. (5-11) is examined in Section 5.1.3 by evaluating the experimental data. The objective function is found to be convex with the piecewise linear integrand. The variable bounds (5-11**e**-**g**) and mechanical constraint (5-11**h**) are affine, but equality constraints (5-11**b**-**d**) do not satisfy the requirement of convex programming [161].

In the following section, a convexification including change of variables and equality relaxation, is carried out to convert the Problem represented by Eqs. (5-11) into a convex Problem represented by Eqs. (5-28).

5.3.2.1 Change of Variables

Internal power of battery P_b which does not include power loss is proposed in this thesis, then the equality constraints (Eqs. (5-11**b**) and (5-11**d**)) become:

$$P_{ICE} + P_b = P_{req} + P_{EM,loss} + P_{b,loss}, \quad \textbf{(5-18)}$$

$$P_b = I * V_b(x). \quad \textbf{(5-19)}$$

The power loss of the battery, $P_{b,loss}$ defined here is mainly due to the power dissipated in the resistance, which is dependent on the internal battery power and battery SoC (see Figure 5-9). Similar to $P_{EM,loss}$, the distance correlation between power loss and SoC is only 0.0810. In other words, the power loss is correlated mainly with battery power, rather than SoC. $P_{b,loss}$ can be fitted with a simple convex quadratic function: $P_{b,loss} = a_l P_b^2$. The fitted coefficient is $a_l = 3.24 * 10^{-6}$, with its coefficient of multiple determination being 0.9998. The observed data used in the fitting is the mathematical expectation of the original power loss data at different SoC. Note that by introducing the battery internal power P_b, the power loss is transformed to a symmetrical graph across the y-axis, which simplifies the formulation of battery model and the proof of *Lemma 1* as follows in Section 5.3.2.2.

Now, the inequality (5-11**g**) becomes:

$$I_{min} \leq \frac{P_b}{V_b(x)} \leq I_{max}, \tag{5-20}$$

which is affine in the battery internal power P_b, but does not guarantee the convexity of the battery voltage $V_b(x)$.

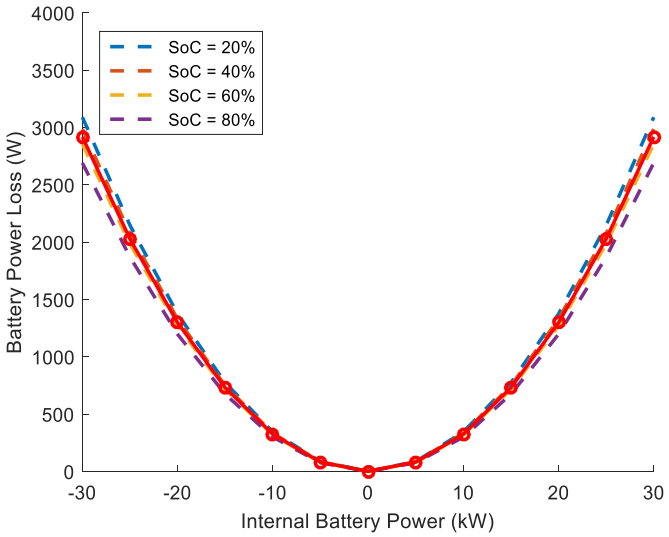

Figure 5-9 Approximation of the battery power losses

Consider approximating $V_b(x)$ with two affine functions: $V_{lb}(x)$ and $V_{ub}(x)$, as illustrated in Figure 5-10, with black dotted and solid lines, respectively. The $V_{lb}(x)$ is the Taylor expansion of $V_b(x)$ at $x = 0.5$, while the line defined by $V_{ub}(x)$ goes through two points at 20% and 80% SoC.

Because of the convexity of $V_b(x)$, $V_{lb}(x)$ and $V_{ub}(x)$ suggest the lower and upper bounds of the voltage:

$$I_{min}V_b(x) \leq I_{min}V_{ub}(x),\ I_{max}V_b(x) \geq I_{max}V_{lb}(x). \tag{5-21}$$

Thus the following constraints need to be satisfied:

$$I_{min}V_{ub}(x) \leq P_b \leq I_{max}V_{lb}(x). \tag{5-22}$$

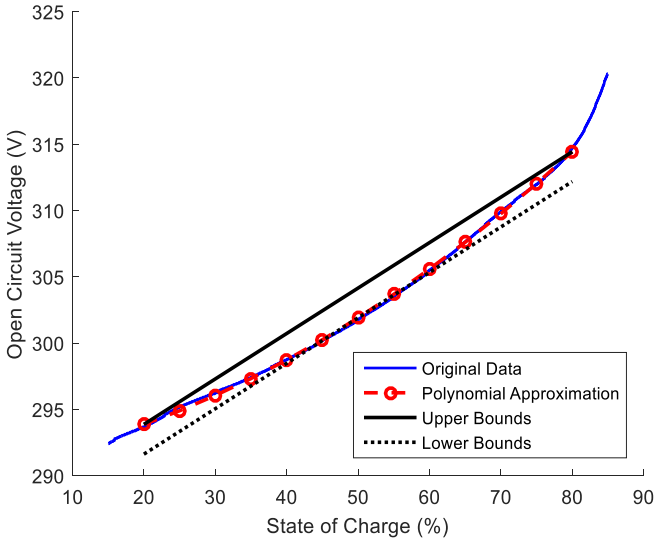

Figure 5-10 Upper and lower bounds of the open circuit voltage

By solving the problem within the bounds of these constraints (see Eq. (5-22)), one never obtains solutions that violate the constraints imposed by the physical problem. The bounds on errors (e_{lb}, e_{ub}) introduced by second approximation of $V_b(x)$ were computed and are displayed in Figure 5-11. The figure clearly shows that the percentages of errors of upper and lower bounds are both smaller than 1%. Put differently, for all practical purposes, the inequalities Eq. (5-20) are not compromised when replaced by Eq. (5-22).

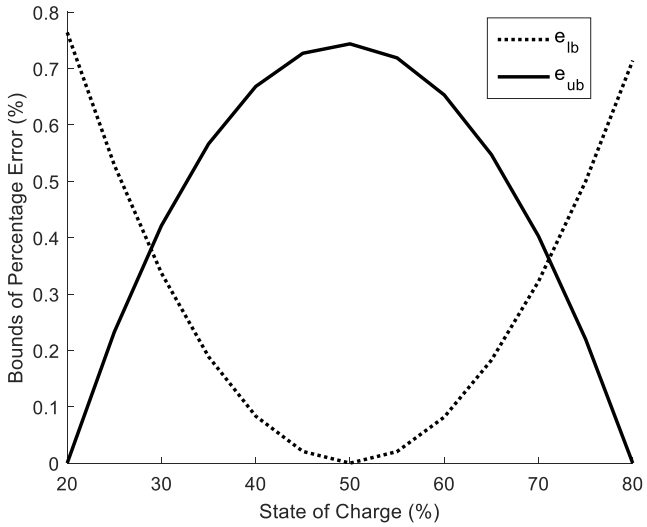

Figure 5-11 Error bounds of the second approximation

From Eq. (5-11**c**) and Eq. (5-19), the state equality function can be deduced:

$$\dot{x} = -\frac{P_b}{V_b(x)Q_{max}}, \tag{5-23}$$

which still does not meet the requirement of convex programming. Therefore, a new variable called battery internal energy E is introduced to replace the original state variable (SoC). The new state transition equality is formulated as:

$$\dot{E} := Q_{max}V_b(x)\dot{x} = -P_b, \tag{5-24}$$

while x still denotes the battery SoC to maintain consistency. Simple integration leads to:

$$E(x) = Q_{max}\int V_b(x)dx = Q_{max}\left(\frac{1}{3}a_v x^3 + \frac{1}{2}b_v x^2 + c_v x + d_v\right), \tag{5-25}$$

where d_v is set to zero without loss of generality. Meanwhile, the inequality (5-11**f**) is transformed into:

$$E_{min} \leq E \leq E_{max}. \tag{5-26}$$

Since $E(x)$ monotonically increases with x in the domain of definition, E_{min}, E_{max} are calculated using $E(x_{min})$ and $E(x_{max})$, respectively.

5.3.2.2 Constraint Relaxation

Similarly, by the substitution of variables, the equality (5-11**b**) is converted to the convex equality Eq. (5-18) to prepare for the formulation of the new convex problem. Subsequently, the relaxation of Eq. (5-18) yields to the inequality constraint:

$$P_{ICE} + P_b \geq P_{req} + P_{EM,loss} + P_{b,loss}. \tag{5-27}$$

As a consequence, the non-affine equality is successfully converted to a convex inequality. This relaxation does not prejudice the optimality of the solution. The detailed reasoning supporting this statement is given in [109]. Assuming that the convex solver

finds the optimal solution while respecting $P_{ICE} + P_b > P_{req} + P_{EM,loss} + P_{b,loss}$, it would mean that some of the energy supplied by the fuel and battery was wasted, thus a better solution can be found via Eq. (5-27), while maintaining the equality. Proof of this proposition will be given in *Lemma 1*.

The constraint relaxation leads to a convex fuel optimization problem. The convex formulation of the original Problem (5-11) is re-constructed as Problem (5-28):

$$J = \int_0^{t_f} \left(k(\omega_{ICE}) \frac{P_{ICE}}{\omega_{ICE}} + d(\omega_{ICE}) \right) dt, \;\; k > 0, \tag{5-28a}$$

subject to:

$$P_{ICE} + P_b \geq P_{req} + P_{EM,loss}(\omega_{EM}) + P_{b,loss}, \tag{5-28b}$$

$$\dot{E} = -P_b, \tag{5-28c}$$

$$P_{ICE,min}(\omega_{ICE}) \leq P_{ICE} \leq P_{ICE,max}(\omega_{ICE}), \tag{5-28d}$$

$$E_{min} \leq E \leq E_{max}, \tag{5-28e}$$

$$I_{min} V_{ub}(x) \leq P_b \leq I_{max} V_{lb}(x), \tag{5-28f}$$

$$\omega_{ICE} = G * \omega_{EM} = r * \omega_{req}, \tag{5-28g}$$

in which the motor speed ω_{EM} is related to the engine speed by the gear ratio G.

Lemma 1: The optimal solution of the original Problem (5-11) can be accomplished by solving the relaxed convex Problem (5-28). In other words, a sufficient condition for reaching the minimum of Problem (5-11) is that the constraint (5-28b) holds with equality at the optimum of Problem (5-28).

Proof: Assume that an optimal solution of Problem (5-28) is found that satisfies:

$$P_{ICE}^* + P_b^* > P_{req} + P_{EM,loss} + P_{b,loss}^*. \tag{5-29}$$

It is possible to construct a suboptimal solution with the same battery internal power and power loss trajectory, i.e. $\tilde{P}_b = P_b^*$, $\tilde{P}_{b,loss} = P_{b,loss}^*$. In the meantime, this feasible solution maintains the condition:

$$\tilde{P}_{ICE} + \tilde{P}_b = P_{req} + P_{EM,loss} + \tilde{P}_{b,loss}. \quad \textbf{(5-30)}$$

It can then be inferred that:

$$P_{ICE}^* > \tilde{P}_{ICE}. \quad \textbf{(5-31)}$$

Meanwhile, the cost, J, increases monotonically with P_{ICE}. Consequently, the following inequality can be deduced:

$$J^* > \tilde{J}, \quad \textbf{(5-32)}$$

which contradicts the assumption that P_{ICE}^* is the optimal solution of Problem (5-28). That means Eq. (5-28**b**) holds with the condition of equality at the optimum. Therefore, the relaxation does not lead to any loss of the original optimality.

5.3.3 Discretization

The discretization is implemented subsequently on the convexified Problem (5-28), since the numerical optimization algorithm requires the discrete version of the control problem. The discretization procedure converts the infinite dimensional optimization problem to a finite-dimensional one by discretizing the system at specific time nodes. The constraints are also converted to a discrete formation and imposed at the collocation points.

For a given time interval $[t_0, t_f]$, and time increment array, $\Delta t_k, k = 1, \ldots, N$, the collocation nodes can be expressed as:

$$t_k = t_{k-1} + \Delta t_k, \ \ k = 1, \ldots, N, \quad \textbf{(5-33)}$$

in which t_0 is normally set to 0. Then, the priori-known power requirement and speed reference are converted to $P_{req}(t_k)$ and $\omega_{req}(t_k)$. As illustrated in the Section 5.1.3, the power loss of EMs is related only to the motor/generator speed, it can be transformed to a pre-known variable $P_{EM,loss}(t_k)$.

The most important step in the discretization of the problem is to obtain the discretized control input u. Then, all other variables (like system states) can be represented by the control variable $u(t_k)$.

With the convex relaxation of equality (5-10**b**), the original control variable has to be extended to:

$$u(t_k) = \begin{bmatrix}\sigma_1(t_k)\\ \sigma_2(t_k)\end{bmatrix} = \begin{bmatrix}P_{ICE}(t_k)\\ P_b(t_k)\end{bmatrix},\ k = 1,\dots,N, \qquad \textbf{(5-34)}$$

where $\sigma_1(t)$ and $\sigma_2(t)$ are introduced to represent the continuous formation of the control input u.

The control variable is broadly constructed on the basis of some prescribed continuous basis functions, $\phi_j, j = 1,\dots,M$ [162]:

$$\begin{bmatrix}\sigma_1(t)\\ \sigma_2(t)\end{bmatrix} = \sum_{j=1}^{M}(\eta_j\phi_j),\quad j = 1,\dots,M. \qquad \textbf{(5-35)}$$

Thus, the control input at the collocation points $u(t_k)$ can be addressed by:

$$\begin{bmatrix}\sigma_1(t_k)\\ \sigma_2(t_k)\end{bmatrix} = I_k\mathrm{H},\quad k = 1,\dots,N, \qquad \textbf{(5-36)}$$

where I_k is the matrix function of time index determined by the selected basis functions and $\mathrm{H} = [\eta_1,\dots,\eta_M]$. After acquiring the discrete control (engine and battery power), the cost and constraints can be represented by the $u(t_k)$.

If the piecewise constant basis functions are applied:

$$\phi_j(t) = \begin{cases}1, & t \in [t_{j-1}, t_j]\\ 0, & \text{otherwise}\end{cases},\quad j = 1,\dots,M, \qquad \textbf{(5-37)}$$

which indicates that:

$$\eta_j = \begin{bmatrix} \sigma_1(t_{j-1}) \\ \sigma_2(t_{j-1}) \end{bmatrix},\ j = 1, \ldots, N, \quad \textbf{(5-38)}$$

and $M = N$. The procedure corresponds to zero-order-hold discretization of a time-invariant system.

5.4 Numerical Examples

To validate the proposed convexification and convex programming, two different hypothetical flight test scenarios are considered. The first test case is a complete mission that includes take-off, climbing, cruising and landing phases, where the battery charge-depleting and charge-sustaining strategy are both implemented on convex programming. Secondly, the charge-sustaining based convex optimization is employed on a cruising flight phase and its performance is compared with the DP. Furthermore, the optimal controls of two scenarios are conducted and verified on a forward simulation model developed in the previous Chapter 4.

5.4.1 Convex Optimization

This section validates the optimal results of convex programming, using test scenario 1. This test case simulates a complete 30 minutes flight mission that includes take-off, climbing, cruising and landing phases. The details of this hypothetical mission are given in Section 5.1.4. Regarding the SoC-regulating strategy, the initial value of battery SoC is set to 60%. The maximum and minimum value of SoC are 80% and 20%, respectively, considered the operating range of the battery. When the SoC depletes to 30%, then the energy management maintains the SoC around this value, to extend the lifetime of the battery.

5.4.1.1 Lossless Optimal Results

The power requirement of this flight mission is shown in Figure 5-12 (a) as the dark blue dotted line, in addition the figure also shows the optimal engine power, the battery internal power and the power consumed. The power consumed is the sum of useful

power and power losses, namely $P_{ICE} + P_b - P_{EM,loss} - P_{b,loss}$. As shown in Figure 5-12 (a), the power consumption is equal to the power requirement, i.e. $P_{ICE} + P_b - P_{EM,loss} - P_{b,loss} = P_{req}$ being satisfied at each and every time node. That means Eq. (5-28**b**) holds under the equality condition at the optimal trajectory. In other words, the relaxation presented in Section 5.3.2.2 does not affect the results of the optimization.

Figure 5-12 (b) displays the optimal state variable E with a red dotted line. Note that this virtual variable E has no precise physical definition, and thus cannot reflect the actual remaining energy of the battery. The original state SoC is computed from internal energy E and plotted alongside the internal energy. In this case, the SoC value during the mission satisfies the original variable bounds and meets the requirement of the SoC-regulating strategy. The optimal SoC demonstrates that the convex optimization can realize both depleting and sustaining strategies. It also demonstrates that the change of state variable in convexification retains the original variable bounds.

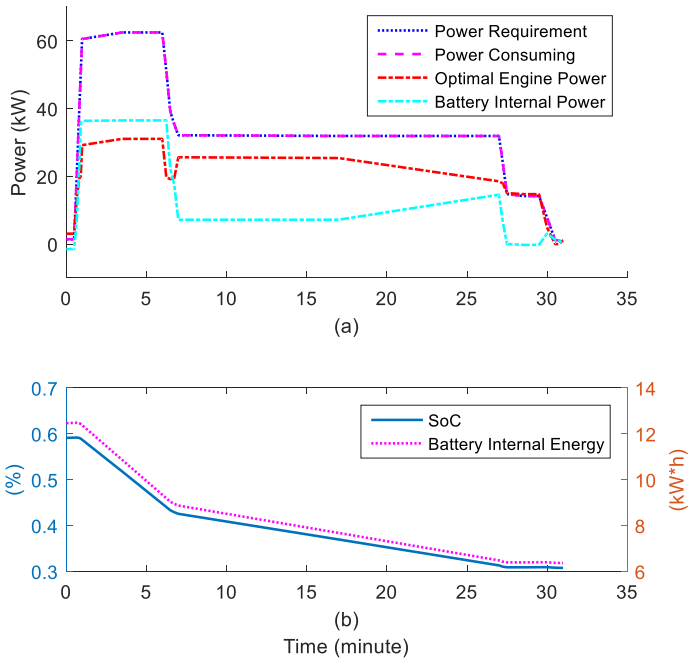

Figure 5-12 Optimization results of convex programming

In short, the convexification procedures proposed in this thesis do not lead to any loss of original optimality and the optimization of convexified problem gives the same solution of the original problem.

5.4.1.2 Forward Simulation

The optimal control is implemented in the forward simulation model. Note that the power requirement with disturbance is used for the numerical simulation.

Similarly, Figure 5-13 gives the simulation results of convex programming, including the engine and motor/generator power, in addition to battery SoC. As shown in Figure 5-13 (a), the simulation result of engine and motor/generator power basically follows the optimized one. For most of the time during the mission, the engine power fluctuates with the power disturbance but maintains convergence and good performance. It implies that the optimal control is robust to the disturbances.

The supervisory controller requests energy from both combustion and electrical sources to power the aircraft during the lift-off (around 1 min). The power demand for the engine and motor/generator reach to their maximum power during the climbing part, between 1st and 6th minute. Regarding the cruising phase, the engine contributes almost two-thirds of power requirement, while the motor/generator facilitates the propeller driven. The output engine power decreases while the motor/generator power increases from about 20th minute. Those two values becomes similar at the end of the cruising flight. The motor/generator functions as the generator to charge the battery, when the power requirement is low in the system initialization and final taxiing parts.

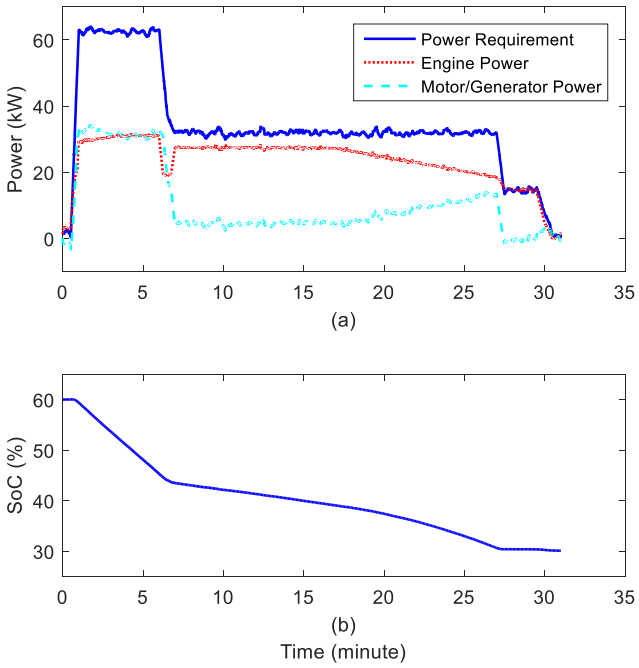

Figure 5-13 Simulation results of convex programming (1)

The motor/generator power is monitored in the numerical simulation instead of the battery one, since the battery internal power cannot be observed in the real application. This replacement is reasonable since both of them can reflect the consumption of electric power.

Figure 5-13 (b) displays the simulation results for SoC. Though the SoC varies from the optimized one, it still accomplishes both depleting and sustaining strategies. The SoC increases in the 1st minute, due to the battery charging during the initial ground-roll run. Later, it drops by a large margin with the aircraft's demand for power for lift-off and climb. The SoC continuously decrease during the cruising phase and the margin becomes larger in the time interval of the 20th-26th minute. Once the SoC reaches the 30% level (set as the sustaining value in this test case), the controller maintains it at that level.

Figure 5-14 compares the results of the engine power, motor/generator power, battery power and SoC, between the forward simulation and the optimization. The figure demonstrates that the simulation engine power matches the optimal one, while there is difference between the motor/generator power and battery internal power. This difference is small and mainly due to the power loss in electrical energy path. Different from the simulation results of engine and motor/generator, the simulation value of SoC differs from the optimized one. This is partly due to the fluctuation of control variable (engine power), but the main error comes from the battery model.

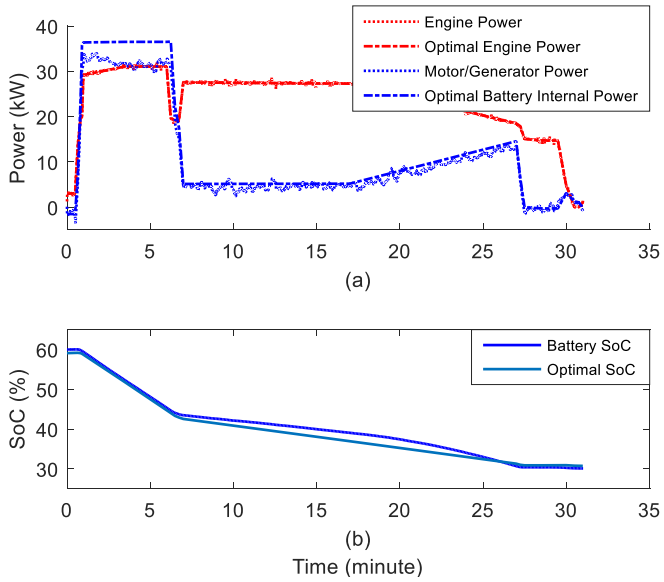

Figure 5-14 Comparison between simulation results and optimal results

Figure 5-15 and Figure 5-16 give simulation results of other variables, such as speed, torque, current and voltage. From Figure 5-15 (a), it is obvious that the engine and motor/generator can achieve good speed performance. The torque values in Figure 5-15 (b) also indicates the charge state at the initial and final part of the mission, with negative torque values of motor/generator. From Figure 5-15 (b), the torque of motor/generator is more vulnerable to the fluctuation of power requirement, since electric machines have a smaller time constant than combustion engines. In other words, the integration of electric motor can reduce the fluctuation of engine output, thereby improving the working condition of the combustion engine.

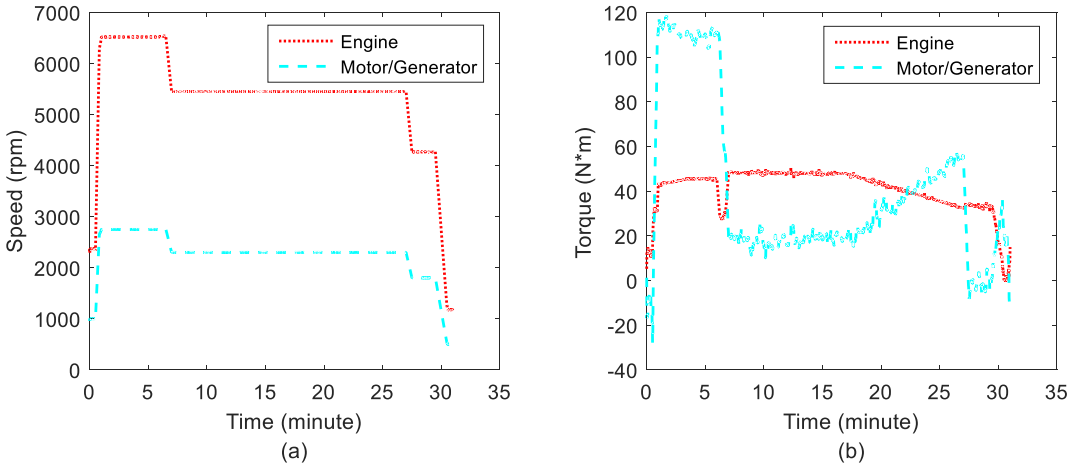

Figure 5-15 Simulation results of convex programming (2)

As shown in Figure 5-16, the output current and voltage of the DC/DC converter are compared with ones of the battery, which is equal to the input current and voltage of the DC/DC converter. The output voltage of the DC/DC converter is stabilized to 300 V, which is higher than the voltage of the battery. As a result, the output current of the DC/DC converter is not higher than one of the battery. The voltage of the battery decreases sharply when the discharging current is high between 1st and 6th minute. It recovers to nearly 280 V when the drawing current reduces to around 20 A. Then, the voltage continuously falls by the final part of the mission. Before the landing part, the output current rises to 40 A, since the SoC has not reached its sustaining value yet.

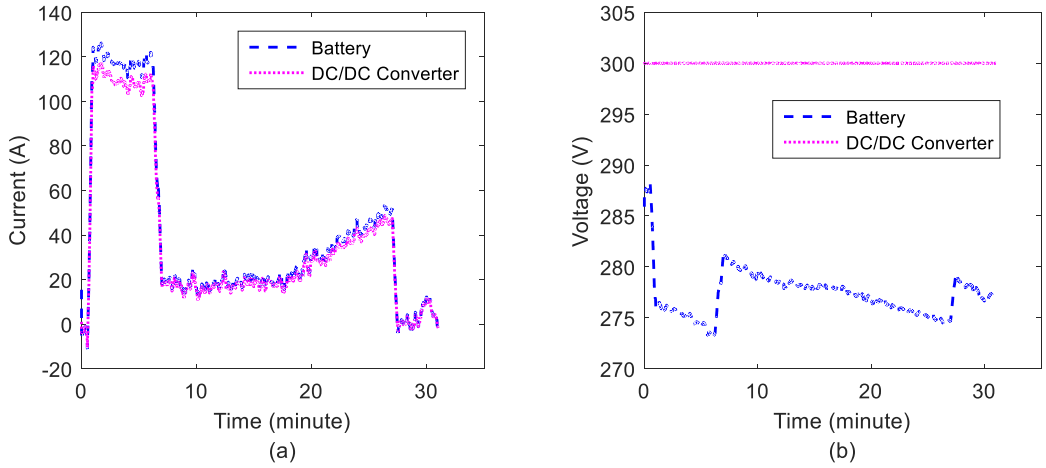

Figure 5-16 Simulation results of convex programming (3)

In sum, the optimal control has a potential to be applied to the practical application with a degree of robustness.

5.4.2 Comparison

This section compares the results from convex programming with ones from another global optimization—DP, using the second test instance. Similar to the test case 1, the forward simulation technique is applied and the disturbance to power demand is added.

5.4.2.1 Test Case 2

In the test scenario 2, the battery SoC is demanded to sustain around 50%. The initial value of battery SoC is also set to 50%. The maximum and minimum value of SoC are still 80% and 20%, respectively.

Figure 5-17 compares the simulation results of battery SoC and fuel consumption between convex optimization and DP. The initial value of SoC is set to 50% and its value is supposed to be sustained in the 20-minute whole cruising. The curves of SoC verify that both optimizations can realize the charge-sustaining, but the convex optimization obtains a more precise regulation of SoC than DP. Moreover, the convex optimization can achieve better optimal objective value, i.e. fuel consumption, than DP. Note that since the SoC trajectory of convex programming and DP are not exactly the same, the direct comparison between fuel consumptions cannot reflect which one is better regarding the fuel saving. The SoC correction is introduced in this study to adjust

the fuel consumption, since many researches [62] claim that fuel consumption in HEPS should be evaluated for the balanced energy content of their electric storage devices.

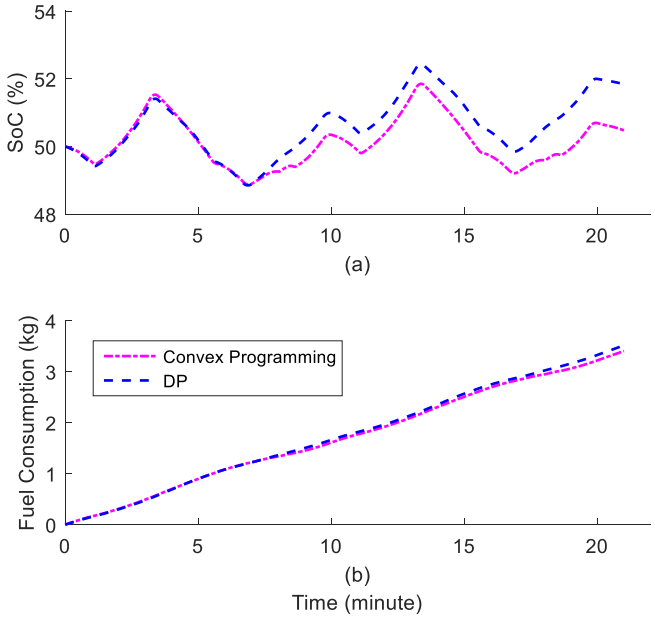

Figure 5-17 Comparison of simulation results between convex optimization and dynamic programming (1)

The details of fuel/energy saving and computational cost of two optimizations are given in Table 5-1. The final SoC for convex programming (50.47%) is lower than for DP (51.85%), which means the convex programming implies greater consumption of electric energy. The extra electric energy stored in the battery with DP is the cause of the additional fuel consumed. The real fuel consumption of two optimizations can be acquired by adjusting two final SoC values to the same one. This process is the above-mentioned SoC correction.

The corrected SoC and fuel usage are also displayed in Table 5-1. The figures show that the convex optimization really has lower fuel usage (3.39) compared with DP (3.48). Apart from the amount of fuel used, another criterion—energy consumption, which includes the fuel usage and electrical energy consumption, also indicates that the convex optimization demands less energy to complete the flight mission. This implies that the optimal trajectory of convex optimization results in better energy efficiency. Note that the study assumes that the gasoline is applied and its energy density (12.89 kW*h/kg) is used to estimate the energy of a certain fuel.

Table 5-1 Comparison of optimization results between convex optimization and dynamic programming

	Convex Programming	Dynamic Programming
Final SoC (%)	50.47	51.85
Fuel Consumption (kg)	3.40	3.52
Corrected Final SoC (%)	50.00	50.00
Corrected Fuel Consumption (kg)	3.39	3.48
Energy Consumption (kW*h)	43.7	45.0
Optimization Time (sec)	0.40	4.65

The most important advantage of convex programming is reduced computational cost of non-causal optimization. It is generally accepted that global optimization such as DP normally has low efficiency and an exponentially growing (worst-case) complexity [161]. Theoretically, with the same problem dimension and convergence accuracy, the convex optimization should have much lower computational cost than DP.

For the same problem given in test case 2, it takes around 4.65 sec for DP to converge, while convex programming is over ten times faster and the optimization time is only 0.4 sec (see Table 5-1). Confirming that the convexification simplifies the original problem and largely reduces the complexity cost. Considering 3GHz CPU and 2GB memory used in this study, the convexified problem is applicable to be converted to the real-time implementation.

The simulation results of the engine and motor/generator power from two optimizations are given in Figure 5-18, in addition to the power request. Figure 5-18 (a) compares the optimal engine power between convex optimization and DP. They both follow the change of power demand, e.g. increasing when the power demand is rising, vice versa. The main difference is that the DP draws more combustion power, while the convex programming prefers the electric powertrain. In terms of motor/generator power shown in Figure 5-18 (b), the motor/generator works at charging mode when the power requirement becomes relatively lower, while it outputs power to facilitate the cruising flight if the power demand is higher.

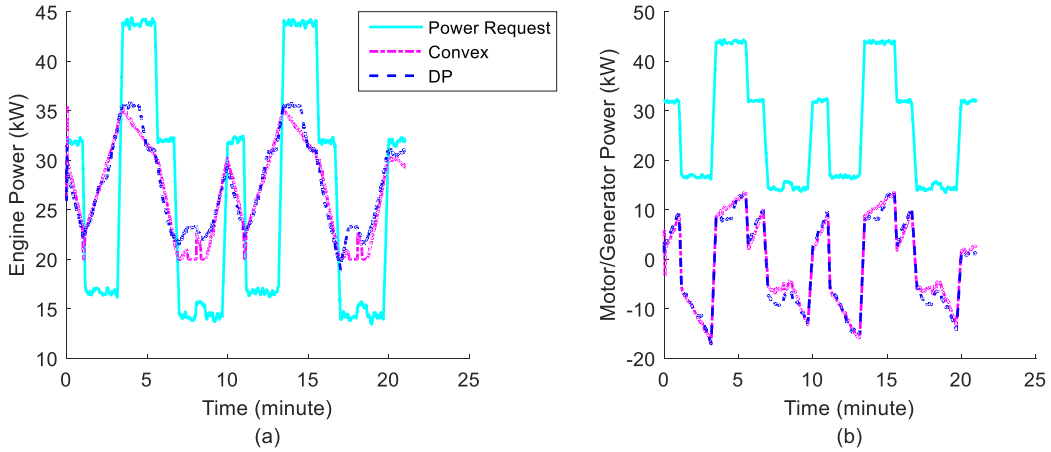

Figure 5-18 Comparison of simulation results between convex optimization and dynamic programming (2)

In sum, the forward simulations demonstrate that optimal controls of the two methods are both practical in real application.

5.5 Conclusion

This chapter presented the energy management of the hybrid electric propulsion system using two non-causal controls: convex optimization and dynamic programming. The design of convex optimization was illustrated in detail.

The simplified models were applied to study the energy management of hybrid propulsion systems and to formulate the primary problem. The experimental data were analysed and approximated to clarify the convexity of the original problem. Under the operating range, the battery voltage is able to be approximated with a quadratic equation. The examination also shows that the power loss of motor is mainly dependent on the motor speed with an exponential function. Concerning the engine fuel approximation, the comparison reveals that piecewise linear fitting not only performs better in keeping the original shape of the best efficiency region, but also in data prediction than spline approximation.

However, the battery model and power equality still do not satisfy the requirement of convex programming. Hence, two techniques—change of variables and equality relaxation were implemented with the need for lossless convexification. A variable named battery internal voltage was proposed in this thesis to convexify the battery

model and power equality. The corresponding variable bounds, such as current and SoC limits, were also converted and convexified. Finally, the relaxation of non-affine equality yielded to a new inequality constraint. A Lemma is also proposed and proved to establish that this convexification does not lead to any loss of original optimality. Subsequently, the discretization is implemented on the new convexified problem.

Two different hypothetical flight test scenarios were designed in this thesis. The first one includes the complete flight process (take-off, climbing, cruising and landing), while the second test case enriches the cruising phase of the first one by varying the power demands based on different cruising airspeeds. Those two test cases were applied to validate the optimality of the convex optimization, under different flight missions.

The first test case verifies that the convex relaxation does not sacrifice the optimality of the solution nor does the variable change lose the original bounds. With the forward simulation, the optimized control from convex optimization is testified to be robust to the disturbance in power demand. Also, it can reach optimal results under both charge-depleting and charge-sustaining strategies.

The dynamic programming was also implemented in the second test scenarios. By comparing with dynamic programming, the convex optimization achieves better optimal cost results. Most significant advantage of convex optimization is that it can converge to the optimal solution with a much lower time cost than dynamic programming method. This makes the convex optimization more attractive for practical applications.

6 Causal Energy Management

In causal energy management, our proposed algorithm—the fuzzy based Equivalent Consumption Minimization Strategy (ECMS) is compared with the conventional ECMS and adaptive ECMS.

The Hamiltonian function is introduced to transform the original non-causal fuel minimization into a causal optimization. The equivalence factor and the new instantaneous cost are derived from the Hamiltonian function. The new instantaneous cost is also considered as the equivalent consumption. The ECMS can optimize the equivalent consumption but not guarantee the sustaining of battery SoC. Therefore, a fuzzy controller is designed to maintain the battery SoC in a desirable range. The main work of developing a fuzzy controller is to design the corresponding membership functions and fuzzy rules. The instantaneous SoC value is fuzzificated by its membership functions and regulated by fuzzy rules.

The proposed fuzzy based optimization is validated by the comparison with the conventional ECMS, adaptive ECMS and dynamic programming, via two hypothetical flight scenarios. Moreover, the PMP is studied to validate the established relationship between the equivalence factor of ECMS and the co-state variable of Hamiltonian function.

6.1 Equivalent Consumption

Basically, the original problem of causal energy optimization shares the same constraints as the one of non-causal optimization. The constraints of the causal optimization problem are given by equations (6-1a)-(6-1g).

$$P_{ICE} + P_b = P_{req} + P_{EM,loss}(\omega_{EM}) + P_{b,loss}, \quad \textbf{(6-1a)}$$

$$\dot{x} = f(x,u) = -\frac{P_b}{V_b(x)Q_{max}}, \quad \textbf{(6-1b)}$$

$$P_{ICE,min}(\omega_{ICE}) \leq P_{ICE} \leq P_{ICE,max}(\omega_{ICE}), \quad \textbf{(6-1d)}$$

$$x_{min} \leq x \leq x_{max}, \quad \textbf{(6-1e)}$$

$$I_{min} \leq I \leq I_{max}, \quad \textbf{(6-1f)}$$

$$\omega_{ICE} = G * \omega_{EM} = r * \omega_{req}. \quad \textbf{(6-1g)}$$

Though subject to the same constraints (system state and component limitation), non-causal and causal problems employ different approaches to express the cost function.

6.1.1 Objective

As same as the convex optimization, the objective of the causal optimization is to minimize the total fuel consumption. Traditionally, this issue is formulated into a non-causal optimization problem:

$$J = \int_{t_0}^{t_f} \dot{m}_f \, dt. \quad \textbf{(6-2)}$$

However, it generally requires unknown priori knowledge (like the complete flight mission). To avoid this drawback, the original ECMS proposes to replace the non-causal criterion by an instantaneous one [130], reducing the problem to a minimization of equivalent fuel consumption at any instant of time.

If considering the energy optimization as the optimal control problem, the optimal control also minimizes the Hamiltonian function:

$$H = \dot{m}_f + \lambda \cdot f(x,u), \tag{6-3}$$

where $f(x,u)$ is the system state transition equation and λ is the so-called co-state variable. This co-state variable has to satisfy a dynamic equation defined in the maximum principle [163].

By substituting Eq. (6-1b) for system state transition equation in Eq. (6-3), the Hamiltonian function can be transformed to:

$$H = \dot{m}_f + \left(-\frac{\lambda}{V_b(x)\cdot Q_{max}}\right) \cdot P_b. \tag{6-4}$$

If the term $-\frac{\lambda}{V_b(x)\cdot Q_{max}}$ is replaced by the equivalence factor s, the Hamiltonian function can be considered as a new criterion:

$$J = \dot{m}_{equiv} = \dot{m}_f + s \cdot P_b. \tag{6-1h}$$

This new criterion is so-called the equivalent consumption [130]. It is the instantaneous cost function used in the ECMS optimization. Actually, the second term on the right of the equation is taken as the virtual fuel consumption rate of electric energy [138].

From above deducing, it is obvious that the co-state of Hamiltonian function, to some extent, represents the equivalence between the fuel and electric energy usage. If the equivalence factor has to be evaluated from the co-state, ECMS will lose the advantage when compared with the maximum principle. The following text will present how to estimate the equivalence factor based on its physical meaning; while, the relationship between co-state λ and equivalence factor s will be demonstrated in Section 6.5.

6.1.2 Equivalence Factor

The equivalence factor represents the core of ECMS. This parameter influences the system behaviour as follows: if it is relatively large, the use of electrical energy tends to be penalized and the fuel consumption increases; if, on the contrary, it is relatively small, the use of electrical energy is overly favoured and the battery SoC decreases [164]. Since the equivalence factor represents the conversion ratio between two energies, it can be estimated using SFC [136]. Meanwhile, the overall efficiency of the electric path is also reflected. Given that the efficiencies of the electric path must be included, the equivalence factor can be expressed as:

$$s = \begin{cases} SFC \cdot \eta_{MG}^{-1} \cdot \eta_{batt.c}^{-1}, & P_b > 0 \\ SFC \cdot \eta_{MG} \cdot \eta_{batt,d}, & P_b < 0 \end{cases}, \qquad \textbf{(6-5)}$$

where η_{MG} is the efficiency of motor/generator. $\eta_{batt,c}$ and $\eta_{batt,d}$ are battery charging/discharging efficiency, respectively. The efficiency of the converter is not considered. Note that the equivalence factor defined in this thesis is not dimensionless, since P_b instead of a virtual electric fuel cost $\dot{m}_e$ is introduced in the cost function. The SFC is given by Figure 4-2 and motor/generator efficiency map is shown in Figure 4-4. Note the generator mode shares the same efficiency map as the motor mode, only the torque becoming negative.

The idea of equivalent consumption was initially established based on the charge-sustaining strategy, in which the battery is considered as an energy buffer with no net usage of electricity [138]. If the battery energy flow is taken into account as an 'additional' fuel used, the ECMS can also be applied to other charging strategies (e.g. maintaining the SoC within a range).

6.2 Fuzzy Logic Control

As illustrated in Section 2.3.2.2, the conventional ECMS cannot maintain the desired constraints on battery SoC. Therefore, a fuzzy logic controller is designed to regulate the optimal control of ECMS according to the instantaneous value of the SoC.

A fuzzy logic controller generally consists of the rule-base, fuzzification interface, inference mechanism, and defuzzification interface (see Figure 6-1). The rule-base

collects a series of linguistic rules that describe available expert knowledge and experience on how to control the system. On the fuzzification interface, the numeric inputs of the controller are converted into the linguistic inputs. Then, using the linguistic inputs and established rule-base, the inference mechanism mimics the expert's knowledge and determines the linguistic control decisions (linguistic outputs). Lastly, defuzzification is performed to convert the linguistic controls into actual control values (outputs of the fuzzy controller).

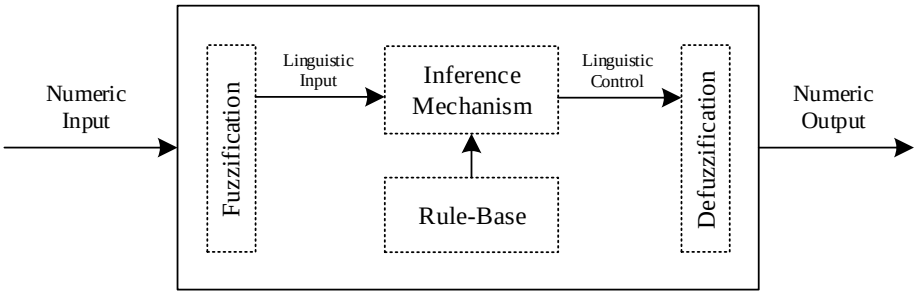

Figure 6-1 Fuzzy controller [165]

6.2.1 Fuzzy Sets

In this study, the fuzzy controller has four input variables: the power requirement P_{req}, the maximum engine power $P_{ICE,max}$, the optimal engine power $P_{ICE,opt}$ and the SoC. The output of the fuzzy controller is the motor/generator power P_{MG}. Using the power requirement, the maximum power and optimal power of the engine can be substituted by their difference. Thus, hereafter, the original inputs are replaced by $u_1 = P_{req} - P_{ICE,max}$, $u_2 = P_{req} - P_{ICE,opt}$, and $u_3 = SoC$. The output of fuzzy controller is denoted by $y = P_{MG}$. To simplify the illustration, the linguistic variables (inputs and outputs) are also described by symbols, $P_{req} - P_{ICE,max}$, $P_{req} - P_{ICE,opt}$, SoC and P_{MG}, instead of the lengthy linguistic terms.

The fuzzy set, A_i, and its associated Membership Function (MF), $\mu_{A_i}(u_i)$, can describe the degree of certainty that the input, u_i, possesses the property characterized by its linguistic value, $\tilde{A}_i$ [165]:

$$A_i = \{(u_i, \mu_{A_i}(u_i)) : u_i \in U_i\}, \quad \textbf{(6-6)}$$

where U_i is the universe of discourse for u_i. In other word, the MF associated with A_i and $\tilde{A}_i$ can map the U_i to [0, 1]. Note that generally there are more than one MF for one input. Therefore, the fuzzy set and its associated MFs are symbolized by A_i^j and $\mu_{A_i^j}(u_i)$, where $A_i^j \in A_i$.

In this study, a functional fuzzy system (T-S fuzzy system) is introduced as the basis of the controller. In the same manner as a traditional fuzzy system, the T-S fuzzy system describes the inputs by fuzzy sets. However, its control values are determined by the function with input variables as arguments. The MFs of three new inputs are shown in Figure 6-2.

With the substitution of input variables, the number of inputs is reduced to three. In addition, fewer MFs are required to cover the range of $P_{req} - P_{ICE,max}$ and $P_{req} - P_{ICE,opt}$, since only two linguistic values ('neg' and 'pos') are needed. The domain of $P_{req} - P_{ICE,max}$ and $P_{req} - P_{ICE,opt}$ is (-40, 40) kW and (-50, 50) kW, respectively.

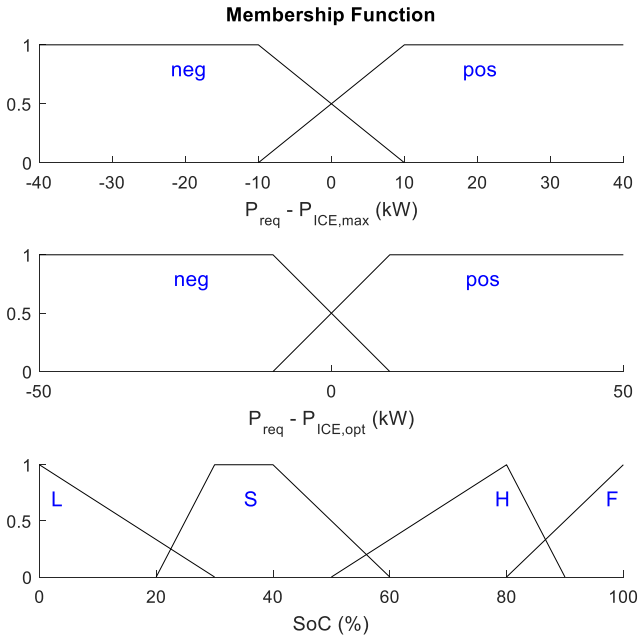

Figure 6-2 Membership Functions

Concerning the SoC, four linguistic terms are defined to represent values of SoC, i.e. 'L', 'S', 'H' and 'F'. The 'L' is where the SoC is low and the battery charge is requested if the extra engine power is available. The 'S', denoting 'sustaining', is the most important criterion. When the degree of this membership reaches 1, the corresponding

numeric value of SoC is the ideal sustainable value. The 'H' implies that the SoC is high and the battery charge is not compulsory, unless the power demand is lower than the optimal engine power. The full SoC is indicated by the 'F', where the battery charge is not permitted.

It can be concluded from Figure 5-7 that the battery voltage will decrease sharply when the SoC is under 20%. Hence, the zero degree of 'L' is set at slight above 20% SoC. On the other hand, (30%, 40%) is selected as the ideal SoC range, because the remaining electrical energy (30%, 40%) can guarantee a safe landing if the engine fails. The advantage of combining the motor power can be obtained by classifying the range for fuzzy set 'H' as (50%, 90%).

6.2.2 If-Then Rules

The rule-base of fuzzy controller consists of a series of linguistic rules. The general form of the linguistic rules is as follows [165]:

If premise, **then** consequent.

Therefore, the linguistic rule is normally called If-Then rules. The premise is associated with the input and is on the left-hand side of the If-Then rule. The consequent is associated with the control and is on the right-hand side of the If-Then rule. The controls are inferred from the premise and consequent of linguistic If-Then rules.

As mentioned in Section 6.2.1, the T-S fuzzy system is applied in this study. Therefore, the premises of the If-Then rules are represented by fuzzy sets with the associated MFs, while the consequents are approximated using linear functions:

1) If $P_{req} - P_{ICE,max}$ is **pos** and SoC is **H** or SoC is **F**, then $P_{MG} = P_{req} - P_{ICE,opt}$;
2) If $P_{req} - P_{ICE,max}$ is **pos** and SoC is **S**, then $P_{MG} = P_{req} - P_{ICE,max}$;
3) If $P_{req} - P_{ICE,opt}$ is **neg** and SoC is **F**, then $P_{MG} = 0$;
4) If $P_{req} - P_{ICE,opt}$ is **neg** and SoC is **not F**, then $P_{MG} = P_{req} - P_{ICE,opt}$;
5) If $P_{req} - P_{ICE,max}$ is **neg** and $P_{req} - P_{ICE,opt}$ is **pos** and SoC is **H** or SoC is **F**, then $P_{MG} = P_{req} - P_{ICE,opt}$;
6) If $P_{req} - P_{ICE,max}$ is **neg** and $P_{req} - P_{ICE,opt}$ is **pos** and SoC is **L** or SoC is **S**, then $P_{MG} = P_{req} - P_{ICE,max}$;

7) If SoC is **L**, then $P_{MG} = f(SoC)$.

As shown in Rules 1) and 2), if the power demand is above the ICE maximum power, the positive motor/generator power decreases when the SoC drops from 'H' level to the 'S' level. On the other hand, when the power demand is lower than the ICE optimal power, the battery charge will be activated and continue until the SoC is near its maximum capacity (see Rules 3)-4)). The third scenario is that the power demand is between the ICE optimal and maximum power, see Rule 5)-6). If the SoC is high enough ('H' or 'F'), the controller demands the positive power from the motor/generator, to enable the ICE to operate at its optimal condition. Otherwise, the motor/generator acts as a generator to restore the electrical energy in the battery, using the extra available power of the engine. It should be noted that if the SoC is very low, without compromising the safety of aircraft, charging the battery has the priority over meeting higher power demand (see Rule 7)). This is to prevent permanent damage to the battery and guarantee enough electrical energy in case of engine failure. Rule 7) also illustrates that charging power increases at lower values of SoC.

6.2.3 (De-)fuzzification and Inference

On the basis of designed fuzzy sets and If-Then rules, the fuzzification, inference and defuzzification can be employed in sequence to deduce the final control output. In the fuzzification process, actual inputs are transformed to fuzzy sets. Note that the singleton fuzzification (generally used in the T-S system) is not applied in this study, since it is sensitive to measurement noise.

The inference mechanism has two basic tasks: the first one is called matching, determining the extent to which each rule is relevant to the current system state; secondly, the inference step draws the conclusions using the inputs and the relevant rules.

The inference involves resulting in the membership value combing the fuzzy sets in premises of rules and fuzzification: $\mu_{\hat{A}_i^j}(u_i) = \mu_{A_i^j}(u_i) * \mu_{\hat{A}_i^{u_i}}(u_i)$. Then, the membership value μ_i for the i^{th} rule's premise can be formed as:

$$\mu_i = \mu_{\hat{A}_1^j}(u_1) * \mu_{\hat{A}_2^k}(u_2) * \mu_{\hat{A}_3^l}(u_3), \quad \textbf{(6-7)}$$

where $*$ denotes fuzzy intersection. The parameters j, k, l represent all possible j, k, l MFs for three input variables.

In the defuzzification process, the linear functions β_i are given by the consequents of If-Then rules in Section 6.2.2. Therefore, the defuzzification is expressed as:

$$y = \frac{\sum_{i=1}^{R} \beta_i \mu_i}{\sum_{i=1}^{R} \mu_i}, \quad \textbf{(6-8)}$$

where y is the numeric output of the fuzzy controller. It is assumed that the functional fuzzy system is well defined so that $\sum_{i=1}^{R} \mu_i \neq 0$ for all possible inputs.

6.3 Fuzzy Based Optimization

With the combination of ECMS and FLC, the supervisory control can achieve the optimal hybrid of fuel and electrical energy, and also keep the battery SoC in the desirable range. The variable exchanges between the ECMS and FLC are highlighted in Figure 6-3. The ECMS requests the instantaneous value of power requirement P_{req} and SoC to optimize the engine power. The optimal engine power from the ECMS is sent to the FLC, in addition to the maximum engine power, $P_{ICE,max}$. The FLC still needs the power demand, P_{req} and SoC to give the outputs of the supervisory controller.

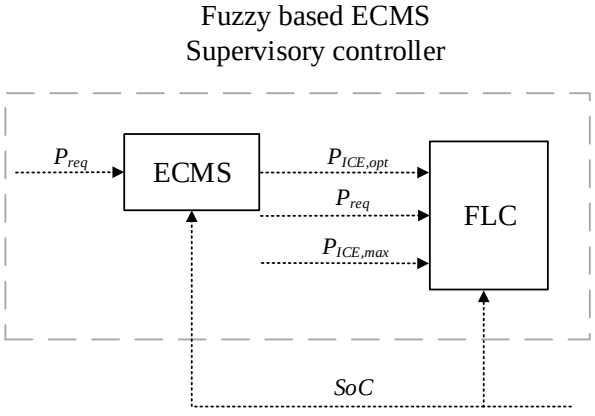

Figure 6-3 Combined supervisory controller

6.4 Numerical Examples

This section reports the validation of the FLC based ECMS, also using hypothetical flight test scenarios given in Section 5.1.4. As the same as the Section 5.4, since the first test case is taken as a priori-known flight mission, DP can also be implemented; on the other hand, the second mission is assumed as impromptu and unpredictable in this section, which can only be optimized by our FLC based ECMS, the original ECMS and A-ECMS.

6.4.1 Fuzzy Based Optimization

This section validates the results of FLC based ECMS, using test scenario 1. This test case simulates a complete 30 minutes flight mission that includes take-off, climbing, cruising and landing phases. The details of this hypothetical mission are given in Section 5.1.4. Regarding the SoC-regulating strategy, the initial value of battery SoC is set to 50%. The maximum and minimum value of SoC are 80% and 20%, respectively, considering the operating range of the battery. The SoC is sustained according to the designed fuzzy rules.

Figure 6-4 gives the simulation results of FLC based ECMS, including the engine and motor/generator power, in addition to battery SoC. At the beginning of the mission, the battery SoC is 50% that falls into the fuzzy set ‘S’. According to the If-Then rules 6), the battery should be charged if the engine has extra available power. It is clear in Figure 6-4 that the motor/generator absorbs power from the engine during this process (before 1st minute).

Regarding the take-off and climbing phase, between 1st and 6th minute, the power demand exceeds the maximum engine power. Therefore, the motor/generator should output positive power to facilitate climbing. Since the battery SoC at this moment is both in ‘S’ and ‘H’ sets, the controller requests nearly maximum power from the motor, as shown in Figure 6-4.

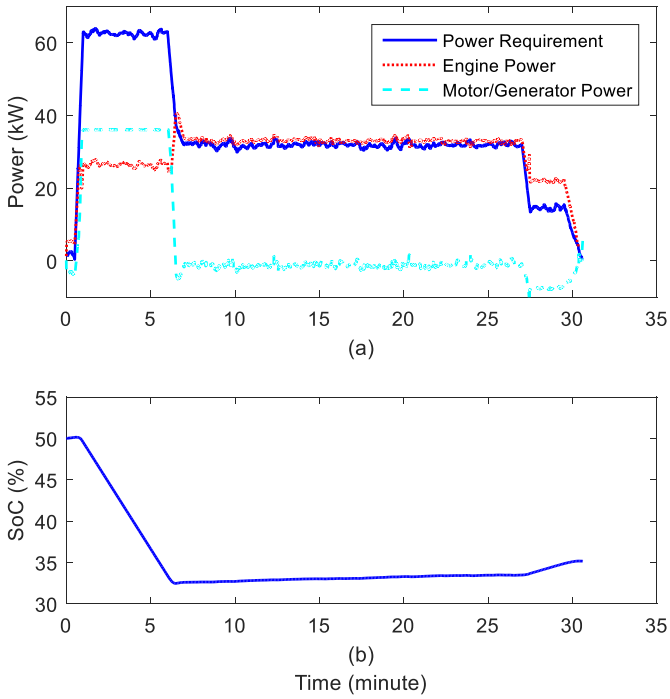

Figure 6-4 Simulation results of FLC based ECMS (1)

After the climbing phase, the battery SoC decreases to between 30% and 40%, which is the sustaining range according to the designed fuzzy sets. Consequently, the output of the motor/generator reduces under zero during the whole cruising part. In this process, the engine not only provides all the power that the propeller needs, but also delivers some power to sustain the battery SoC based on fuzzy rules. When the landing phase starts, the battery SoC recovers by a small margin since the engine has more extra available power. This charging process is in accordance with the rule 4) or 6) in Section 6.2.2.

Figure 6-5 and Figure 6-6 give simulation results of other variables, such as speed, torque, current and voltage. It is seen from Figure 6-5 (a) that the engine and motor/generator speed fluctuate a little during the cruising. This reflects that the instantaneous (on-line) control algorithm is more vulnerable to the variation of mission requirement, compared with the off-line control method. The torque values in Figure 6-5 (b) also indicates the battery charge at the initial, cruising and final part of the mission.

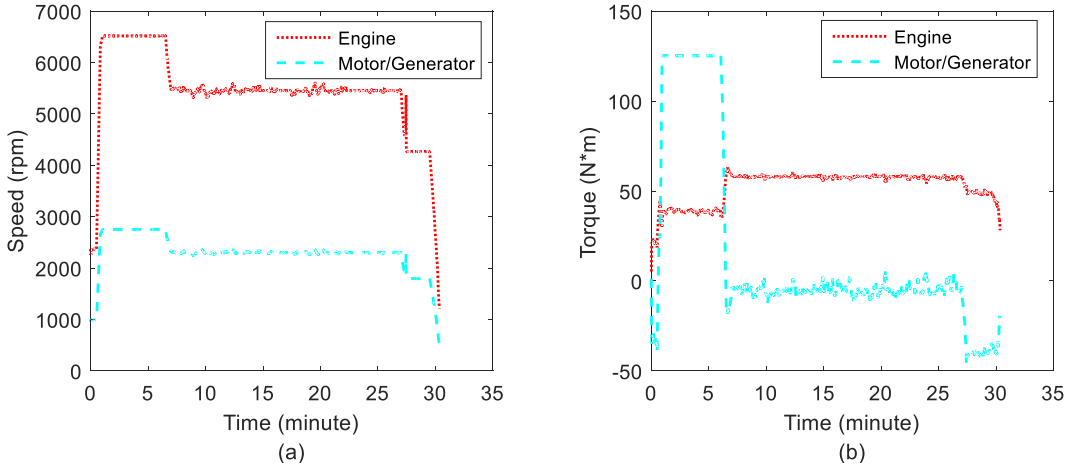

Figure 6-5 Simulation results of FLC based ECMS (2)

As shown in Figure 6-6, the output current and voltage of the DC/DC converter are compared with ones of the battery, which is equal to the input current and voltage of the DC/DC converter. The output voltage of the DC/DC converter is also stabilized to 300 V, which is higher than the voltage of the battery. The absolute value of output current of the battery is also not lower than one of the DC/DC converter. The voltage of the battery decreases to roughly 271 V when the discharging current is high between 1st and 6th minute. Then it recovers and stables around 279 V since the output current of those two electric devices varies around zero. The charging current rises to 20 A for the landing phase, with a small margin of growth of battery voltage. The current falls back to zero at the end of the flight mission.

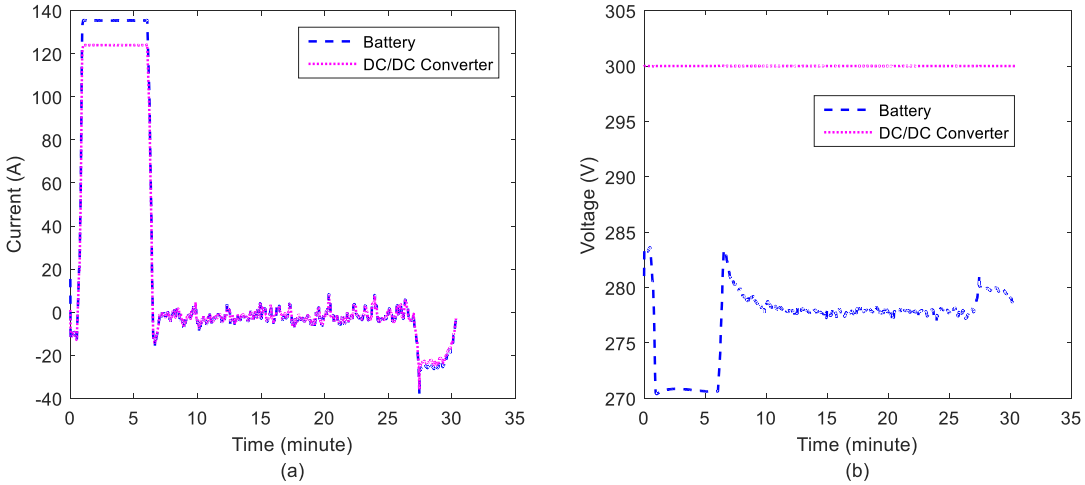

Figure 6-6 Simulation results of FLC based ECMS (3)

In sum, the proposed fuzzy based optimization can sustain the battery SoC between 30% and 40%, at the same time satisfying power requirement. With the implementation of disturbed power demand, the control algorithm is also verified to be robust to the disturbance.

6.4.2 Comparison

In the previous section, the FLC based ECMS is validated to have the good performance, but the optimality of its result has not been discussed. Therefore, the results of FLC based ECMS are compared with ones of DP, since DP can guarantee the global optimality of its solutions. On the other hand, the on-line performance of FLC based ECMS is compared with another two instantaneous optimizations—ECMS and A-ECMS.

6.4.2.1 Test Case 1

According to the If-Then rules, the battery SoC should be sustained between (30%, 40%). Thus, the final state of SoC is set as 35% for DP. The initial state is equal to one in the previous section, i.e. 50%. The maximum and minimum value are also 80% and 20%, respectively.

Table 6-1 lists the information on the final SoC and the fuel/energy usage from two optimizations. It is obvious that two approaches can ensure that the final value of battery SoC is between 30% and 40%, while the certain error exists between the final value from DP and the desired value. Similar to Table 5-1, the true fuel consumption of two optimizations is acquired using SoC correction.

Table 6-1 Comparison of optimization results between FLC based ECMS and dynamic programming

	Fuzzy based ECMS	Dynamic Programming
Final SoC (%)	35.14	33.68
Fuel Consumption (kg)	5.65	5.41
Corrected Final SoC (%)	35	35
Corrected Fuel Consumption (kg)	5.64	5.42
Energy Consumption (kW*h)	72.7	70.0

The corrected SoC and fuel usage are also displayed in Table 6-1. The corrected figures demonstrate that the FLC based ECMS can achieve sub-optimal results, though the fuzzy-based rules are applied to adjust optimal results from ECMS. The error between the fuel usage of FLC based ECMS and the optimal one of DP is 4%. The error between the energy consumption of the two methods is less than 4%.

Figure 6-7 provides the details of battery SoC and fuel used for DP and FLC based ECMS. Note that FLC based ECMS is labelled as F-ECMS in the figure. At the first step of the mission, before the 1st minute, two optimizations act the similar way. When the take-off and climbing phase start, the FLC based ECMS requests more electrical energy than the DP, resulting in lower SoC and fuel consumption compared to ones of DP. At the end of climbing, since the SoC of FLC based ECMS declines to about 31%, a charging process is activated to sustain the SoC during the cruising. Therefore, the fuel usage of FLC based ECMS rises quickly than one of DP after the 6th minute. It outnumbers the fuel usage of DP around 20th minute. The charging process lasts until the end of the mission, since high power demand does not occur. With the continuous charge, the SoC of FLC based ECMS recovers to 35.14% finally.

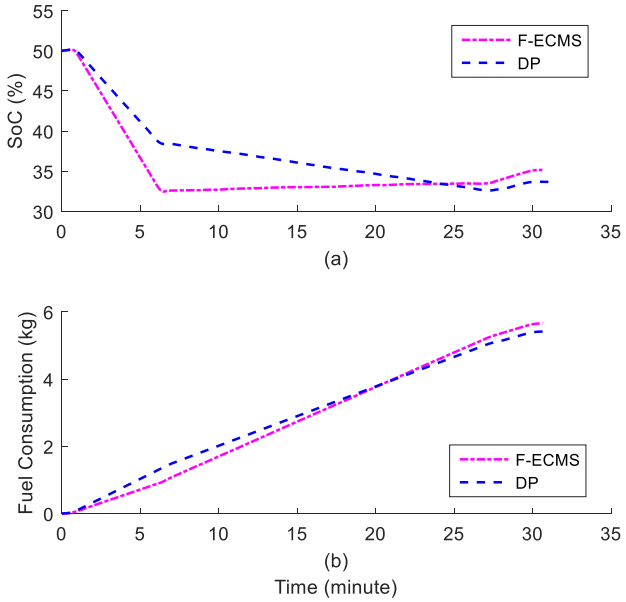

Figure 6-7 Comparison of simulation results between FLC based ECMS and dynamic programming (1)

On the other hand, after the first minute, the DP has been requesting the positive power from the electric powertrain until the landing phase. Consequently, the time

length of the battery charge for DP is much less than one for the FLC based ECMS. This means that the DP saves many energy losses caused by converting the combustion energy to the electrical one. Therefore, it consumes less fuel compared with the FLC based ECMS. However, this optimal result is on the basis of the prior-known knowledge of future mission. As a causal optimization, the FLC based ECMS selects the best solution only based on the past and current information, thereby leading to the sub-optimal results.

The engine and motor/generator power shown in Figure 6-8 give an insight into the power distribution of two methods. When the aircraft requests the high power to take-off and climb, the DP draws more power from the engine while the FLC based ECMS uses more electric power. This directly leads to the battery charge during the cruising phase for the FLC based ECMS, but the battery in DP still has a few energy to facilitate the propeller driven.

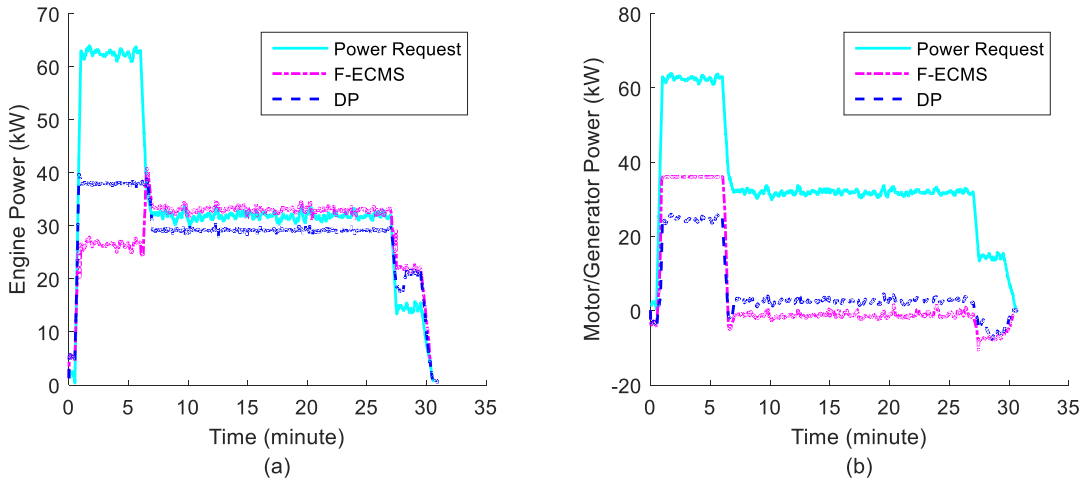

Figure 6-8 Comparison of simulation results between FLC based ECMS and dynamic programming (2)

In short, the FLC based ECMS succeeds in converting the non-causal energy optimization into an equivalent causal energy optimization, with little sacrifice of the optimality of the solution. Moreover, the prior-knowledge of flight mission is not pre-requisite and the FLC based ECMS can achieve the sub-optimal control for on-line implementation.

6.4.2.2 Test Case 2

Different from the test case 1, the second one emphasizes on analysis of the capability of SoC sustaining and computational cost of different instantaneous optimization algorithms. Since the sustaining range of fuzzy rules is (30%, 40%), the initial SoC in this test is set as 35%. The maximum and minimum value are also 80% and 20%, respectively. The flight mission used in this section is the second test scenario, and its power requirement is given in Figure 5-6.

In addition to the FLC based ECMS, the original ECMS and A-ECMS are also studied and validated in this test case. It is well-known that the original ECMS cannot sustain the battery SoC if its equivalence factor is not optimized for the test mission profile [132,133]. To enable the comparison between three ECMS based optimizations, the optimal equivalence factor of the original ECMS in this test case is estimated off-line using the cost-to-go from DP [128]. On the other hand, the equivalence factor of A-ECMS is updated on-line using a PI controller. The formulation of this PI controller is illustrated in the following Section 6.5.3.

Figure 6-9 presents the battery SoC, fuel usage and computation time of optimization of ECMS, A-ECMS and FLC based ECMS. The results of FLC based ECMS is labelled by F-ECMS. As shown in Figure 6-9 (a), the FLC based ECMS succeeds in sustaining the SoC between 30% and 40%, following the objective of designed fuzzy rules. On the other hand, both the A-ECMS and ECMS can sustain the battery SoC around the pre-set value (35%). However, the ECMS shows poorer performance than the A-ECMS, though it applies the optimal equivalence factor estimated off-line. This demonstrates that even though the mission profile is priori-known and the corresponding equivalence factor is optimized, the ECMS still cannot achieve precise sustaining if there is a disturbance in the mission profile.

The computation time of optimization of ECMS, A-ECMS, and FLC based ECMS are plotted in Figure 6-9 (b). It indicates that these three instantaneous optimizations are all eligible for implementing on the real-time application, since their optimization time are all less than 0.01 sec. Among three algorithms, the A-ECMS has the largest computational burden, since it needs to update the equivalence factor on-line. The computational cost of FLC based ECMS is not much higher than the benchmark one (the original ECMS).

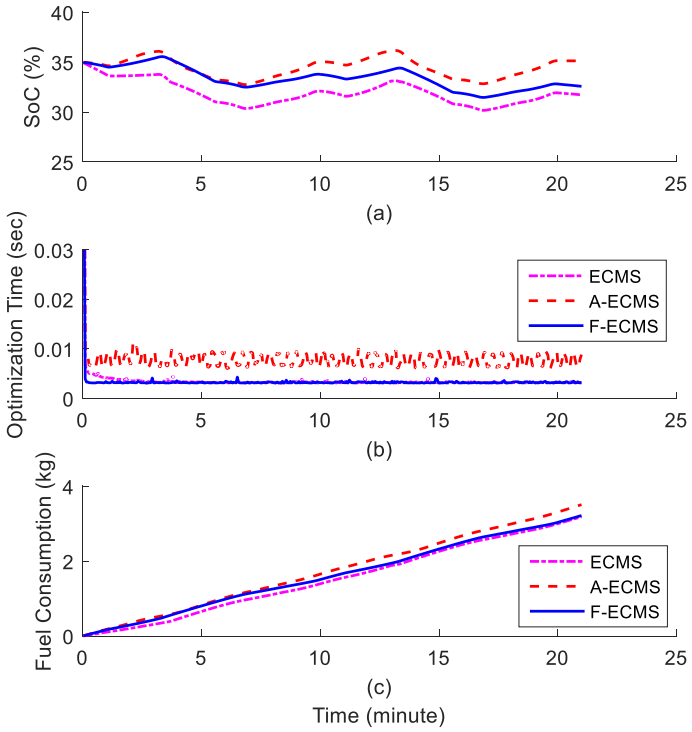

Figure 6-9 Comparison of simulation results between ECMS, A-ECMS, and FLC based ECMS

Table 6-2 lists the details of final values of SoC and fuel consumption, in addition to their corrected values. The corrected (true) fuel usages demonstrate that the original ECMS consumes the least fuel (3.21 kg) among three approaches. The reason may be that its equivalence factor is estimated from the non-causal optimization—DP. On the other hand, the FLC based ECMS can save around 7% fuel usage, compared with the A-ECMS. The fuel cost of the FLC based ECMS (3.23 kg) is not much higher than one of the original ECMS.

Table 6-2 Comparison of optimization results between ECMS, A-ECMS and FLC based ECMS

	ECMS	A-ECMS	F-ECMS
Final SoC (%)	31.72	35.11	33.67
Fuel Consumption (kg)	3.19	3.51	3.22
Corrected Final SoC (%)	35	35	35
Corrected Fuel Consumption (kg)	3.20	3.51	3.23

Energy Consumption (kW*h)	41.7	45.2	41.9
Average Optimization Time (sec)	0.0033	0.0089	0.0034
Need for Off-line Optimization of Equivalence Factor	Yes	No	No

The average computation time of optimization is also given in Table 6-2. It is shown that the average optimization time of the A-ECMS is nearly three times higher than another two instantaneous methods. However, the combination of fuzzy control and ECMS does not increase much of the computational cost of the original ECMS. Furthermore, the FLC based ECMS can be applied on-line directly while the original ECMS requests the off-line optimization of the equivalence factor.

In sum, the FLC based ECMS overcomes the deficiency of the original ECMS, by integrating fuzzy logic controller. Similar to the A-ECMS, it can realize the on-line charge-sustaining with no need for off-line estimation of equivalence factor. Moreover, the FLC based ECMS outperforms the A-ECMS, concerning the less computing time and less fuel consumption.

Besides the profits revealed by the test cases and comparisons, some further advantages are worth to be mentioned: It is well-known that the performance of A-ECMS is sensitive to mission profiles, since the PI controller or penalty function may be required to be regulated for each mission. Following the designed fuzzy rules, the fuzzy controller won’t be up against this issue.

6.5 Pontryagin’s Maximum Principle

As mentioned in Section 6.1, the equivalence factor of ECMS is related to the co-state variable of Hamiltonian function. This section aims to solve the energy management problem by the PMP and then verify the relationship between the co-state variable and the equivalence factor.

6.5.1 Problem Formulation

The minimum (or maximum) principle of optimal control gives the fundamental necessary conditions for a controlled trajectory, generally described with (x, u), to be optimal [163]. Though only a necessary condition for the original non-causal problem, PMP is still worth researching since it can transform the original problem to the causal one.

As given in Section 6.1.1, the Hamiltonian function of fuel minimization problem for hybrid propulsion system consists of two parts:

$$H(x, u, t) = \dot{m}_f(u) + \lambda(t) \cdot f(x, u). \quad \textbf{(6-9)}$$

The first term in the Hamiltonian is the instantaneous fuel usage, which is the integrand of the original objective; while the second term is the co-state variable multiplied by the system state transition function.

The PMP states that the necessary conditions (equations (6-10)-(6-12)) must be satisfied, if $u^*(t)$ is the optimal control of the original problem. Eq. (6-10) indicates that $u^*(t)$ can minimize the Hamiltonian function at each instant; and Eqs. (6-11) and (6-12) give transition equations of the co-state variable and system state variable, respectively.

$$H(x(t), u(t), t) \geq H(x(t), u^*(t), t), \quad \forall u(t) \neq u^*(t) \quad \textbf{(6-10)}$$

$$\dot{\lambda}(t) = -\frac{\partial H}{\partial x} = -\lambda \cdot \frac{\partial f(x,u)}{\partial x}, \quad \textbf{(6-11)}$$

$$\dot{x}(t) = \frac{\partial H}{\partial \lambda} = f(x, u). \quad \textbf{(6-12)}$$

In consequence, the original non-causal problem can be resolved theoretically by finding the optimal control to minimize the Hamiltonian function at any instant of time. Generally, the initial value of co-state needs to be set previously; then the value at the next step can be updated with the state transition equation.

6.5.2 Piecewise Linear Approximation of Hamiltonian function

Though the PMP has converted the non-causal optimization into an instantaneous one, the real-time application is still a challenge due to the nonlinearity of the Hamiltonian function, which comprises the engine fuel rate and SoC rate multiplied by the co-state. Here, the fuel rate is fitted with the piecewise linear approximation as the same as in convex optimization.

The SoC rate is also approximated with the piecewise linear function, though with the motor/generator torque as the self-dependent variable (see Figure 6-10). The motor/generator torque is selected since it is more relevant to the battery power. The turning point of all ΔSoC curves is the zero torque point, due to the opposite power flow directions. As a result of the directional reverse, for the same absolute output motor power, a negative torque will cause a smaller absolute value of ΔSoC than a positive torque. This phenomenon has been retained by the piecewise linear approximation, as shown in Figure 6-10.

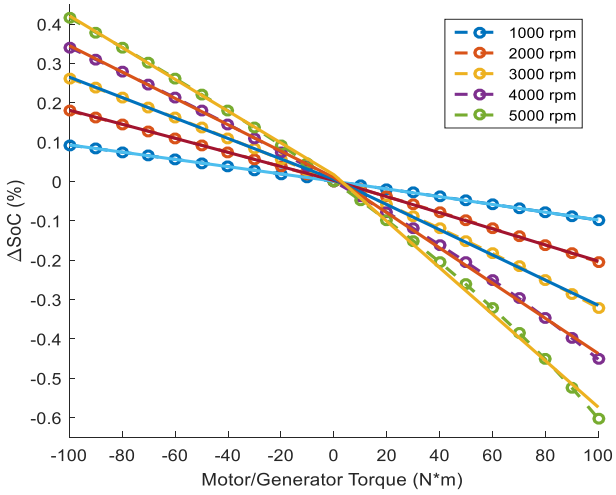

Figure 6-10 Piecewise linear approximation of the SoC rate

6.5.3 Equivalence Factor

This section validates the PMP based energy optimization using the first hypothetical flight test scenario given in Section 5.1.4. Furthermore, the co-state variable of PMP is

transferred and compared with the equivalence factor of A-ECMS. The initial value of co-state variable and equivalence factor are both estimated by the cost-to-go of DP.

The initial value of SoC is set to 60%. The maximum and minimum value of SoC are 80% and 20%, respectively, considering the operating range of the battery. The SoC is allowed to be depleted to 30%, then the energy management is demanded to sustain the SoC around this value.

The A-ECMS updates the equivalence factor $s(t)$ by a PI controller to regulate the current SoC (i.e. $x(t)$) to the target value x_{sus}:

$$s(t) = s_0 + K_P(x(t) - x_{sus}) + K_I \int (x(\tau) - x_{sus})d\tau. \quad \textbf{(6-13)}$$

Here, the s_0 is the initial value of equivalence factor, whereas K_P and K_I are gains of PI controller. Likewise, the Hamiltonian function takes the SoC into consideration using the state transition equation.

Figure 6-11 compares the optimization time and equivalence factor between the PMP and A-ECMS. In terms of the computational cost, the A-ECMS has less optimization time than PMP. The reason may be that the PMP is needed to update the co-state in each step. Yet this does not influence its capability of the on-line application.

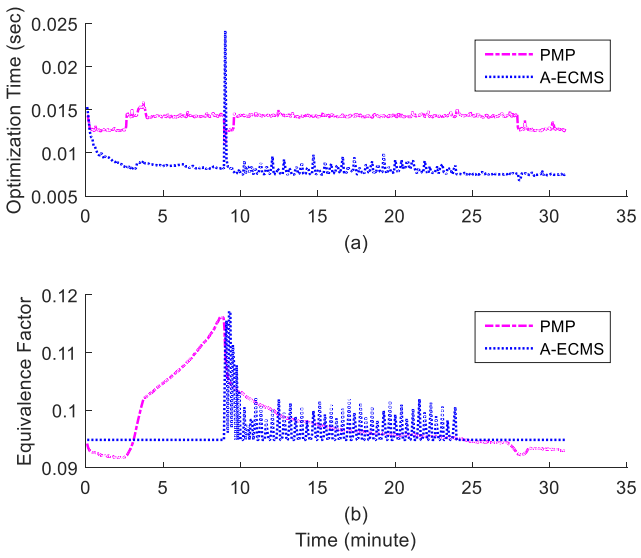

Figure 6-11 Comparison of optimization variables between PMP and A-ECMS

The equivalence factor is a significant parameter of A-ECMS optimization, since the performance of A-ECMS methods is heavily dependent on its precise estimation. The equivalence factor of PMP is defined and calculated by $s(t) = -\frac{\lambda(t)}{V_b(t) \cdot Q_{max}}$. Two equivalence factor are shown in Figure 6-11 (b). The equivalence factor of PMP is clearly comparable to one of A-ECMS. Furthermore, the equivalence factor of PMP increases gradually and reaches a similar value as A-ECMS around the 10th minute. This avoids the sharp up and down of equivalence factor, leading to a gently varying of optimal control.

6.6 Conclusions

This chapter proposed a causal optimization—the fuzzy based equivalent consumption optimization, to manage the energy distribution of hybrid propulsion system.

The original non-causal fuel minimization problem was first converted into a causal one. The main difference between the original non-causal problem formulation and its corresponding causal one is the objective function. The causal problem formulation replaced the non-causal criterion by an instantaneous one, by introducing the Hamiltonian function. The Hamiltonian function was processed and converted to the new instantaneous cost, which is named by equivalent consumption. Furthermore, the co-state variable of Hamiltonian function was related to the equivalence factor of equivalent consumption.

The causal optimization—ECMS can optimize the equivalent consumption but not guarantee the sustaining of battery SoC, if the equivalence factor is not optimized based on the mission profile. To overcome this issue, this study extended the ECMS with a fuzzy control. The fuzzy rules can maintain the battery SoC in a desirable range, since it can favour the electric power if the SoC is too high while request the battery charge if the SoC is too low. The so-called ‘sustaining’ range of SoC is determined by the membership functions of fuzzy control. It is worth mentioning that for the FLC, the T-S fuzzy system was selected and the number of MFs was also reduced by reconsidering inputs of FLC. Those approaches reduce the complexity of the fuzzy system and the computation of (de-)fuzzification.

The proposed FLC based ECMS was validated using hypothetical flight scenarios defined in Chapter 5. Its optimality and advantages were demonstrated by the

comparison with DP, ECMS and A-ECMS. The first test scenario compared the results of one non-causal optimization—DP with our FLC based ECMS algorithm. The test validates that the FLC based ECMS succeeds in converting the non-causal energy optimization into an equivalent causal energy optimization, with little sacrifice of the optimality of the solution. In other words, the prior-knowledge of flight mission is not pre-requisite and the FLC based ECMS can achieve the sub-optimal control for on-line implementation.

Another two causal optimizations: the original ECMS and A-ECMS, were also studied in the second test case. Their results were compared with one of the FLC based ECMS. The FLC based ECMS overcomes the deficiency of the original ECMS, since it can realize the on-line charge-sustaining with no need for off-line estimation of equivalence factor. Moreover, the FLC based ECMS outperforms the A-ECMS, since it can reduce the computation time of optimization and save more fuel.

The PMP was applied to solve the energy management problem. The piecewise linear approximation was employed to simplify the Hamiltonian function. The test results demonstrate that the relationship between the equivalence factor of ECMS and the co-state variable of Hamiltonian function can be represented by the equation provided in this chapter.

7 Combined Energy Management

The convex optimization and fuzzy based optimization has been proposed and validated in Chapter 5 and Chapter 6. The convex optimization can save more fuel usage even compared with the most popular non-causal optimization—DP. Furthermore, it reduces the computation time of optimization to less than 1 sec. However, the convex optimization still cannot be applied when the mission profile is not priori-known. Therefore, the FLC based ECMS is also studied in this thesis, since it only requires the current or past system information. The deficiency of all causal optimizations is that it can only achieve sub-optimal results. Moreover, the control trajectory cannot lead the system to a pre-defined state since the future information is not considered in the algorithm.

This chapter will combine the convex optimization and fuzzy based optimization to complete a flight mission with several sub-tasks. If the profile of sub-task is not accessible before the flight, the FLC based ECMS needs to be adopted to update control variables on-line. If a specific sub-task is demanded for the part of the future flight, the convex optimization is preferred to achieve the optimal results, since all information about this sub-task is previously known.

7.1 Flight Mission

The flight mission illustrated in this chapter is called the test case 3. It also includes take-off, climbing, cruising and landing phases. Besides, the Combined Mode, Charge Mode and EM-Only Mode are all verified in the test scenario. When both the engine and motor output positive power to drive the propeller, the HEPS is at Combined Mode. The Charge Mode requests the power from the engine to charge the battery, on this condition that the motor functions as the generator. If the engine fails or the aircraft enters a 'low-noise' area, the EM-Only Mode is activated. The engine will be decoupled from the drivetrain, while the motor will be only drivers to provide the propulsive power.

Similar to the flight mission given in Section 5.1.4, the power requirement P_{req} is the sum of the power requested to drive the propeller and power demanded by the auxiliary devices of the aircraft (such as payloads, power electronics and supervisory controller). Note that the power requirement takes into account of the power loss of propeller propulsion. However, different from the estimation of power demand in the system sizing, the calculation of power demand here does not need to consider the power loss due to higher altitude. The reason is that the model of engine ECU control already takes the altitude coefficient e_{air} into account.

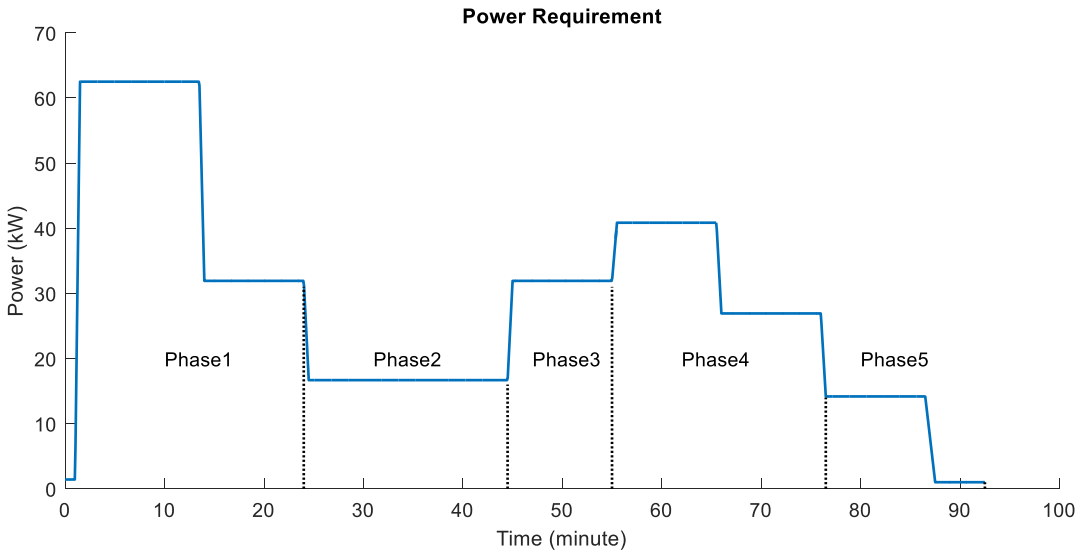

Figure 7-1 Power requirement of test case 3

The test scenario 3 simulates a complete one and half hour flight mission that includes take-off, climbing, cruising, descending and landing parts. As shown in Figure 7-1, the whole mission can be classified into five segments:

(1) Phase 1:

Phase 1 is the first stage of the aircraft flight. It contains the take-off, climbing and small segment of cruising at the optimum velocity. The system is initialized and the aircraft lifts off from the ground to the safety height in the first 2 minutes. The climbing is as follows and continues until the aircraft reaches roughly 2000 m. Climbing to this altitude costs around 10 minutes. Then, the aircraft cruises at its optimum velocity for another 10 minutes.

The FLC based ECMS is applied in Phase 1. The initial value of battery SoC is 100%. The final state of SoC is not constrained, but it has to be higher than 20%.

(2) Phase 2:

Phase 2 stays at Charge Mode and the battery SoC is required to recover to 60% at the end of the phase. Phase 2 is actually a period of transition before the aircraft starts the EM-Only Mode in Phase 3. After the take-off and climbing in Phase 1, the battery SoC may stay relatively low. Therefore, Phase 2 is set to restore the SoC before the electric-only flying. The convex optimization is used in this phase to produce the optimal energy trajectory to meet the constraints of SoC.

The aircraft is set to cruise at the range speed during Phase 2. Thus, the power demand of Phase 2 is lower than the power demand of the cruising segment of Phase 1, as shown in Figure 7-1.

(3) Phase 3:

The EM-Only Mode is activated in Phase 3, continuing on around 10 minutes. The engine is decoupled from the motor/generator. The energy management is not needed in this phase since only the motor is connected to the load.

The cruising speed increases to the optimum speed in Phase 3. The power demand rises to the corresponding value, either.

(4) Phase 4:

Phase 4 can be divided into two parts. At the first part, the aircraft climbs at a small rate of climb. This process continues on 10 minutes until the aircraft climbs by 600 m. Then it enters into the second part—descending stage, which lasts for another 10 minutes.

After roughly 10-minute electric-only flying, the battery SoC must fall into a low range at the end of Phase 3, i.e. at the beginning of Phase 4. There is no specific requirement of SoC trajectory in Phase 4. Therefore, the FLC based ECMS is employed in this phase to sustain the SoC.

(5) Phase 5:

The final segment—Phase 5 is the aircraft landing. The power requirement decreases with time. The battery SoC is requested to recover to 40% at the end of the landing phase. Convex optimization is applied to give the optimal solution.

The information about the different phases is summarized in Table 7-1. The table lists the aircraft flight phase, HEPS mode, energy optimization strategy and final SoC limitation. It is clear that two phases (Phase 1 and 4) apply the FLC based ECMS. Meanwhile, the mode and the final SoC value of these two phases are not constrained, but depends on the management of fuzzy based ECMS. On the other hand, the final value of battery SoC of Phase 2 and 5 are limited to 60% and 40%, respectively. The Charge Mode is also forced to these two phases with the implementation of convex programming. Phase 3 is different from others. It operates at EM-Only Mode and does not need the energy management strategy.

Table 7-1 Aircraft flight stage, HEPS mode, energy optimization strategy and final SoC limitation of different phases

	Flight Phase	Mode	Optimization	Final SoC
Phase 1	Take-off and Climb	-	Fuzzy based ECMS	-
Phase 2	Cruise	Charge	Convex Optimization	60%
Phase 3	Cruise	EM-Only	-	-
Phase 4	Climb and Descend	-	Fuzzy based ECMS	-
Phase 5	Land	Charge	Convex Optimization	40%

7.2 Numerical Examples

This section validates the results of hypothetical test scenario 3. This test case simulates a 1 h 30 minutes flight mission that includes take-off, climbing, cruising,

descending and landing phases. Regarding the SoC-regulating strategy, the initial value of battery SoC is set to 100%. The maximum and minimum value of SoC are 80% and 20%, respectively, considering the operating range of the battery.

Figure 7-2 (a) gives the simulation results of the engine and motor/generator power, in addition to power requirement. The corresponding SoC is also plotted in Figure 7-2 (b). As mentioned above, the FLC based ECMS is performed on Phase 1. At the initial stage of Phase 1, since the power demand is quite small, the extra engine power is available to charge the battery. However, since the battery is at full capacity, the SoC still remains at 100%. For the take-off and climbing parts, both the engine and motor produce power to drive the propeller, since the power demand exceeds both of their maximum power. The motor contributes more than the engine since the battery SoC is at 'H' and 'F' region, according to the fuzzy rules. Both the power of engine and motor decline when the power requirement falls to a cruising level after the 13th minute. The engine power only drops by a small margin (around 4 kW). The motor power reduces by over 20 kW since the battery SoC (50%) comes to the lower bound of fuzzy sets—'H', at the end of Phase 1.

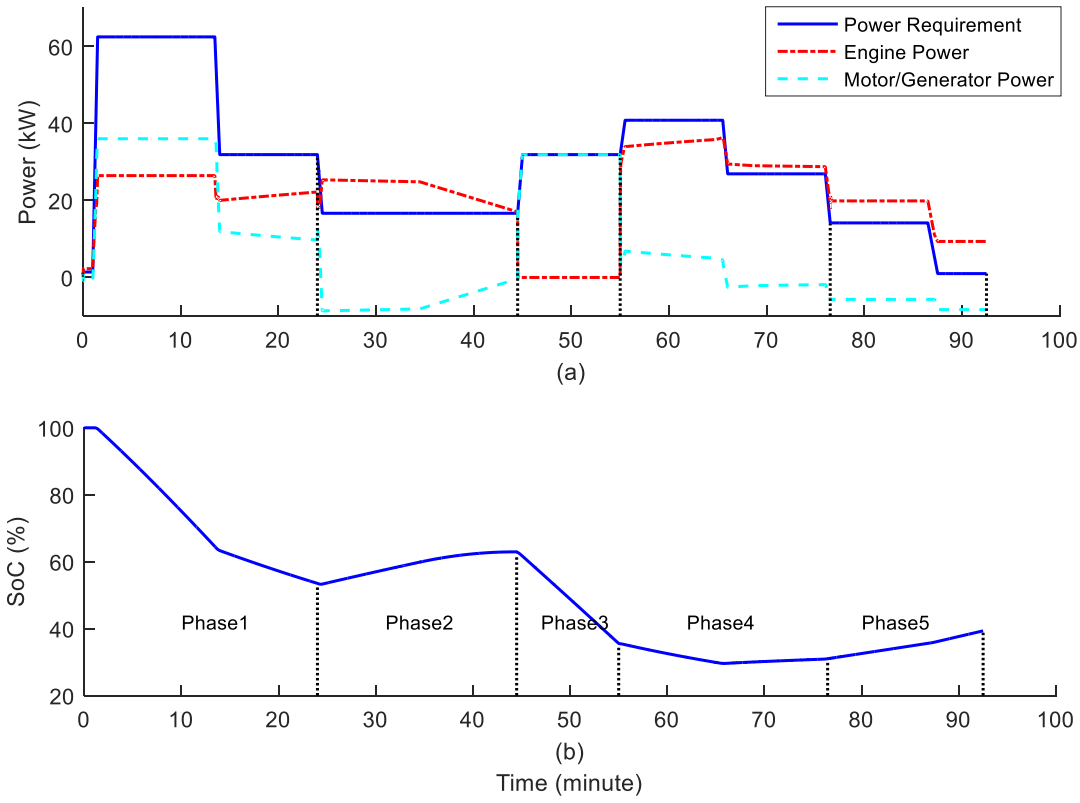

Figure 7-2 Simulation results of test case 3 (1)

The energy management approach is switched to the convex programming for Phase 2, since the sub-task of this phase is to charge the battery to restore SoC to 60%. The engine power rises to over the power demand, while the generator power drops to a negative value. The power for the battery charge is held on around 8 kW between the 24^{th} and 34^{th} minute. Its value declines to zero when the battery SoC reaches 60% at the end of Phase 2. The engine power is equal to the power requirement at the close of Phase 2.

The ten-minute electric-only flying occurs in Phase 3, with no need for energy strategy. Since the engine is decoupled from the drivetrain, the motor has the full responsibility of powering the propeller. Its output power is identical to the power requirement, while the engine has no power output. With the continuous electrical power flow drawn, the SoC of decreases to roughly 35% from 60%.

The energy management method is switched back to the FLC based ECMS during Phase 4. It is interesting that though the fuzzy rules illustrate that the SoC should be sustained around 35%, more electrical power is still available when high power request is demanded at the first 10 minutes of Phase 4. After the power demand falls to the level that the engine can power the aircraft by itself, the generator starts to draw power from the combustion powertrain. The SoC also recovers gradually and reaches about 30% after 10-minute charging.

The target value of battery SoC is 40% at the end of Phase 5, i.e. at the final of the whole flight mission. Convex programming is employed in this landing phase. The extra available power of the engine is used to charge the battery. The power of generator changes from -5 kW to -8 kW, when the aircraft touches down and starts to taxi.

As shown in Figure 7-3, the output current and voltage of the DC/DC converter are compared with ones of the battery, which is equal to the input current and voltage of the DC/DC converter. Before around 7^{th} minute, the battery voltage is higher than the DC/DC converter one. The DC/DC converter works as the buck type and reduces the voltage to the 300 V. The current of the battery is lower than one of DC/DC converter before the 7^{th} minute. After this turning point, the absolute value of battery current cannot be lower than one of DC/DC converter current, since the battery voltage becomes smaller than the DC/DC converter one.

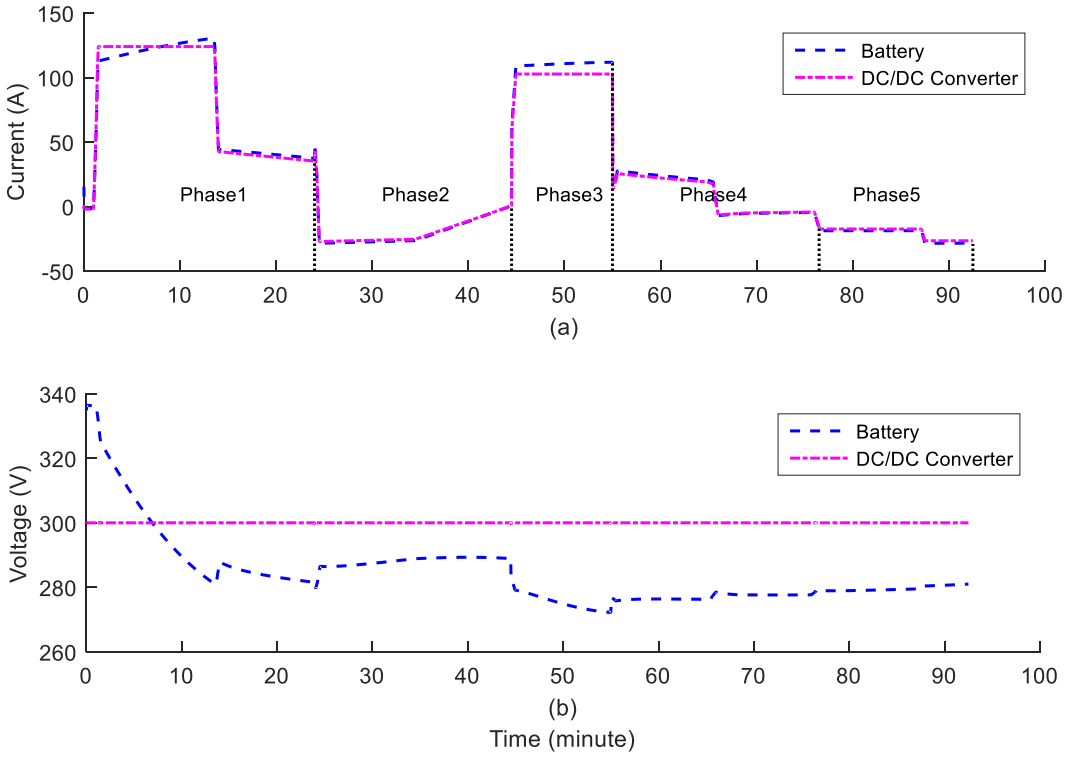

Figure 7-3 Simulation results of test case 3 (2)

The current values of both two devices are above zero for Phase 1 and Phase 3. Phase 1 requests the motor to output power to facilitate the climbing. In Phase 3, the motor provides all the power requested to fly, since the HEPS runs at EM-Only Mode. On the other hand, the current of battery and DC/DC converter becomes all negative values during Phase 2 and Phase 5. The charging process is requested in these two phases to recover the battery SoC. Phase 2 can be considered as the stage of making preparations for Phase 3. The charging process is favoured in the final phase, since extra engine power is usually available. Different from Phase 2, Phase 4 regulates the output current according to the instantaneous power demand and battery SoC. At the first stage of Phase 4, the battery provides electrical power since the power demand is higher than the engine maximum one. For the second stage, the charging power is drawn from the combustion powertrain since the SoC is in its sustaining range.

The test scenario 3 demonstrates another advantage of the FLC based ECMS: it can resolve the conflict between the SoC sustaining and electrical power using. The inherent drawback of all non-rule-based optimizations is that the SoC can only be sustained around a single value. If the SoC is sustained at a very low level, the residual

battery capacity cannot guarantee a safe landing when the engine fails; while the SoC stays at a high level, the combination of the fuel and electric energy cannot be made the best use of. Therefore, the advantages of HEPS for the aircraft would not be exploited to the full, using non-fuzzy-rule-based optimizations. Concluded from the fuzzy logic rules of the FLC based ECMS, the SoC can be sustained to a desirable range (30, 40%) but also permitted to drop to a lower value if necessary and possible.

7.3 Fuel Economy

In this section, the fuel and energy performance of our hybrid propulsion system are analysed and compared with the conventional combustion powertrain. In Chapter 2, the fuel saving performance of HEPS has been already compared with the prototype aircraft, under the same cruising distance. However, the prototype and hybrid aircraft have the different MTOW, cruising speeds and the corresponding power requirements. This brings the question that how much fuel the HEPS can save compared with the engine-only system, powering the same aircraft with the same MTOW.

This section compares the fuel saving performance of HEPS and one of engine-only propulsion system, using the same flight mission. Therefore, the original Continental C-75 engine is replaced by higher-power Continental O-200. Continental O-200 can reach the maximum 75 kW at 2750 rpm. Actually, if only considering the maximum power, Continental C-85 (63 kW) is more appropriate than Continental O-200. However, Continental C-85 can hold at its maximum shaft speed for only 5 minutes, but the time length of climbing in the test scenario 3 is at least 10 minutes. Furthermore, the operating speed range of Continental C-85 is not compatible with our propeller [166]. As a consequence, the slightly over-powered Continental O-200 is selected. On the other hand, the engine of HEPS is still RT600 LCR (see Section 3.7).

Figure 7-4 compares the output power of engine between the hybrid-electric and ICE-only propulsion system. It is clear that the engine of ICE-only propulsion system provides all the power required to fly, while the engine power of HEPS is dependent on energy optimization algorithm. When the power demand is high, it is shown in Figure 7-4 that the output power of HEPS is lower than one of ICE-only propulsion system in Phase 1, since the HEPS combines the power of the electric propulsive unit. When the output of HEPS is higher than one of ICE-only one, the extra power is drawn to charge the battery, e.g. in Phase 2 and 5.

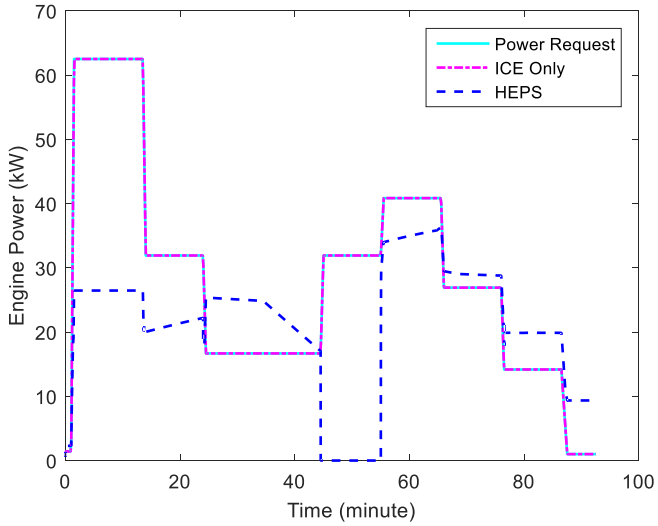

Figure 7-4 Comparison of engine power between HEPS and engine-only powered aircraft

The fuel rate and fuel consumption of two propulsion systems are plotted in Figure 7-5. The fuel rates of two propulsion systems both vary depending on the output power of the engine. In other words, more engine power implies more fuel used. In Phase 3, between 44th and 55th minute, the fuel used rate is not equal to zero when the power demand of RT600 LCR in HEPS is zero. The reason is that the engine is not shut down but held at its idle speed while the power demand is zero. This strategy is to ensure the safety of the HEPS powered aircraft.

Most important factor concluded from Figure 7-5 is that the fuel used rate of HEPS is lower than one of ICE-only propulsion system, during most of the flight time. Even the engine power of HEPS is higher than one of ICE-only powertrain, the fuel rate of HEPS can be lower than one of ICE-only powertrain, for example from around 66th minute to the end of the mission. This indicates that RT600 LCR has better fuel performance than Continental O-200.

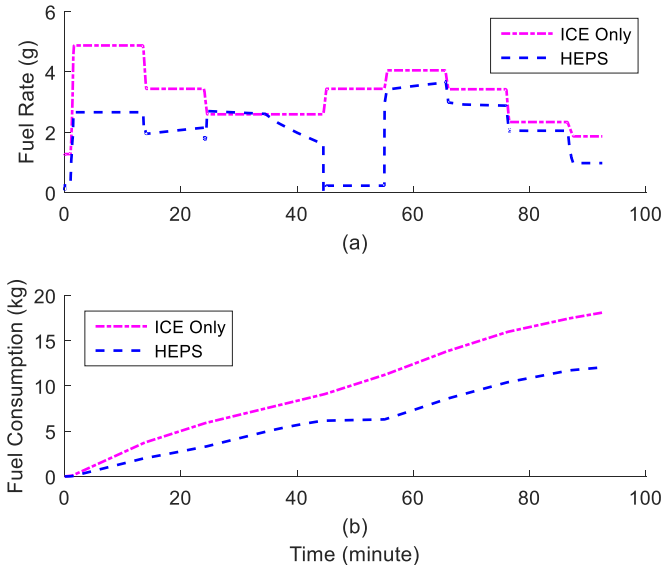

Figure 7-5 Comparison of fuel usage between HEPS and engine-only powered aircraft

The final fuel usages for the complete mission of HEPS and conventional propulsion system are provided by Table 7-2. At the end of the flight mission, the hybrid aircraft can save at most 40.8% fuel compared with the Continental O-200 powered one. Concerning the whole energy consumption, the HEPS also achieves 28.3% reduction. For a nearly 90-minute mission in this test case, the HEPS can save around 6 kg of fuel. In other words, the retrofitted hybrid aircraft can save about 4 kg per 1-hour flight. This means that up to tens of thousands of fuel usage can be reduced in a typical lifetime of one light aircraft.

Table 7-2 Comparison of fuel and energy usage between HEPS and engine-only powered aircraft

	Engine Only	HEPS
Fuel Consumption (kg)	18.1	12.0
Fuel Saving (%)	0	40.8
Energy Consumption (kW*h)	233.4	167.3
Energy Saving (%)	0	28.3

The comparison of fuel consumption between two propulsion systems demonstrates the significant fuel saving capability of HEPS, however, is not quite a fair comparison. One reason for the considerable fuel reduction of our HEPS is that RT600 LCR has higher fuel efficiency than Continental O-200. The fuel consumption of Continental O-200 at the full throttle is between 6.3 g/s and 6.9 g/s, while the fuel rate of RT600 LCR at the maximum power is only 4.8 g/s. This is also demonstrated in Figure 7-5 (a). The fuel rate of Continental O-200 powered aircraft is always higher than one of hybrid aircraft, though the HEPS consumes more engine power for some parts of the flight mission.

The main issue occurs when comparing the fuel performance between HEPS and conventional propulsion system is that RT600 LCR substantially has better fuel efficiency than Continental O-200. Therefore, the SFC of Continental O-200 has to be adjusted by scaling the fuel map of RT600 LCR. In this study, the Willans line model is introduced to re-map the SFC of Continental O-200 using the SFC of RT600 LCR. The Willans line model was originally used to describe a linear relationship between the brake mean effective pressure and the fuel consumption [167]. Researchers have extended it to a scaling technique to approximate the fuel consumption and even efficiency [168].

Figure 7-6 shows the fuel rate and fuel consumption of the hybrid system, ICE-Only system with original fuel map, and ICE-Only system with adjusted fuel map. As illustrated in Figure 7-6 (a), the adjusted fuel rate is remarkably lower than the original one. Moreover, the difference between the original and adjusted fuel rate is small when the engine power is high; while the difference is large if the engine power is low. In other words, the adjusted Continental O-200 (or RT600 LCR) performs even better fuel efficiency at low power area compared with the original Continental O-200. Figure 7-6 (b) compares the fuel usage of ICE-Only system with original fuel map and with adjusted fuel map. Before the end of Phase 1 (around 24th minute), the fuel consumption of ICE-Only system with adjusted fuel map is only slightly lower than one of ICE-Only system with original fuel map. Then, when the power request declines, the difference between the original and the adjusted one becomes larger.

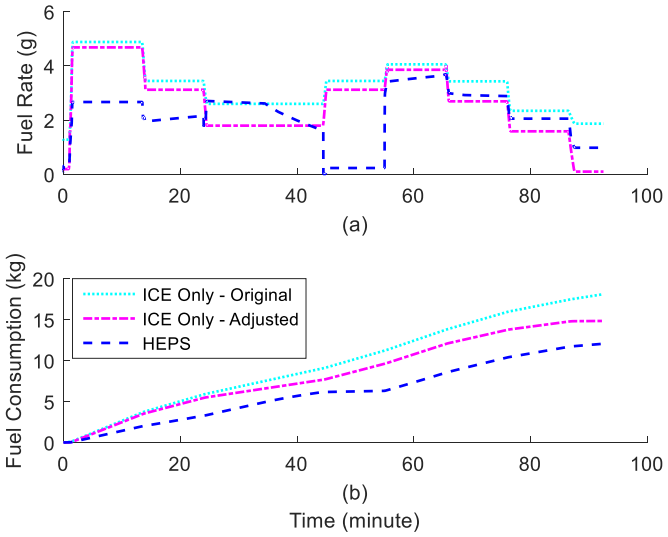

Figure 7-6 Comparison of fuel usage between HEPS and engine-only powered aircraft, with adjusted fuel map

The details of the final fuel consumption and fuel saving of HEPS and ICE-Only system with adjusted fuel map, are listed in Table 7-3. It demonstrates that the hybrid propulsion system still can save 18.7% fuel, even if the fuel map of Continental O-200 in ICE-Only system is re-scaled to the same level of RT600 LCR. The ICE-Only propulsion system consumes 14.8 kg fuel, while HEPS only costs 12 kg. Table 7-3 also gives the energy consumption and saving of the complete propulsion. The energy usage of HEPS is still lower than one of engine-only propulsion system. The hybrid powered aircraft uses 12.5% less energy compared with the conventional engine powered one, to complete the same flight mission.

Table 7-3 Comparison of fuel and energy usage between HEPS and engine-only powered aircraft, with adjusted fuel map

	Engine Only (Adjusted)	HEPS
Fuel Consumption (kg)	14.8	12.0
Fuel Saving (%)	0	18.7
Energy Consumption (kW*h)	191.2	167.3
Energy Saving (%)	0	12.5
Energy Efficiency (%)	20.3	23.2

The energy efficiency in this study is defined as the efficiency of converting the stored energy to the propulsion energy. The energy requirement of one flight mission can be determined using the power requirement. The energy efficiency of engine-only powered aircraft is 20.3%, which cannot be higher than the average efficiency of the engine. The energy efficiency of the hybrid propulsion system (23.2%) is higher than the efficiency of the engine, since the HEPS integrates the electric storage source. The electric energy storage (like the battery) usually has a much higher efficiency of energy conversion than the combustion fuel.

The Federal Office of Civil Aviation (FOCA) of Swiss Confederation carried out a series of experiments to research the aircraft piston engine emissions [169]. The report gives the typical emission factors (emission-weight/fuel-weight) for one specific mission, including the Landing and Take-Off cycle (LTO) and one-hour cruise. The CO_2 emission factor is around 2 kg per 1 kg fuel consumption for one mission, tested on the different piston engines ranging from 100 kW to 220 kW. Since the CO_2 emission factor keeps the same for different piston engines with comparable power outputs, it is applied to the calculation of CO_2 emission for the Continental O-200 powered aircraft. Similarly, the CO emission factor is 760 g per 1 kg fuel consumption for one mission. Yet the authors did not find any open materials covering the rotary engine emission during the flight. Without loss of generality, the same factors are used for estimation of CO_2 and CO emissions for the rotary engine.

Table 7-4 Comparison of fuel usage and CO_2 Emission between HEPS and engine-only powered aircraft

	Engine Only	HEPS
Fuel Consumption (kg)	18.1	12.0
CO_2 Emission (Fuel) (kg)	36.2	24
CO Emission (Fuel) (kg)	13.8	9.12
Electrical Energy Consumption (kW*h)	0	11.9
CO_2 Emission (Electricity) (kg)	0	3.9
Total CO_2 Emission (kg)	36.2	27.9

Another study from the International Energy Agency (IEA) provided the CO_2 emission from the electricity generation [170]. In 2015, Europe produced 329 g CO_2 when generating 1 kWh. Actually, a real-time British electricity fuel mix factor (gCO_2/kWh) is available on the webpage of Electricity Info [171]. The average value in 2017 is 292 g/kWh. To make a relatively fair comparison, the average European value of 2015 is used in this thesis. Note that CO emission from the electricity generation can be neglected.

The general aviation contributes to environment pollutant much less than the civil airlines, in total [172]. The findings in the study of FOCA in 2007 [169] disclosed that piston engine aircraft contribute less than 1% of the total CO_2 emissions from the non-land transportation. However, piston engines applied on aircraft accounts for 40% share of CO emission, since the 'stoichiometric combustion' is hard to achieve for aircraft piston engines.

The total CO_2 and CO emissions of ICE powertrains and HEPS generated in the test case 3 are listed in Table 7-4. The Continental O-200 produces 36.2 kg CO_2 and 13.8 kg CO, while the hybrid propulsion system generates 24 kg CO_2 and 9.12 kg CO when using the on-board fuel. 11.9 kWh electrical energy is consumed in this mission, and 3.9 kg CO_2 is discharged to generate this energy. Put differently, the hybrid aircraft can reduce both CO_2 and CO emissions by approximately 33% by the comparison with engine-only aircraft. The electrical energy is cleaner compared with the fuel combusting in the aircraft engines, even if the CO_2 emissions from the electricity generation process are considered.

7.4 Conclusion

The convex optimization and fuzzy based optimization were combined to complete a flight test case with several sub-tasks. The hypothetical test scenario used in this chapter can be categorized into five phases, with different power and SoC requirements. The test case demonstrates that only the combination of non-causal and causal optimization can satisfy the different constraints and requests of the test scenario. The fuel economy of the HEPS with the two optimizations was also evaluated.

The test scenario also illustrates that the FLC based ECMS is more suitable for hybrid propulsion of aerial vehicles, compared with other ECMS based optimizations. Those ECMS based optimizations were designed for ground vehicles, with no consideration of vehicle safety if the engine fails. The FLC based ECMS can sustain the battery SoC among a range to guarantee the aircraft landing using the remaining electrical energy. The FLC based ECMS also allows the SoC to drop to the lower level if the flight mission requests high power for a short duration. In other words, the FLC based ECMS can not only sustain the SoC in a range around the desirable value, but also take advantage of the electrical energy source to power the aircraft.

Another two advantages of the hybrid propulsion system were revealed in an analysis of the fuel saving performance. Firstly, the hybrid propulsion system can have longer continuous climbing, since the engine does not necessarily work at its maximum power during climbing. The second benefit is that the hybrid propulsion system can enjoy the higher energy efficiency by introducing the electric powertrain.

In this chapter, the hybrid propulsion system was proved to reduce the fuel consumption by 18.7%, when compared with the engine-only propulsion system. This result was concluded with the consideration of the different fuel efficiency levels between different engine classes. The scaling technique was applied to re-map the fuel efficiency using the same engine classes.

8 Summary

This thesis studied the techniques to design and optimize a hybrid electric propulsion system for aircraft. Firstly, the hybrid propulsion system was sized to retrofit the prototype aircraft. Then, dynamic models of the hybrid propulsion system were studied. Two energy optimization supervisory controls were proposed to minimize the fuel consumption of the hybrid propulsion system.

8.1 Conclusion

A parallel hybrid electric propulsion system was designed for the prototype aircraft using the system sizing. The propulsion system sizing was established as a multi-objective optimization problem and optimized by NSGA. The sized hybrid electric propulsion system will ensure that with a fuel saving of 17%, there is no substantial performance loss. Furthermore, the hybrid propulsion system can be sized to achieve larger RoC and higher cruising speed. The novel approach of this work is a new non-dominated sorting algorithm. It was developed to improve the computational efficiency of NSGA. This method can reduce many unnecessary comparisons and achieve $O(MN)$ of the best time complexity of the comparison. One of advantages of NSGA in this study is that the smaller discretization number not only reduces the computation considerably, but also achieves no sacrifice of the precision of the Pareto front results. One interesting conclusion is that the DoH has little impact on the two objectives (fuel usage and flight duration). The sensitivity analysis shows that the Pareto front are more sensitive to the variation of battery energy density than other parameters. The MTOW

of hybrid aircraft was adjusted after the selection of off-the-shelf products, and is 1 kg higher than the MTOW of the original optimized hybrid aircraft.

The dynamic and static characteristics of the main components of the HEPS were modelled. The engine MVM simplified the manifold dynamics and flow rate dynamics, but can represent the dynamics between the throttle command and the output torque. The model has low computational efficiency due to no requirement for the estimation of the torque loss. Regarding the motor/generator, the d-q model and vector control were introduced to simplify its speed and torque control. The torque loss of the d-q model at steady state was estimated using the efficiency map. One of advantages of the battery Shepherd model is the simplicity of identifying the model parameters. This avoids large number of experiments.

The primary energy management problem was first formulated in the convex optimization. The simplified model of powertrain was developed using first principle and experimental data. The experimental data were analysed and approximated to clarify the convexity of the original problem. Subsequently, two techniques, change of variables and equality relaxation were implemented with the need for lossless convexification. The main novelty of this part of work is the proposal of a new lossless convexification by the introduction of variable—battery internal energy. The test cases verify that the convex relaxation does not sacrifice the optimality of the solution nor does the variable change lose the original bounds. Also, the optimal control from convex optimization is demonstrated to be robust against the disturbance. By comparing with the dynamic programming, the convex optimization performs minimal optimal cost results, with much lower optimization time. The most significant advantage is that the convexification reduces the optimization computation to a level compatible with the practical application.

The conventional ECMS was established by introducing the Hamiltonian function. It can convert the original non-causal fuel minimization problem to an equivalent causal one, but cannot sustain the battery SoC. The main contribution of this part of work is to extend the original ECMS by a fuzzy control. The proposed algorithm can keep the battery SoC in a desirable range, without the requisite of off-line estimation of equivalence factor. By comparing with a non-causal optimization—DP, the test case validates that the FLC based ECMS succeeds in converting the non-causal energy optimization, with little sacrifice of the optimality of the solution. In other words, the prior-knowledge of flight mission is not pre-requisite and the FLC based ECMS can

achieve the sub-optimal control for on-line implementation. Another causal optimization (A-ECMS) was also studied and compared. The FLC based ECMS is validated to outperform the A-ECMS, since it can reduce the computation time of optimization and save more fuel.

The convex optimization and fuzzy based optimization were combined to complete a flight mission with several sub-tasks. Each sub-task has different power and SoC requirements. The test case demonstrates that only the combination of non-causal and causal optimization can satisfy the different constraints and requests of the test scenario. The FLC based ECMS considers the safety issue of hybrid powered aircraft, since it can sustain the battery SoC within a range to guarantee that the aircraft is capable of landing using the remaining electrical energy. Compared with the engine-only powered aircraft, the hybrid powered aircraft saves up to 18.7% fuel consumption. Furthermore, the hybrid propulsion system has better efficiency since it integrates the high efficient electric powertrain.

8.2 Future Work Recommendation

The thesis completed the design and energy management of an aircraft HEPS. The new non-causal and casual supervisory controls were proposed to optimize the power distribution between the engine and motor and save fuel consumption. The improved fuel economy performance was validated by the numerical simulation tests. The areas of future work are recommended:

1) The conceptual design of hybrid-powered aircraft. This thesis has been engaged in the sizing of HEPS for a prototype aircraft. The aircraft design was not included due to its high computational complexity. The synergetic sizing of the aircraft and its hybrid propulsion system is an interesting and challenging topic. The aerodynamics of the aircraft and propeller, etc., will be considered and integrated into the developed NSGA. Further study to develop a new non-dominated sorting algorithm is recommended due to the increased computational cost of the new sizing problem.
2) The reduction of pollutant emissions from hybrid propulsion systems. Generally, the total amount of emissions decreases when the fuel consumption reduces. The reduction of CO_2, CO and NO_x is worth studying to reduce the

side effect of hybrid-powered aircraft on the environment. The emission maps of the engine are needed for this further study.

3) The validation of energy optimization strategies in the Hardware-in-the-Loop (HiL) system. The real-time capability is the main performance required to be validated. The optimization solvers for the embedded systems are needed. The on-line estimation of battery SoC will be integrated to the embedded systems. The developed HiL system of the HEPS is briefly described in the Appendix.

9 Appendix

The high-level architecture of HiL system for the HEPS is shown in Figure 9-1. The blocks with dashed outlines are simulated in software, while the others are the hardware implementation of the system. Different categories of lines also denote different physical connections. The black solid line without arrows indicates the mechanical connection between different components, while the power supply is represented by the red solid line with arrows. The control and feedback signal are illustrated via black lines with arrows.

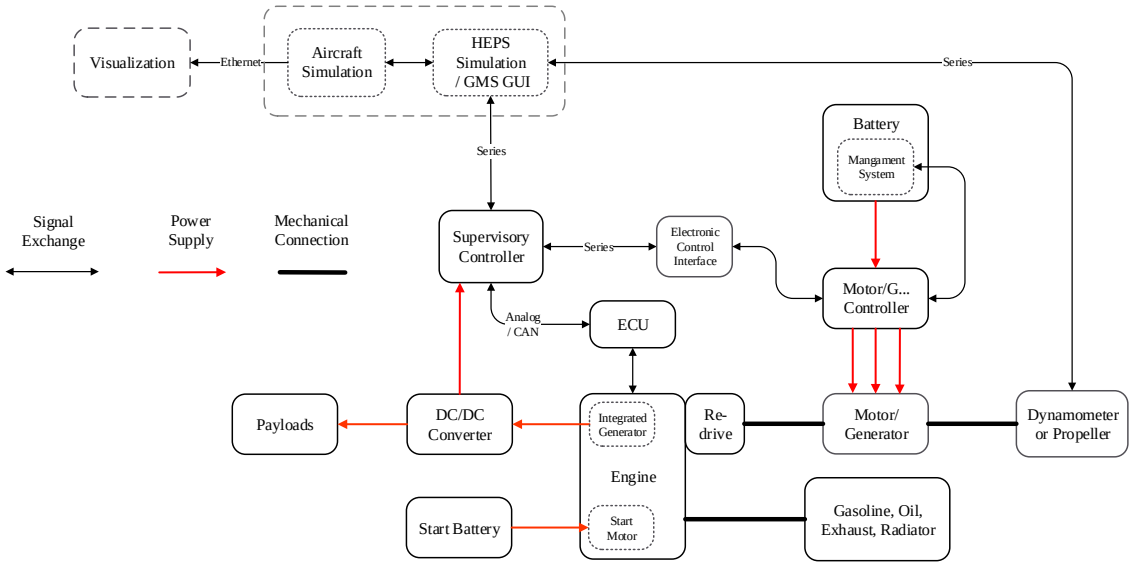

Figure 9-1 Architecture of hardware-in-the-Loop system

The primary function of the supervisory controller is energy optimization of HEPS. The supervisory controller receives power demand from the simulation, optimizes the power

distribution and converts the optimal control to the physical control signal. It sends the analog voltage command to the ECU to regulate the engine throttle; meanwhile, it sets the speed or torque of motor/generator via a series port of the power electronics. The ECU and electronic control interface feed the instant variable values back to the supervisory controller, through the CAN bus and series port, respectively.

As shown in Figure 9-1, the motor/generator acquires the power from the battery via the motor/generator controller. Note that the voltage control of motor/generator is integrated with the motor/generator controller and the battery can manage its discharge/charge process with its own management system. Therefore, there is no need for an extra DC/DC converter between the motor controller and battery. The take-off weight is further saved here. Likewise, the start battery will supply the power to the starter motor of the engine. On the other side, the integrated generator of the engine can power the supervisory controller and some other payloads (like sensors), via a DC/DC converter.

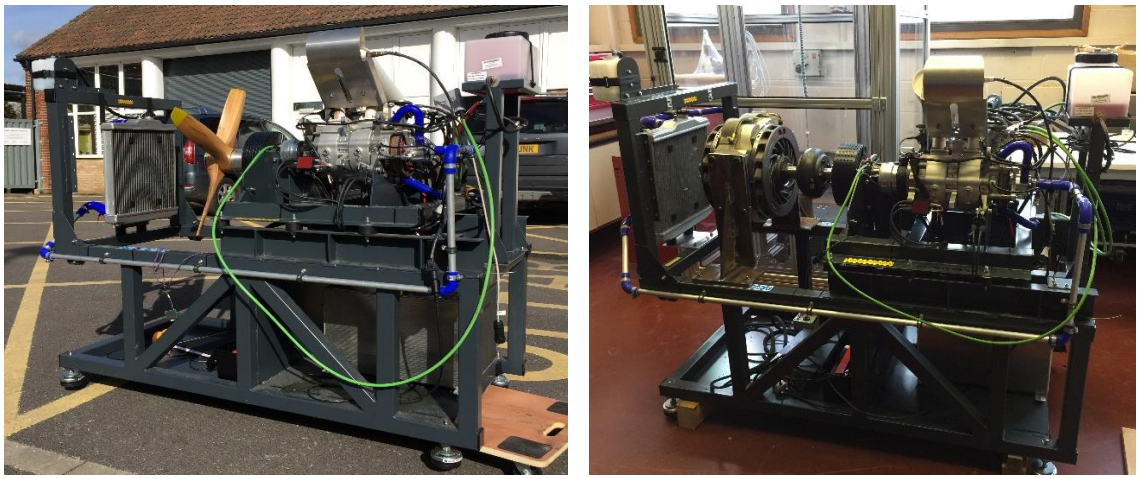

(a) **(b)**

Figure 9-2 Test rig with propeller (a) and dynamometer (b)

A transportable test rig has been manufactured and developed with the assist of Rotron Power Ltd., based on the design of HiL system. The test rig is divided into two layers: the upper layer is to hold and fix the propulsive parts that include the engine (with the exhaust subsystem), motor and propulsion load; the lower layer contains the energy sources (fuel tank and battery), controllers and other auxiliary devices (such as converters and interface boards). The cooling system is developed attached to the

frame of the test rig. Figure 9-2 shows the test rig with the propeller and the air-cooled eddy-current dynamometer. The output shaft of the motor/generator is extended if connected to the dynamometer.

REFERENCES

[1] Z. Zhu, Mode and implementation of a hybrid control system for a 2-mode hybrid electric vehicle, West Virginia University, 2013. http://search.proquest.com/docview/1491165582?accountid=37552.

[2] E.M. Greitzer, P.A. Bonnefoy, E.D. la R. Blanco, C.S. Dorbian, M. Drela, D.K. Hall, R.J. Hansman, J.I. Hileman, R.H. Liebeck, J. Lovegren, P. Mody, J.A. Pertuze, S. Sato, Z.S. Spakovszky, C.S. Tan, J.S. Hollman, J.E. Duda, N. Fitzgerald, J. Houghton, J.L. Kerrebrock, G.F. Kiwada, D. Kordonowy, J.C. Parrish, J. Tylko, E.A. Wen, N+3 Aircraft Concept Designs and Trade Studies, Final Report. Volume 1, 2010. https://ntrs.nasa.gov/search.jsp?R=20100042401.

[3] M. Darecki, C. Edelstenne, T. Enders, E. Fernandez, P. Hartman, J.-P. Herteman, M. Kerkloh, I. King, P. Ky, M. Mathieu, G. Orsi, G. Schotman, C. Smith, J.-D. Wörner, Flightpath 2050 Europe's Vision for Aviation, 2011. http://www.acare4europe.org/sites/acare4europe.org/files/document/Flightpath2050_Final.pdf.

[4] X. Wei, Modeling and Control of a Hybrid Electric Drivetrain for optimum fuel economy, performance and driveability, The Ohio State University, 2004. https://etd.ohiolink.edu/!etd.send_file?accession=osu1095960915&disposition=inline.

[5] C.C. Chan, The State of the Art of Electric, Hybrid, and Fuel Cell Vehicles, Proc. IEEE. 95 (2007) 704–718. doi:10.1109/JPROC.2007.892489.

[6] L. Guzzella, A. Sciarretta, Vehicle Propulsion Systems: Introduction to Modeling

and Optimization, 2013. doi:10.1007/978-3-540-74692-8.

[7] K. Bergsson, Hybrid Vehicle History More than a Century of Evolution and Refinement, (2005). http://www.hybrid-vehicle.org/hybrid-vehicle-history.html (accessed May 23, 2018).

[8] J. Youngs, History of the Hybrid Car, (2012). http://www.jdpower.com/cars/articles/safety-and-mpg/history-hybrid-car (accessed May 23, 2018).

[9] N. Georgano, The Beaulieu encyclopedia of the automobile, Taylor & Francis, 2000.

[10] B. Berman, History of Hybrid Vehicles, (2011). http://www.hybridcars.com/history-of-hybrid-vehicles/ (accessed May 22, 2018).

[11] U.S. Department of Energ, Public Law 94-413, The Electric and Hybrid Vehicle Research, Oak Ridge, TN, 1977. doi:10.2172/12155514.

[12] J. Grahame, 1968: AMC's Amazing Amitron Electric Car, Automobiles. (2008). http://www.retrothing.com/2008/09/1968-amcs-amazi.html (accessed May 23, 2018).

[13] C. Squatriglia, Priustoric: GM Builds a Plug-In Hybrid in ... 1969, (2008). https://www.wired.com/2008/09/priustoric----g/.

[14] Mercedes-Benz Austria GmbH, Mercedes-Benz Omnibusse mit Hybrid-Antrieb, (2018). https://www.mercedes-benz.at/content/austria/mpc/mpc_austria_website/de/home_mpc/bus/home/buses_world/innovations/alternative_drives/hybrid_technology.0001.html (accessed May 24, 2018).

[15] Volkswagen AG, City taxi hybrid prototype, (2018). https://www.volkswagenag.com/en/group/history/chronicle/1973-1981.html (accessed May 24, 2018).

[16] Environmental Policy Analyst, The Partnership for a New Generation of Vehicles: Status and Issues, 2003. https://www.everycrsreport.com/files/20030122_RS20852_45384fa93764404210695783b732baab92cf58f1.pdf.

[17] Toyota City, Worldwide Sales of Toyota Hybrids Surpass 10 Million Units, Toyota Eur. Newsroom. (2017). https://newsroom.toyota.eu/global-sales-of-toyota-hybrids-reach-10-million/ (accessed May 24, 2018).

[18] T. Zaun, Ford to Use Toyota's Hybrid Technology, New York Times. (2004). https://www.nytimes.com/2004/03/10/business/ford-to-use-toyota-s-hybrid-technology.html (accessed May 24, 2018).

[19] Next Green Car, Car of the Year 2010, (2010). http://www.nextgreencar.com/green-car-of-the-year-2010.php#jp (accessed May 24, 2018).

[20] J. Lesage, 2017 Prius Prime Offers Industry's Best 'MPGe' and 25 Miles Electric Range, (2016). http://www.hybridcars.com/2017-prius-prime-offers-industrys-best-mpge-and-25-miles-electric-range/ (accessed May 24, 2018).

[21] F.G. Harmon, A.A. Frank, J. Chattot, Conceptual Design and Simulation of a Small Hybrid-Electric Unmanned Aerial Vehicle, J. Aircr. 43 (2006) 1490–1498. doi:10.2514/1.15816.

[22] R.M. Hiserote, Analysis of hybrid-electric propulsion system designs for small unmanned aircraft systems, Air Force Institute of Technology, 2010.

[23] J.K. Ausserer, Integration, Testing and Validation of a Small Hybrid-Electric Remotely-Piloted Aircraft, Air Force Institute of Technology, 2012.

[24] M.P. Molesworth, Rapid Prototype Development of a Remotely-Piloted Aircraft Powered by a Hybrid-Electric Propulsion System, Air Force Institute of Technology, 2012.

[25] R. Glassock, J.Y. Hung, L.F. Gonzalez, R.A. Walker, Design, modelling and measurement of a hybrid powerplant for unmanned aerial systems, Aust. J. Mech. Eng. 6 (2008) 69–78. doi:10.1080/14484846.2008.11464559.

[26] J.Y. Hung, L.F. Gonzalez, On parallel hybrid-electric propulsion system for unmanned aerial vehicles, Prog. Aerosp. Sci. 51 (2012) 1–17. doi:10.1016/j.paerosci.2011.12.001.

[27] C. Friedrich, P.A. Robertson, Hybrid-Electric Propulsion for Aircraft, J. Aircr. 52 (2015) 176–189. doi:10.2514/1.C032660.

[28] J. Sliwinski, A. Gardi, M. Marino, R. Sabatini, Hybrid-electric propulsion integration in unmanned aircraft, Energy. (2016). doi:10.1016/j.energy.2017.05.183.

[29] Matthew D. Rippl, Sizing Analysis for Aircraft Utilizing Hybrid-Electric Propulsion Systems, Air Force Institute of Technology, 2011.

[30] Jason Paur, Hybrid Power Comes to Aviation, WIRED. (2009). https://www.wired.com/2009/07/hybrid-aviation/ (accessed July 2, 2018).

[31] Embry-Riddle's Eagle Flight Research Center, Propulsion, WIX. (2011). http://embryriddle.wix.com/greenflight3#!__eagle-flight-research-center/the-eco-eagle/vstc1=propulsion (accessed July 2, 2018).

[32] D. Sigler, Launching on a Leaf Blower and a Hacker, CAFE. (2010). http://cafe.foundation/blog/launching-on-a-leaf-blower-and-a-hacker/ (accessed July 2, 2018).

[33] Jason Paur, Siemens Builds the Chevrolet Volt of Airplanes, WIRED. (2011). https://www.wired.com/2011/06/electric-airplane-uses-hybrid-power-similar-to-chevy-volt/ (accessed July 2, 2018).

[34] W. Wittmann, Flying with Siemens Integrated Drive System, SIEMENS. (2013). https://www.siemens.com/press/en/pressrelease/?press=/en/pressrelease/2013/industry/drive-technologies/idt2013064084.htm (accessed July 2, 2018).

[35] Pipistrel, HYPSTAIR Report Summary, 2016. https://cordis.europa.eu/result/rcn/192537_en.html.

[36] R. Glassock, M. Galea, W. Williams, T. Glesk, Hybrid Electric Aircraft Propulsion Case Study for Skydiving Mission, Aerospace. 4 (2017) 45. doi:10.3390/aerospace4030045.

[37] T. Banning, G. Bristow, C. Level, L. Sollmann, J. Calderon-Fernandez, D. Wells, M. Olson, NXG-50, 2013. http://emerald.ts.odu.edu/Apps/FAAUDCA.nsf/Mavris2013.pdf?OpenFileResource.

[38] M. Caujolle, Airbus, Rolls-Royce, and Siemens team up for electric future Partnership launches E-Fan X hybrid-electric flight demonstrator, AIRBUS.

(2017). http://www.airbus.com/newsroom/press-releases/en/2017/11/airbus--rolls-royce--and-siemens-team-up-for-electric-future-par.html (accessed July 2, 2018).

[39] J. Van Bogaert, Assessment of Potential Fuel Saving Benefits of Hybrid- Electric Regional Aircraft, Delft University of Technology, 2015.

[40] N. Madavan, Hybrid-Electric and Distributed Propulsion Technologies for Large Commercial Transports: A NASA Perspective, in: IEEE Energy Convers. Congr. Expo., Montreal, Canada, 2015.

[41] S. Manu, SCEPTOR Distributed Electric Propulsion Aircraft, NASA. (2016). https://sbir.nasa.gov/success-stories/sceptor-distributed-electric-propulsion-aircraft (accessed July 2, 2018).

[42] B. Schiltgen, A.R. Gibson, M. Green, J. Freeman, More Electric Aircraft: “Tube and Wing” Hybrid Electric Distributed Propulsion with Superconducting and Conventional Electric Machines, in: SAE 2013 AeroTech Congr. Exhib., SAE International, 2013. doi:10.4271/2013-01-2306.

[43] Marty K. Bradley, C.K. Droney, Subsonic Ultra Green Aircraft Research: Phase II – Volume II – Hybrid Electric Design Exploration, California, 2015. https://ntrs.nasa.gov/archive/nasa/casi.ntrs.nasa.gov/20150017039.pdf.

[44] R. Gardner, Into the DEAP, SAE Veh. Electrif. (2014).

[45] R. Hiserote, F. Harmon, Analysis of Hybrid-Electric Propulsion System Designs for Small Unmanned Aircraft Systems, in: 8th Annu. Int. Energy Convers. Eng. Conf., 2010. doi:10.2514/6.2010-6687.

[46] A.T. Isikveren, Method of Quadrant-Based Algorithmic Nomographs for Hybrid/Electric Aircraft Predesign, J. Aircr. (2017) 1–10. doi:10.2514/1.C034355.

[47] J. Schoemann, M. Hornung, Modeling of Hybrid Electric Propulsion Systems for Small Unmanned Aerial Vehicles, in: 12th AIAA Aviat. Technol. Integr. Oper. Conf. 14th AIAA/ISSMO Multidiscip. Anal. Optim. Conf., American Institute of Aeronautics and Astronautics, Reston, Virigina, 2012: p. 5610. doi:10.2514/6.2012-5610.

[48] C. Pornet, C. Gologan, P.C. Vratny, A. Seitz, O. Schmitz, A.T. Isikveren, M.

Hornung, Methodology for Sizing and Performance Assessment of Hybrid Energy Aircraft, J. Aircr. 52 (2015) 1–12. doi:10.2514/1.C032716.

[49] D.E. Bryson, C.R. Marks, R.M. Miller, M.P. Rumpfkeil, Multidisciplinary design optimization of quiet, hybrid-electric small unmanned aerial systems, J. Aircr. 53 (2016). doi:10.2514/1.C033455.

[50] J.D. Schaffer, J.J. Grefenstette, Multi-Objective learning via genetic algorithms, J. Chem. Inf. Model. 53 (1989) 160. doi:10.1017/CBO9781107415324.004.

[51] N. Srinivas, K. Deb, Multiobjective optimization using nondominated sorting in genetic algorithms, Evol. Comput. 2 (1994) 221–248. doi:10.1017/CBO9781107415324.004.

[52] K. Deb, A. Pratap, S. Agarwal, T. Meyarivan, A fast and elitist multiobjective genetic algorithm: NSGA-II, IEEE Trans. Evol. Comput. 6 (2002) 182–197. doi:10.1109/4235.996017.

[53] D.E. Goldberg, Genetic Algorithms in Search, Optimization and Machine Learning, Comput. Optim. Appl. (1989) 372. doi:10.1007/s10589-009-9261-6.

[54] M.T. Jensen, Reducing the Run-Time Complexity of Multiobjective EAs: The NSGA-II and Other Algorithms, IEEE Trans. Evol. Comput. 7 (2003) 503–515. doi:10.1109/TEVC.2003.817234.

[55] S. Tang, Z. Cai, J. Zheng, A Fast Method of Constructing the Non-dominated Set: Arena's Principle, in: 2008 Fourth Int. Conf. Nat. Comput., IEEE, 2008: pp. 391–395. doi:10.1109/ICNC.2008.823.

[56] K. McClymont, E. Keedwell, Deductive Sort and Climbing Sort: New Methods for Non-Dominated Sorting, Evol. Comput. 20 (2012) 1–26. doi:10.1162/EVCO_a_00041.

[57] X. Zhang, Y. Tian, R. Cheng, Y. Jin, An Efficient Approach to Nondominated Sorting for Evolutionary Multiobjective Optimization, IEEE Trans. Evol. Comput. 19 (2015) 201–213. doi:10.1109/TEVC.2014.2308305.

[58] X. Zhang, Y. Tian, Y. Jin, Approximate non-dominated sorting for evolutionary many-objective optimization, Inf. Sci. (Ny). 369 (2016) 14–33. doi:10.1016/j.ins.2016.06.007.

[59] L. Guzzella, A. Amstutz, CAE tools for quasi-static modeling and optimization of hybrid powertrains, IEEE Trans. Veh. Technol. 48 (1999) 1762–1769. doi:10.1109/25.806768.

[60] D. Ambuhl, L. Guzzella, Predictive reference signal generator for hybrid electric vehicles, IEEE Trans. Veh. Technol. 58 (2009) 4730–4740. doi:10.1109/TVT.2009.2027709.

[61] N.J. Schouten, M.A. Salman, N.A. Kheir, Fuzzy logic control for parallel hybrid vehicles, IEEE Trans. Control Syst. Technol. 10 (2002) 460–468. doi:10.1109/87.998036.

[62] C. Hou, M. Ouyang, L. Xu, H. Wang, Approximate Pontryagin's minimum principle applied to the energy management of plug-in hybrid electric vehicles, Appl. Energy. 115 (2014) 174–189. doi:10.1016/j.apenergy.2013.11.002.

[63] L. Guzzella, C.H. Onder, Introduction to modeling and control of internal combustion engine systems, 2010. doi:10.1007/978-3-642-10775-7.

[64] J.R. Wagner, D.M. Dawson, L. Zeyu, Nonlinear air-to-fuel ratio and engine speed control for hybrid vehicles, IEEE Trans. Veh. Technol. 52 (2003) 184–195. doi:10.1109/TVT.2002.807156.

[65] F.U. Syed, Modeling and Control Methods for Improving Drivability, Power Management and Fuel Economy in a Hybrid Electric Vehicle, Wayne State University, 2008.

[66] S. Maganti, Control and Model of Power Split Hybrid Electric Car, Texas A&M University, 2011.

[67] P. Pillay, R. Krishnan, Modeling of permanent magnet motor drives, IEEE Trans. Ind. Electron. 35 (1988) 537–541. doi:10.1109/41.9176.

[68] P. Pillay, R. Krishnan, Modeling, simulation, and analysis of permanent-magnet motor drives. I. The permanent-magnet synchronous motor drive, Ind. Appl. IEEE Trans. 25 (1989) 265–273. doi:10.1109/28.25541.

[69] S. a Evangelou, a Shukla, Advances in the modelling and control of series hybrid electric vehicles, Am. Control Conf. (ACC), 2012. (2012) 527–534. http://ieeexplore.ieee.org/stamp/stamp.jsp?tp=&arnumber=6315156.

[70] J. Zhang, Bidirectional DC-DC Power Converter: Design Optimization , Modeling and Control, Virginia Polytechnic Institute and State University, 2008.

[71] M.B. Camara, H. Gualous, F. Gustin, A. Berthon, Design and new control of DC/DC converters to share energy between supercapacitors and batteries in hybrid vehicles, IEEE Trans. Veh. Technol. 57 (2008) 2721–2735. doi:10.1109/TVT.2008.915491.

[72] M.B. Camara, H. Gualous, F. Gustin, A. Berthon, B. Dakyo, DC/DC Converter Design for Supercapacitor and Battery Power Management in Hybrid Vehicle Applications—Polynomial Control Strategy, IEEE Trans. Ind. Electron. 57 (2010) 587–597. doi:10.1109/TIE.2009.2025283.

[73] D. Sha, J. Zhang, X. Wang, W. Yuan, Dynamic Response Improvements of Parallel-Connected Bidirectional DC-DC Converters for Electrical Drive Powered by Low-Voltage Battery Employing Optimized Feedforward Control, IEEE Trans. Power Electron. 32 (2017) 7783–7794. doi:10.1109/TPEL.2016.2637370.

[74] C.M. Shepherd, Design of Primary and Secondary Cells: II. An Equation Describing Battery Discharge, J. Electrochem. Soc. 112 (1965) 657. doi:10.1149/1.2423659.

[75] O. Tremblay, L.-A. Dessaint, A.-I. Dekkiche, A Generic Battery Model for the Dynamic Simulation of Hybrid Electric Vehicles, in: 2007 IEEE Veh. Power Propuls. Conf., IEEE, 2007: pp. 284–289. doi:10.1109/VPPC.2007.4544139.

[76] O. Tremblay, L.A. Dessaint, Experimental validation of a battery dynamic model for EV applications, World Electr. Veh. J. 3 (2009).

[77] M. Gokasan, S. Bogosyan, D.J. Goering, Sliding mode based powertrain control for efficiency improvement in series hybrid-electric vehicles, IEEE Trans. Power Electron. 21 (2006) 779–790. doi:10.1109/TPEL.2006.872373.

[78] X. Zhang, C.C. Mi, C. Yin, Active-charging based powertrain control in series hybrid electric vehicles for efficiency improvement and battery lifetime extension, J. Power Sources. 245 (2014) 292–300. doi:10.1016/j.jpowsour.2013.06.117.

[79] P. Zhang, F. Yan, C. Du, A comprehensive analysis of energy management strategies for hybrid electric vehicles based on bibliometrics, Renew. Sustain.

Energy Rev. 48 (2015) 88–104. doi:10.1016/j.rser.2015.03.093.

[80] O. Sundström, L. Guzzella, P. Soltic, Optimal Hybridization in Two Parallel Hybrid Electric Vehicles using Dynamic Programming, Proc. 17th World Congr. Int. Fed. Autom. Control. (2008) 4642–4647. doi:10.3182/20080706-5-KR-1001.2452.

[81] Y. Yang, X. Hu, H. Pei, Z. Peng, Comparison of power-split and parallel hybrid powertrain architectures with a single electric machine: Dynamic programming approach, Appl. Energy. 168 (2016) 683–690. doi:10.1016/j.apenergy.2016.02.023.

[82] Z. Chen, C.C. Mi, R. Xiong, J. Xu, C. You, Energy management of a power-split plug-in hybrid electric vehicle based on genetic algorithm and quadratic programming, J. Power Sources. 248 (2014) 416–426. doi:10.1016/j.jpowsour.2013.09.085.

[83] P. Elbert, S. Ebbesen, L. Guzzella, Implementation of dynamic programming for n-dimensional optimal control problems with final state constraints, IEEE Trans. Control Syst. Technol. 21 (2013) 924–931. doi:10.1109/TCST.2012.2190935.

[84] M. Oprean, V. Ionescu, N. Mocanu, S. Beloiu, C. Stanciu, Dynamic programming applied to hybrid vehicle control, in: Proc. Int. Conf. Electr. Drives (ICED 88), 1988: p. D2.

[85] A. Brahma, Y. Guezennec, G. Rizzoni, Optimal energy management in series hybrid electric vehicles, in: Proc. 2000 Am. Control Conf., 2000: pp. 60–64 vol.1. doi:10.1109/ACC.2000.878772.

[86] C.-C. Lin, H. Peng, J.W. Grizzle, J.-M. Kang, Power management strategy for a parallel hybrid electric truck, IEEE Trans. Control Syst. Technol. 11 (2003) 839–849. doi:10.1109/TCST.2003.815606.

[87] Y. Bin Yu, Q.N. Wang, Y.J. Chen, C.J. Hu, B.S. Wang, Control strategy optimization research using dynamic programming method for synergic electric system on HEV, in: IEEE Intell. Veh. Symp. Proc., 2009: pp. 770–774. doi:10.1109/IVS.2009.5164375.

[88] D. Bianchi, L. Rolando, L. Serrao, S. Onori, G. Rizzoni, A.-K. Nazar, T.-M. Hsieh,

P. Kang, A Rule-Based Strategy for a Series/Parallel Hybrid Electric Vehicle: An Approach Based on Dynamic Programming, in: ASME Dyn. Syst. Control Conf., 2010: pp. 1–8.

[89] C.-C. Lin, H. Peng, J.W. Grizzle, A stochastic control strategy for hybrid electric vehicles, Proc. 2004 Am. Control Conf. 5 (2004) 4710–4715. doi:10.1109/ACC.2004.182696.

[90] C. Vagg, S. Akehurst, C.J. Brace, L. Ash, Stochastic Dynamic Programming in the Real-World Control of Hybrid Electric Vehicles, IEEE Trans. Control Syst. Technol. 24 (2016) 853–866. doi:10.1109/TCST.2015.2498141.

[91] A. Boyali, L. Guvenc, Real-time controller design for a parallel hybrid electric vehicle using neuro-dynamic programming method, in: 2010 IEEE Int. Conf. Syst. Man Cybern., 2010: pp. 4318–4324. doi:10.1109/ICSMC.2010.5641785.

[92] W. Li, G. Xu, Y. Xu, Online learning control for hybrid electric vehicle, Chinese J. Mech. Eng. 25 (2012) 98–106. doi:10.3901/CJME.2012.01.098.

[93] E.D. Tate, S.P. Boyd, Finding Ultimate Limits of Performance for Hybrid Electric Vehicles, SAE Trans. 109 (1998). doi:10.1.1.16.8058.

[94] G. Steinmauer, L. Del Re, Optimal control of dual power sources, in: Proc. 2001 IEEE Int. Conferece Control Appl., 2001: pp. 422–427. doi:10.1109/CCA.2001.973902.

[95] R. Zhang, Y. Chen, Control of hybrid dynamical systems for electric vehicles, in: Proc. 2001 Am. Control Conf., 2001: pp. 2884–2889. doi:10.1109/ACC.2001.946338.

[96] M. Koot, J.T.B.A. Kessels, B. deJager, W.P.M.H. Heemels, P.P.J. vandenBosch, M. Steinbuch, Energy Management Strategies for Vehicular Electric Power Systems, IEEE Trans. Veh. Technol. 54 (2005) 771–782. doi:10.1109/TVT.2005.847211.

[97] B. Sampathnarayanan, L. Serrao, S. Onori, G. Rizzoni, S. Yurkovich, Model Predictive Control as an Energy Management Strategy for Hybrid Electric Vehicles, in: Proc. ASME Dyn. Syst. Control Conf., 2009: pp. 249–256. http://dx.doi.org/10.1115/DSCC2009-2671.

[98] W. Salman, M.F. Chang, J.-S. Chen, Predictive energy management strategies for hybrid vehicles, in: 2005 IEEE Veh. Power Propuls. Conf., 2005: pp. 21–25.

[99] A.H. Hajimiragha, C.A. Canizares, M.W. Fowler, S. Moazeni, A. Elkamel, A Robust Optimization Approach for Planning the Transition to Plug-in Hybrid Electric Vehicles, IEEE Trans. Power Syst. 26 (2011) 2264–2274. doi:10.1109/TPWRS.2011.2108322.

[100] G. Wu, K. Boriboonsomsin, M.J. Barth, Development and evaluation of an intelligent energy-management strategy for plug-in hybrid electric vehicles, IEEE Trans. Intell. Transp. Syst. 15 (2014) 1091–1100. doi:10.1109/TITS.2013.2294342.

[101] T. Nuesch, P. Elbert, M. Flankl, C. Onder, L. Guzzella, Convex optimization for the energy management of hybrid electric vehicles considering engine start and gearshift costs, Energies. 7 (2014) 834–856. doi:10.3390/en7020834.

[102] N. Murgovski, L.M. Johannesson, J. Sjoberg, Engine on/off control for dimensioning hybrid electric powertrains via convex optimization, IEEE Trans. Veh. Technol. 62 (2013) 2949–2962. doi:10.1109/TVT.2013.2251920.

[103] S. Hadj-Said, G. Colin, A. Ketfi-Cherif, Y. Chamaillard, Convex Optimization for Energy Management of Parallel Hybrid Electric Vehicles, IFAC-PapersOnLine. 49 (2016) 271–276. doi:10.1016/j.ifacol.2016.08.041.

[104] C.M. Martinez, X. Hu, D. Cao, E. Velenis, B. Gao, M. Wellers, Energy Management in Plug-in Hybrid Electric Vehicles: Recent Progress and a Connected Vehicles Perspective, IEEE Trans. Veh. Technol. 66 (2017) 4534–4549. doi:10.1109/TVT.2016.2582721.

[105] N. Murgovski, L. Johannesson, J. Sjoberg, Convex modeling of energy buffers in power control applications, IFAC Proc. Vol. (2012) 92–99. doi:10.3182/20121023-3-FR-4025.00009.

[106] N. Murgovski, L. Johannesson, J. Sjoberg, B. Egardt, Component sizing of a plug-in hybrid electric powertrain via convex optimization, Mechatronics. 22 (2012) 106–120. doi:10.1016/j.mechatronics.2011.12.001.

[107] P. Elbert, T. Nuesch, A. Ritter, N. Murgovski, L. Guzzella, Engine On/Off control

for the energy management of a serial hybrid electric bus via convex optimization, IEEE Trans. Veh. Technol. 63 (2014) 3549–3559. doi:10.1109/TVT.2014.2304137.

[108] N. Murgovski, L.M. Johannesson, B. Egardt, Optimal battery dimensioning and control of a CVT PHEV powertrain, IEEE Trans. Veh. Technol. 63 (2014) 2151–2161. doi:10.1109/TVT.2013.2290601.

[109] N. Murgovski, L. Johannesson, X. Hu, B. Egardt, J. Sjoberg, Convex relaxations in the optimal control of electrified vehicles, Proc. Am. Control Conf. 2015–July (2015) 2292–2298. doi:10.1109/ACC.2015.7171074.

[110] X. Hu, L. Johannesson, N. Murgovski, B. Egardt, Longevity-conscious dimensioning and power management of the hybrid energy storage system in a fuel cell hybrid electric bus, Appl. Energy. 137 (2015) 913–924. doi:10.1016/j.apenergy.2014.05.013.

[111] X. Hu, S.J. Moura, N. Murgovski, B. Egardt, D. Cao, Integrated Optimization of Battery Sizing, Charging, and Power Management in Plug-In Hybrid Electric Vehicles, IEEE Trans. Control Syst. Technol. 24 (2016) 1036–1043. doi:10.1109/TCST.2015.2476799.

[112] J.-Y. Park, Y.-K. Park, J.-H. Park, Optimal power distribution strategy for series—parallel hybrid electric vehicles, Proc. Inst. Mech. Eng. Part D J. Automob. Eng. 222 (2008) 989–1000. doi:10.1243/09544070JAUTO518.

[113] K. Ahn, P.Y. Papalambros, Engine optimal operation lines for power-split hybrid electric vehicles, Proc. Inst. Mech. Eng. Part D J. Automob. Eng. 223 (2009) 1149–1162. doi:10.1243/09544070JAUTO1124.

[114] D. Sun, X. Lin, D. Qin, T. Deng, Power-balancing instantaneous optimization energy management for a novel series-parallel hybrid electric bus, Chinese J. Mech. Eng. 25 (2012) 1161–1170. doi:10.3901/CJME.2012.06.1161.

[115] K. Ahn, S. Cho, S. Won Cha, J. Moo Lee, Engine operation for the planetary gear hybrid powertrain, Proc. Inst. Mech. Eng. Part D J. Automob. Eng. 220 (2006) 1727–1735. doi:10.1243/09544070JAUTO279.

[116] Ho Jae Lee, Jin Bae Park, Guanrong Chen, Robust fuzzy control of nonlinear

systems with parametric uncertainties, IEEE Trans. Fuzzy Syst. 9 (2001) 369–379. doi:10.1109/91.919258.

[117] Hyeoun-Dong Lee, Seung-Ki Sul, Fuzzy-logic-based torque control strategy for parallel-type hybrid electric vehicle, IEEE Trans. Ind. Electron. 45 (1998) 625–632. doi:10.1109/41.704891.

[118] B.M. Baumann, G. Washington, B.C. Glenn, G. Rizzoni, Mechatronic design and control of hybrid electric vehicles, IEEE/ASME Trans. Mechatronics. 5 (2000) 58–72. doi:10.1109/3516.828590.

[119] M. Montazeri-Gh, A. Ahmadi, M. Asadi, Driving condition recognition for genetic-fuzzy HEV control, in: 2008 3rd Int. Work. Genet. Evol. Fuzzy Syst. GEFS, 2008: pp. 65–70. doi:10.1109/GEFS.2008.4484569.

[120] J. Liang, J. Zhang, H. Zhang, C. Yin, Fuzzy energy management optimization for a parallel hybrid electric vehicle using chaotic non-dominated sorting genetic algorithm , Automatika. 56 (2015) 149–163. doi:10.7305/automatika.2015.07.714.

[121] M. Dawei, Z. Yu, Z. Meilan, N. Risha, Intelligent fuzzy energy management research for a uniaxial parallel hybrid electric vehicle, Comput. Electr. Eng. 58 (2017) 447–464. doi:10.1016/j.compeleceng.2016.03.014.

[122] L. Serrao, S. Onori, A. Sciarretta, Y. Guezennec, G. Rizzoni, Optimal energy management of hybrid electric vehicles including battery aging, in: Proc. 2011 Am. Control Conf., IEEE, 2011: pp. 2125–2130. doi:10.1109/ACC.2011.5991576.

[123] M. Ghasemi, X. Song, A Computationally Efficient Optimal Power Management for Power Split Hybrid Vehicle Based on Pontryagin's Minimum Principle, in: ASME 2017 Dyn. Syst. Control Conf., ASME, 2017: p. V002T17A008. doi:10.1115/DSCC2017-5244.

[124] N. Kim, S. Cha, H. Peng, Optimal Control of Hybrid Electric Vehicles Based on Pontryagin's Minimum Principle, IEEE Trans. Control Syst. Technol. 19 (2010) 1279–1287. doi:10.1109/TCST.2010.2061232.

[125] N. Kim, A. Rousseau, D. Lee, A jump condition of PMP-based control for

PHEVs, J. Power Sources. 196 (2011) 10380–10386. doi:10.1016/j.jpowsour.2011.07.003.

[126] S. Delprat, J. Lauber, T.-M. Guerra, J. Rimaux, Control of a Parallel Hybrid Powertrain: Optimal Control, IEEE Trans. Veh. Technol. 53 (2004) 872–881. doi:10.1109/TVT.2004.827161.

[127] D. Sinoquet, G. Rousseau, Y. Milhau, Design optimization and optimal control for hybrid vehicles, Optim. Eng. 12 (2011) 199–213. doi:10.1007/s11081-009-9100-8.

[128] C. Zhang, A. Vahidi, Route preview in energy management of plug-in hybrid vehicles, IEEE Trans. Control Syst. Technol. 20 (2012) 546–553. doi:10.1109/TCST.2011.2115242.

[129] D. Ambuhl, O. Sundstrom, A. Sciarretta, L. Guzzella, Explicit optimal control policy and its practical application for hybrid electric powertrains, Control Eng. Pract. 18 (2010) 1429–1439. doi:10.1016/j.conengprac.2010.08.003.

[130] G. Paganelli, T.M. Guerra, S. Delprat, J.-J. Santin, M. Delhom, E. Combes, Simulation and assessment of power control strategies for a parallel hybrid car, Proc. Inst. Mech. Eng. Part D J. Automob. Eng. 214 (2000) 705–717. doi:10.1243/0954407001527583.

[131] L. Serrao, S. Onori, G. Rizzoni, ECMS as a realization of pontryagin's minimum principle for HEV control, in: Proc. Am. Control Conf., 2009: pp. 3964–3969. doi:10.1109/ACC.2009.5160628.

[132] D. Sinoquet, G. Rousseau, Y. Milhau, Design optimization and optimal control for hybrid vehicles, Optim. Eng. 12 (2011) 199–213. doi:10.1007/s11081-009-9100-8.

[133] J. Park, J.H. Park, Development of equivalent fuel consumption minimization strategy for hybrid electric vehicles, Int. J. Automot. Technol. 13 (2012) 835–843. doi:10.1007/s12239-012-0084-6.

[134] K. Ahn, S. Cho, S.W. Cha, Optimal operation of the power-split hybrid electric vehicle powertrain, Proc. Inst. Mech. Eng. Part D J. Automob. Eng. 222 (2008) 789–800. doi:10.1243/09544070JAUTO426.

[135] B. Skugor, J. Deur, M. Cipek, D. Pavkovi, Design of a power-split hybrid electric vehicle control system utilizing a rule-based controller and an equivalent consumption minimization strategy, Proc. Inst. Mech. Eng. Part D J. Automob. Eng. 228 (2014) 631–648. doi:10.1177/0954407013517220.

[136] Jinming Liu, Huei Peng, Modeling and Control of a Power-Split Hybrid Vehicle, IEEE Trans. Control Syst. Technol. 16 (2008) 1242–1251. doi:10.1109/TCST.2008.919447.

[137] D. Pei, M.J. Leamy, Dynamic Programming-Informed Equivalent Cost Minimization Control Strategies for Hybrid-Electric Vehicles, J. Dyn. Syst. Meas. Control. 135 (2013) 051013. doi:10.1115/1.4024788.

[138] G. Paganelli, General supervisory control policy for the energy optimization of charge-sustaining hybrid electric vehicles, JSAE Rev. 22 (2001) 511–518. doi:10.1016/S0389-4304(01)00138-2.

[139] S. Onori, L. Serrao, G. Rizzoni, Adaptive Equivalent Consumption Minimization Strategy for Hybrid Electric Vehicles, in: ASME 2010 Dyn. Syst. Control Conf. Vol. 1, ASME, 2010: pp. 499–505. doi:10.1115/DSCC2010-4211.

[140] V. Sezer, M. Gokasan, S. Bogosyan, A Novel ECMS and Combined Cost Map Approach for High-Efficiency Series Hybrid Electric Vehicles, IEEE Trans. Veh. Technol. 60 (2011) 3557–3570. doi:10.1109/TVT.2011.2166981.

[141] C. Sun, F. Sun, H. He, Investigating adaptive-ECMS with velocity forecast ability for hybrid electric vehicles, Appl. Energy. 185 (2017) 1644–1653. doi:10.1016/j.apenergy.2016.02.026.

[142] A. Rezaei, J.B. Burl, B. Zhou, Estimation of the ECMS Equivalent Factor Bounds for Hybrid Electric Vehicles, IEEE Trans. Control Syst. Technol. (2017). doi:10.1109/TCST.2017.2740836.

[143] Y. Xie, A. Savvaris, A. Tsourdos, J. Laycock, A. Farmer, Modelling and control of a hybrid electric propulsion system for unmanned aerial vehicles, in: 2018 IEEE Aerosp. Conf., IEEE, Bozeman, 2018: pp. 1–13. doi:10.1109/AERO.2018.8396436.

[144] T. Hofman, Rule-based equivalent fuel consumption minimization strategies for

hybrid vehicles, in: IFAC Proc. Vol., 2008. doi:10.3182/20080706-5-KR-1001.0573.

[145] D.P. Raymer, Aircraft Design: A Conceptual Approach, 1989.

[146] J.D. Anderson, Aircraft Performance and Design, 1999.

[147] B.H. Carson, Fuel Efficiency of Small Aircraft, J. Aircr. 19 (1982) 473–479. doi:10.2514/3.57417.

[148] MagniX, Permanent Magnet Electric Motors, (n.d.). https://www.magniflux.com/#Magniflux-Technology (accessed November 20, 2017).

[149] Z. Chen, B. Xia, C. You, C.C. Mi, A novel energy management method for series plug-in hybrid electric vehicles, Appl. Energy. (2015). doi:10.1016/j.apenergy.2015.02.004.

[150] F.G. Harmon, Neural network control of a parallel hybrid-electric propulsion system for a small unmanned aerial vehicle, 2005.

[151] C. Pornet, A.T. Isikveren, Conceptual design of hybrid-electric transport aircraft, Prog. Aerosp. Sci. 79 (2015) 114–135. doi:10.1016/j.paerosci.2015.09.002.

[152] A. Seshadri, NSGA - II: A multi-objective optimization algorithm, (n.d.). https://uk.mathworks.com/matlabcentral/fileexchange/10429-nsga-ii--a-multi-objective-optimization-algorithm (accessed November 22, 2017).

[153] C. Bao, L. Xu, E.D. Goodman, L. Cao, A novel non-dominated sorting algorithm for evolutionary multi-objective optimization, J. Comput. Sci. 23 (2017) 31–43. doi:10.1016/j.jocs.2017.09.015.

[154] Kokam, KOKAM Li-ion/Polymer Cell, (n.d.). http://kokam.com/data/Kokam_Cell_Brochure_V.4.pdf (accessed November 24, 2017).

[155] Rotron Power Ltd, ROTRON RT600LCR, (n.d.). http://www.rotronuav.com/engines/rt-600 (accessed January 19, 2018).

[156] EMRAX d.o.o., Company EMRAX d.o.o., (n.d.). http://emrax.com (accessed January 19, 2018).

[157] S.P. Rosado, Voltage Stability and Control in Autonomous Electric Power Systems with Variable Frequency, Virginia Polytechnic Institute and State University, 2007.

[158] Z. Xu, D. Zhang, F. Wang, D. Boroyevich, A unified control for the combined permanent magnet generator and active rectifier system, IEEE Trans. Power Electron. 29 (2014) 5644–5656. doi:10.1109/TPEL.2014.2300191.

[159] R. Bellman, Dynamic Programming, 1957. doi:10.1108/eb059970.

[160] S. Onori, L. Serrao, G. Rizzoni, Hybrid electric vehicles: Energy management strategies, Springer, 2016.

[161] S. Boyd, L. Vandenberghe, Convex Optimization, 2010. doi:10.1080/10556781003625177.

[162] R.L. Burden, J.D. Faires, Numerical Analysis, 2011. doi:10.1017/CBO9781107415324.004.

[163] L.D. Berkovitz, Optimal Control Theory, Springer Science+Business Media, LLC, 1974.

[164] A. Sciarretta, M. Back, L. Guzzella, Optimal Control of Parallel Hybrid Electric Vehicles, IEEE Trans. Control Syst. Technol. 12 (2004) 352–363. doi:10.1109/TCST.2004.824312.

[165] K.M. Passino, S. Yurkovich, Fuzzy Control, Addison-Wesley, 1998. doi:10.3233/978-1-60750-706-2-39.

[166] Continental, Continental Overhual Manual for Aircraft Engine Models: C75, C85, C90 & O-200, n.d.

[167] A. Rajagopalan, G. Washington, G. Rizzoni, Y. Guezennec, Development of Fuzzy Logic and Neural Network Control and Advanced Emissions Modeling for Parallel Hybrid Vehicles, Golden, CO (United States), 2003. doi:10.2172/15006009.

[168] Joachim Schömann, Hybrid-Electric Propulsion Systems for Small Unmanned Aircraft, Technische Universität München, 2014.

[169] Federal Office of Civil Aviation, Aircraft Piston Engine Emissions: Summary

Report, 2007.

[170] I.E.A. IEA, CO2 Emissions from Fuel Combustion 2017 - Highlights, Int. Energy Agency. (2017). doi:10.1787/co2_fuel-2017-en.

[171] Electricity Info, Real Time British Electricity Fuel Mix, (n.d.). http://electricityinfo.org/real-time-british-electricity-supply/ (accessed July 20, 2018).

[172] T.I. Yacovitch, Z. Yu, S.C. Herndon, R. Miake-Lye, D. Liscinsky, W.B. Knighton, M. Kenney, C. Schoonard, P. Pringle, Exhaust Emissions from In-Use General Aviation Aircraft, in: Aircr. Noise Emiss. Reduct. Symp., Arlington, 2017.